12

IONOSPHERIC REFLECTION AND ABSORPTION PROPERTIES OF NORMAL MODES AT ELF

Interim Report No. 772

R.A. Pappert and L.R. Shockey

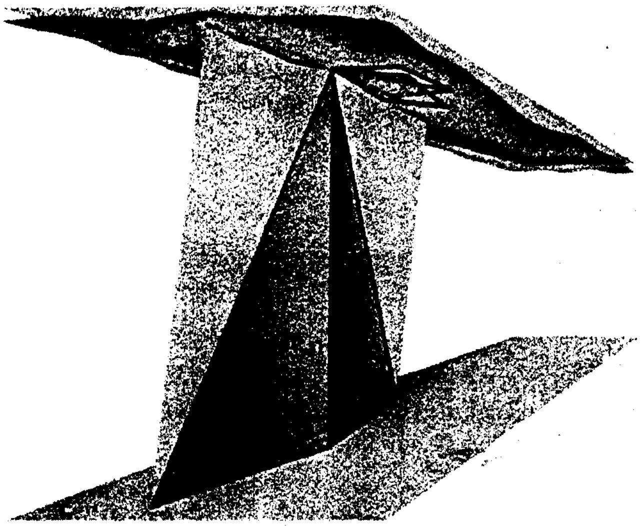

EM PROPAGATION DIVISION
NAVAL OCEAN SYSTEMS CENTER
SAN DIEGO, CALIFORNIA 92152

15 SEPTEMBER 1977

"This work sponsored by the
Defense Nuclear Agency under:
Subtask Code S99QAXHB051 and Work Unit 08"

UNCLASSIFIED
SECURITY CLASSIFICATION OF THIS PAGE (When Data Entered)

REPORT DOCUMENTATION PAGE

READ INSTRUCTIONS BEFORE COMPLETING FORM

1. REPORT NUMBER ⑭ NOSC/IR-
Interim Report No. 772

2. GOVT ~~ACCESSION NO.~~

~~3. RECIPIENT'S CATALOG NUMBER~~

⑨ Interim rept. Jan-Sep 77

~~4. TITLE (and Subtitle)~~
⑥ Ionospheric Reflection and Absorption Properties of Normal Modes at ELF.

~~5. TYPE OF REPORT & PERIOD COVERED~~
Research Report 1/77-9/77

6. PERFORMING ORG. REPORT NUMBER
Interim Report to DNA #772

7. AUTHOR(s)
⑩ R. A. Pappert ~~and~~ L. R. Shockey

8. CONTRACT OR GRANT NUMBER(s)
⑮ DNA MIPR ~~#~~77-522

9. ~~PERFORMING~~ ORGANIZATION NAME AND ADDRESS
Naval Ocean Systems Center
San Diego, CA 92152

10. PROGRAM ELEMENT, PROJECT, TASK AREA & WORK UNIT NUMBERS
⑯ DNA S99QAX HB051
NOSC M402

11. CONTROLLING OFFICE NAME AND ADDRESS
Defense Nuclear Agency
RAAE
Washington, D. C. 20305

~~12. REPORT DATE~~
⑪ 15 Sep 1977

⑰ B051

~~13. NUMBER OF PAGES~~
96

14. MONITORING AGENCY NAME & ADDRESS (if different from Controlling Office)
⑫ 104p.

15. SECURITY CLASS. (of this report)
UNCLASSIFIED

15a. DECLASSIFICATION/DOWNGRADING SCHEDULE

16. DISTRIBUTION STATEMENT (of this Report)

Approved for public release; distribution unlimited

17. DISTRIBUTION STATEMENT (of the abstract entered in Block 20, if different from Report)

D D C
FEB 3 1978
F

18. SUPPLEMENTARY NOTES

19. KEY WORDS (Continue on reverse side if necessary and identify by block number)
Extremely low Frequency
Waveguide propagation
Sporadic E Layers
Ionospheric models

20. ABSTRACT (Continue on reverse side if necessary and identify by block number)

As an aid to better understanding ELF propagation in the earth-ionosphere waveguide, full-wave ELF modal height gains are analyzed as regards regions of reflection and absorption. Frequencies in the Schumann and Seafarer bands are discussed for representative day/night, ambient and disturbed ionospheres. Enhancement of the earth-ionosphere waveguide attenuation due to Sporadic E layering is discussed and the origin of the enhancement clarified.

DD FORM 1 JAN 73 1473 EDITION OF 1 NOV 65 IS OBSOLETE
S/N 0102-LF-014-6601

UNCLASSIFIED
SECURITY CLASSIFICATION OF THIS PAGE (When Data Entered)

393 159

CONTENTS

ILLUSTRATIONS

ILLUSTRATIONS (Continued)

ILLUSTRATIONS (Continued)

ILLUSTRATIONS (Continued) PAGE

ILLUSTRATIONS (Continued)

TABLE

ABSTRACT

As an aid to better understanding ELF propagation in the earth-ionosphere waveguide, full wave ELF modal height gains are analyzed as regards regions of reflection and absorption. Frequencies in the Schumann and Seafarer bands are discussed for representative day/night, ambient and disturbed ionospheres. Enhancement of the earth ionosphere waveguide attenuation due to sporadic E layering is discussed and the origin of the enhancement clarified.

1. INTRODUCTION

In the field of extremely low frequency and very low frequency (ELF), (VLF) propagation in the earth-ionosphere waveguide, much attention has been given in recent years to the problem of solving the modal equation for ionospheres having a gradual continuous increase in electron and ion densities with height at the lower boundary while simultaneously making allowance for anisotropy resulting from the geomagnetic field. Most of these solutions are obtained numerically and various approaches are documented in the works of Budden[1,2], Wait[3], Galejs[4] and Krasnushkin[5]. A by-product of numerical solutions is much quantitative information concerning critical ionospheric height regions as regards reflection and absorption processes. Particularly as regards ambient ionospheres, where the geomagnetic field plays a role, this information has been to a great extent ignored because of the intense interest in the normal mode properties themselves (i.e. phase velocities and attenuations) as well as their excitations. This is unfortunate since detailed full wave analysis of normal mode reflection and absorption can provide valuable insights into puzzling features of the modal properties. As an example, from full wave outputs for ELF normal mode attenuation rates it has been observed that the presence of a sporadic E layer at nighttime could increase attenuation from an order of magnitude of 1 dB/Mm to about 10 dB/Mm in the Seafarer band[6,7]. But without detailed full wave analysis of normal mode reflection and absorption, the underlying mechanisms must remain somewhat obscure. Moreover, the attenuation enhancement cited above may play a significant role in the relatively short path (1600 km) 6-8 dB fades reported in connection with emissions from the Wisconsin Test

Facility[8,9]. Finally, a detailed full wave analysis of normal mode reflection and absorption can provide constructive guidance in the problem area of profile fitting to radio frequency data in the ELF band. Thus, to illustrate some of the information available from full wave programs as well as to provide a better understanding of ELF propagation in the earth-ionosphere waveguide, full wave ELF modal height gains are analyzed in this report for a variety of ionospheres as regards regions of reflection and absorption. Results will be presented for frequencies between the Schumann band and about 100 Hz for representative day/night ambient and disturbed ionospheres.

In the following section notation for some of the more important symbols is given. In section 3 relevant formulas utilizing the full wave fields will be summarized, in section 4 results are presented and in section 5 conclusions are summarized. Appendices A and B contain derivations of formulas useful for understanding features of the full wave absorption results and Appendix C contains the derivation for a simplified sporadic E layer model which gives insight into the origin of attenuation rate resonances associated with such layering.

The full wave fields program utilized in this study, apart from modifications effected to extract field information in the most comprehensible form for our purposes, was developed by Mr. C. H. Shellman and is a Runge-Kutta variant of the original fields program developed by Mr. R. Smith[10]. The latter was based on the Inoue-Horowitz[11] and Pitteway[12] papers. The earth-ionosphere waveguide eigenangles which serve as input to the full wave fields program and modal attenuation rates presented in section 4 are based on Budden's formalism[1,2] as discussed by Pappert and Moler[13].

2. NOTATION

Unless otherwise specified MKS units are assumed throughout the study reported here and some of the more important symbols are the following:

x, y, z	Cartesian coordinates; z is measured vertically upwards into the ionosphere and x is measured horizontally with x-z the plane of incidence.
$\vec{E}$	Radio wave electric field intensity.
$\vec{H}$	Radio wave magnetic field intensity.
$\vec{\mathcal{H}} = Z_0\vec{H}$	Normalized radio wave magnetic field intensity.
$\vec{P}$	Polarization vector.
$\vec{\pi}$	Poynting flux vector.
Z_0	Characteristic impedance of free space.
E_i	$i = 1, 2, 3$; x, y, z components respectively of $\vec{E}$.
H_i	$i = 1, 2, 3$; x, y, z components respectively of $\vec{H}$.
$\mathcal{H}_i$	$i = 1, 2, 3$; x, y, z components respectively of $\vec{\mathcal{H}}$.
P_i	$i = 1, 2, 3$; x, y, z components respectively of $\vec{P}$.
π_i	$i = 1, 2, 3$; x, y, z components respectively of $\vec{\pi}$.
$*$	Complex conjugate.
Im	Imaginary part of.
Re	Real part of.
ϵ_0	Free space permittivity.
ω	$2\pi \times$ frequency of rf wave.
M_{ij}	$i = 1, 2, 3$; $j = 1, 2, 3$; xx, xy, xz, etc., components of susceptibility tensor.
$\mathcal{J}$	Relative heating loss per unit volume.
t	Time.

$k =$	$2\pi/\lambda_0$ free space wavenumber of radio wave.
λ_0	Free space wavelength of radio wave.
θ	Plane wave angle of incidence measured from z (can be eigenangle)
S	$\sin(\theta)$
C	$\cos(\theta)$
ν_j	Collision frequency for species j.
ω_{cj}	2πx cylotron frequency for species j (taken to be positive for all species).
ω_{pj}	2πx plasma frequency for species j.
n	Direction cosine between geomagnetic field and z axis.
c	Speed of light in vacuum.
ω_j	$\|n\|\omega_{cj}$

3. SUMMARY OF EQUATIONS

Principal outputs of full wave ELF and VLF programs such as documented by Smith[10] are the electric ($\vec{E}$) and magnetic ($\vec{H}$) fields both within and without the ionosphere. These fields could be identified, as is often the case, with vertically or horizontally plane polarized waves incident on the ionosphere or they can be identified with generally complex eigenangles satisfying the fundamental determinantal mode equation:

$$F(\theta) = |I - R_D(\theta)\bar{R}_D(\theta)| = 0 \tag{1}$$

with I the unit matrix, R_D the two by two plane wave reflection matrix associated with reflection from everything above the level D and $\bar{R}_D$ the plane wave reflection matrix associated with reflection from everything below the level D. Results presented in the next section are in fact for fields associated with the zeros of equation 1 and as such represent normal mode reflection and absorption properties. Normalization of the modal height gain functions is such that the magnetic field component $\mathcal{H}_2$ at the ground is 1 volt/m. In the remainder of this section are summarized those formulas which involve the full wave fields and which we believe are most useful as a diagnostic tool for understanding fundamental ELF absorption and reflection processes.

a. Absorption and attenuation.

The time average rate of conversion of rf energy into heat per unit volume is given by:

$$J = -\frac{\omega}{2}\,\mathrm{Im}(\vec{E}^{*}\cdot\vec{P})\ \frac{\mathrm{Watts}}{\mathrm{m}^3} \tag{2}$$

where the components of the polarization vector, $\vec{P}$, are given by

$$P_i = \epsilon_o \sum_{j=1}^{3} M_{ij} E_j \qquad i = 1, 2, 3 \tag{3}$$

The time average of the Poynting vector is given by:

$$\vec{\pi} = \frac{1}{2}\,\mathrm{Re}\,(\vec{E} \times \vec{H}^{*}) \quad \frac{\text{Watts}}{\text{m}^2} \qquad (4)$$

and is generally interpreted as the time averaged energy flux.

A convenient measure of the integrated effect of the Joule heating up to altitude z is in terms of attenuation units given by

$$\beta_A(z) = 4343.\frac{\int_0^z J\,dz}{\int_0^h \pi_1\,dz} \quad \text{dB/1000 km} \qquad (5)$$

where h is selected high enough to encapture essentially all of the energy flux in the x direction. Although lower altitudes suffice, results of Eq (5) given in the following section are generally based on an h at F region altitudes during the night and on an h of ≃ 150 km during the day.

Results showing β_A as a function of z will be given in the following section. Such a display will show the buildup of the absorptive contribution to the total attenuation with altitude.

It is also of some interest to have information concerning both upgoing and downgoing waves. To understand how it is achieved a brief review of the mechanics of the full wave fields program will first be given.

In a horizontally stratified medium, an electromagnetic wave with time and x dependence of the form $\exp(i(\omega t - kSx))$ and invariant in the y direction, has an altitude (z) dependence determined by the coupled first order differential equations:

$$\frac{de}{dz} = -ikTe \tag{6}$$

where e is a column vector of field components given by:

$$e = \begin{pmatrix} E_1 \\ -E_2 \\ \mathcal{H}_1 \\ \mathcal{H}_2 \end{pmatrix} \tag{7}$$

T is a 4 X 4 matrix which depends upon the incidence angle, θ, and upon the susceptibility matrix elements (see Clemmow and Heading[14] or Budden[15] - Eq 18.7). The latter of course depends upon z through the electron and ion densities and collision frequencies. They also depend upon both the magnitude and orientation of the geomagnetic field.

Various computational techniques are available for solving Eqs. (6). Smith's[10] program is based upon the Inoue-Horowitz[11] method whereas Shellman's variant which has been used in the present study is based on a a Runge-Kutta integration, but otherwise incorporates the same scaling and other features as Smith's program. The integration is begun high in the ionosphere, where downcoming waves are assumed small. The two upgoing solutions are integrated to the ground, combined to achieve the correct polarization at the ground (except for unusual circumstances discussed in section 4 and Appendix C the polarization at the ground in the lower ELF band may be regarded as vertical) and re-combined at all heights to yield correct field strengths. Once e (Eq. 6) has been obtained it is possible to decompose it at any altitude into four magneto-ionic modes associated with a homogeneous medium having the properties appropriate to that altitude. Calling S_i the magneto-ionic solution vectors, e may be written as:

$$e = \sum_{i=1}^{4} \beta_i S_i \tag{8}$$

where β_i are constants determined by

$$\beta_i = S_i^{-1} e \quad \text{and} \quad S_i^{-1} S_j = \delta_{ij} \quad \text{where } \delta = \text{Kronecker Delta} \tag{9}$$

Effecting this decomposition it is then possible to write at any altitude:

$$e = \begin{pmatrix} E_1^u \\ -E_2^u \\ \mathcal{H}_1^u \\ \mathcal{H}_2^u \end{pmatrix} + \begin{pmatrix} E_1^d \\ -E_2^d \\ \mathcal{H}_1^d \\ \mathcal{H}_2^d \end{pmatrix} \tag{10}$$

where u and d designate up and down travelling waves. Substituting the up or down travelling fields into (4) we define:

$$\vec{\pi}^{u,d} = \frac{1}{2} \operatorname{Re} (\vec{E}^{u,d} \times (\vec{H}^{u,d})^{*}) \tag{11}$$

It should be noted that in general

$$\vec{\pi} \neq \vec{\pi}^{u} + \vec{\pi}^{d} \tag{12}$$

Nevertheless, at high enough altitudes plots of the z component of (11) can serve as a crude measure of where the downcoming wave becomes unimportant. A somewhat more useful index, for our purposes, of where the downcoming wave becomes unimportant is predicated on the fact that at high altitudes the radio wave field, except in a very narrow angular band about the magnetic equator where quasi-transverse propagation applies, is almost totally in the outgoing whistler mode. In the whistler mode, the wave is circularly polarized such that $E_2 = iE_1$ and $\mathcal{H}_2 = i\mathcal{H}_1$. Thus, measures of departure of the total full wave field components from the outgoing whistler mode are given by the following quantities:

$$|\mathcal{H}_2 - i\mathcal{H}_1^u| \tag{13}$$

$$|E_2 - iE_1^u| \tag{14}$$

b. Reflection.

Westcott[16-20] in a series of papers has explored ionospheric reflection processes in the VLF band using the Darwin-Hartree[21,22] microscopic theory of re-radiation. In this theory, the re-radiation of the electron due to its acceleration produced by the total field is of primary importance and leads quite naturally to a conception of how each level of a horizontally stratified medium contributes to the final reflected field. Using the full wave program as described previously, the total fields are available throughout the ionosphere and examination of reflection processes using the microscopic theory is easily implemented. The essential formulas are summarized below.

The most important result of the microscopic theory for our purposes is that the reflected $\mathcal{H}_2^r$ field at the ground produced by the dipole layering up to height z is given by:

$$\mathcal{H}_2^r = \frac{ik}{2C\epsilon_0} \int_0^z (SP_3 + CP_1) e^{-ikCz}\, dz \tag{15}$$

where the P_i's are polarization vector components given by Eq. (3). By utilizing the relationship:

$$\frac{\vec{P}}{\epsilon_o} = \frac{1}{k^2}\left[\vec{\nabla}(\vec{\nabla}\cdot\vec{E}) - \nabla^2\vec{E}\right] - \vec{E} \tag{16}$$

the integral in Eq. (15) may be carried out with the result:

$$\mathcal{H}_2^r = \frac{1}{2}\left[(-\mathcal{H}_2 + E_1/C)\,e^{-ikCz}\right]_o^z \tag{17}$$

In the right hand side of Eq. (17), the $\vec{\mathcal{H}}$'s and $\vec{E}$'s are the full wave solutions and so the right hand side is readily calculable when the latter are available. Taking the derivative of Eq. (15) gives:

$$\frac{d\mathcal{H}_2^r}{dz} = \frac{ik}{2C\epsilon_o}\,(SP_3 + CP_1)\,e^{-ikCz} \tag{18}$$

Equation (18) states that the differential field re-radiated by a layer of thickness Δz at height z is $(d\mathcal{H}_2^r/dz)\Delta z$ where the quantity $d\mathcal{H}_2^r/dz$ is the reflection density for the y component of the magnetic field. Also, $\mathcal{H}_2^r$ given by Eq. (17) is the integrated dipole layer contribution to the reflected y component of the magnetic field.

4. RESULTS

A number of calculations have been made to illustrate the type of information available from full wave outputs as regards ionospheric absorption and reflection features of ELF waves. Many of the calculations have been made using the ambient day and night ionospheric models schematized in Fig. 1. The data for the region from ground to 100 km are from Knapp and those above 100 km are from Johnson. Some adjustments of the two sets of data .re required to avoid discontinuities at 100 km. A mass of 32 AMU is assigned to both the positive and negative ions. The collision frequencies as a function of altitude are listed in Tables I and II for daytime and nighttime, respectively. The collision frequencies vary exponentially with altitude between the tabulated increments.

No claim is made for the correctness of these profiles. Assignment of a single atomic mass unit to the ion population is clearly a compromise and the electron and ion densities are at best, only reasonable representations of mean conditions taken on a global basis. It is known that the profiles yield attenuation rates and field predictions in reasonable agreement with the Sanguine and Seafarer test measurements but at the same time seemingly suffer the shortcoming of overestimating the attenuation rate in the neighborhood of the fundamental Schumann resonance.

For those features of reflection and absorption which seem to be particularly sensitive to model choice, a number of other models will be examined as well. One of these will be the ambient nighttime model of Fig. 1 with the sporadic E layer superimposed. It is a layer about 5 km thick at the top and about 15 km thick at the base with a peak electron density enhancement factor of about 30 over that of the ambient. The

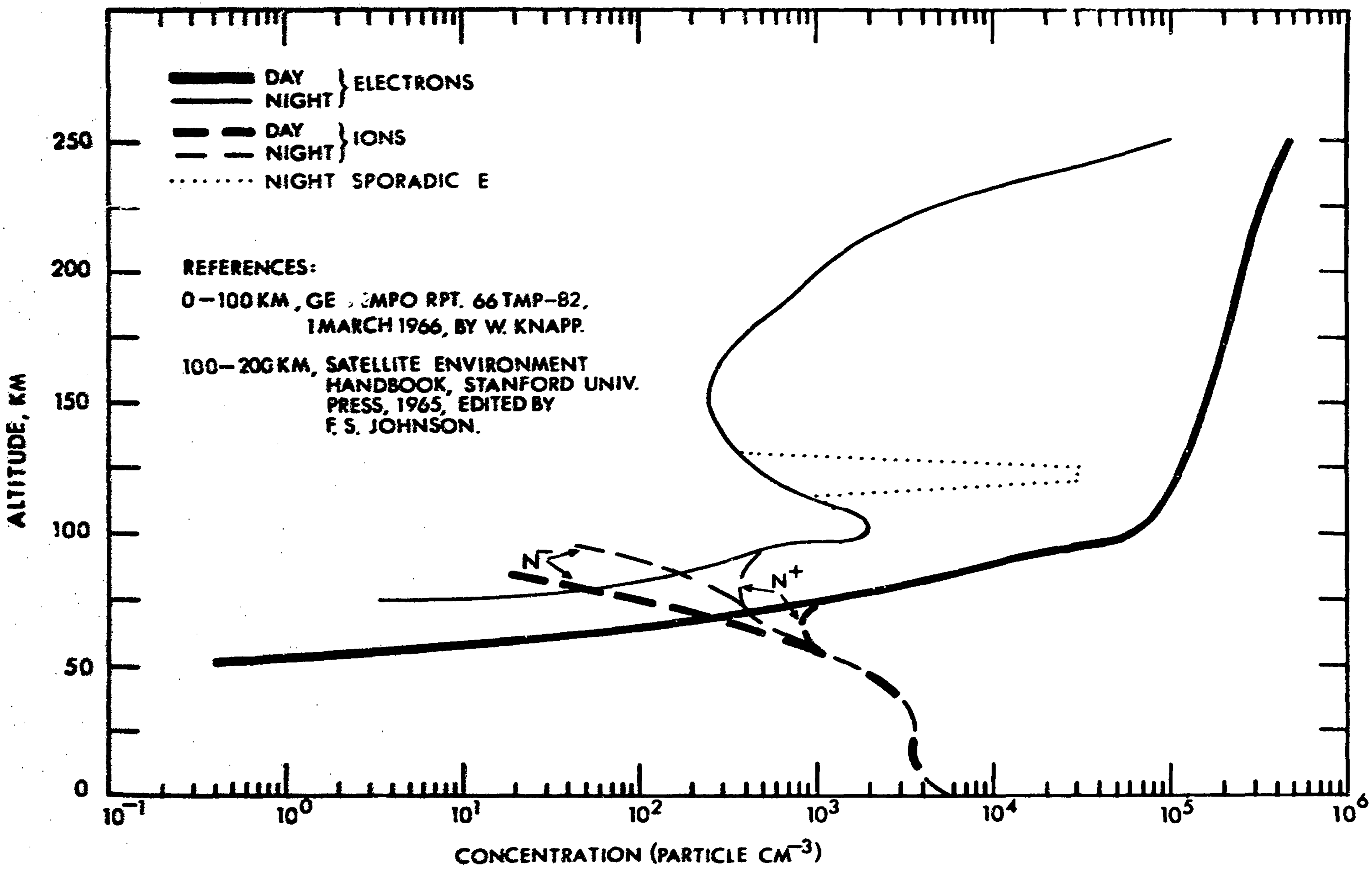

Fig. 1. Day and Night Ambient Profiles and Nighttime Sporadic E.

TABLE 1.

Daytime Ionospheric Electron and Ion Collision Frequency in Seconds^{-1} Versus Altitude

Altitude (km)	Electrons	Positive Ions	Negative Ions
150.	1.60×10^{3}	4.50×10^{1}	4.50×10^{1}
120.	1.00×10^{4}	3.00×10^{2}	3.00×10^{2}
100.	3.90×10^{4}	8.00×10^{3}	8.00×10^{3}
0.0	4.30×10^{11}	1.07×10^{10}	1.07×10^{10}

TABLE 2.

Nighttime Ionospheric Electron and Ion Collision Frequency in Seconds^{-1} Versus Altitude

Altitude (km)	Electrons	Positive Ions	Negative Ions
250.	1.05×10^{2}	4.50×10^{-1}	4.50×10^{-1}
225.	3.50×10^{1}	9.00×10^{-1}	9.00×10^{-1}
220.	3.00×10^{1}	1.00	1.00
210	3.30×10^{1}	1.30	1.30
200.	4.50×10^{1}	2.00	2.00
150.	1.60×10^{3}	4.50×10^{1}	4.50×10^{1}
120.	1.00×10^{4}	3.00×10^{2}	3.00×10^{2}
100.	3.90×10^{4}	8.00×10^{3}	8.00×10^{3}
0.0	4.30×10^{11}	1.07×10^{10}	1.07×10^{10}

layer was suggested in a private communication from T. R. Larsen of the Norwegian Defence Research Establishment. During the course of this section, description of, and results for the other ionospheres will be given. Although finite ground conductivities have been used in the calculations, for all practical purposes the results presented can be thought of as appropriate for an infinitely conducting ground.

Figures 2 through 4 show full wave absorption results for the daytime ambient profile of Fig. 1. Figure 2 is for 75 Hz, Fig. 3 for 45 Hz and Fig. 4 for 7.5 Hz and all of the curves are for an azimuth of propagation of 270° relative to magnetic north, a dip of 60° and a geomagnetic field of 0.5 Gauss. Height in kilometers is given on the vertical axis, relative heating loss per unit volume (Eq. 2) on the lower horizontal axis and integrated absorption measured in units of attenuation (i.e. dB/1000 km - Eq 5) is shown on the upper horizontal axis. Also shown are the total attenuations. The latter are certainly compatible with available measurements. Features common to the three figures are the low and high altitude absorption peaks. The low altitude absorption peaks occur at ≈55 km for 75 and 45 Hz and at ≈51 km for 7.5 Hz. If the profile densities and collision frequencies vary exponentially in the neighborhood of the absorption peaks and if the scale heights are invariant over the line profile then it is shown in Appendix A that the absorption line shape may be approximated by the Lorentzian line shape given by Eq. (A-8). Also, the position of the peak is given approximately

Fig. 2. Day Absorption and Attenuation at 75 hz. Azimuth = 270°, Dip = 60°, Geomagnetic Field = 0.5 Gauss.

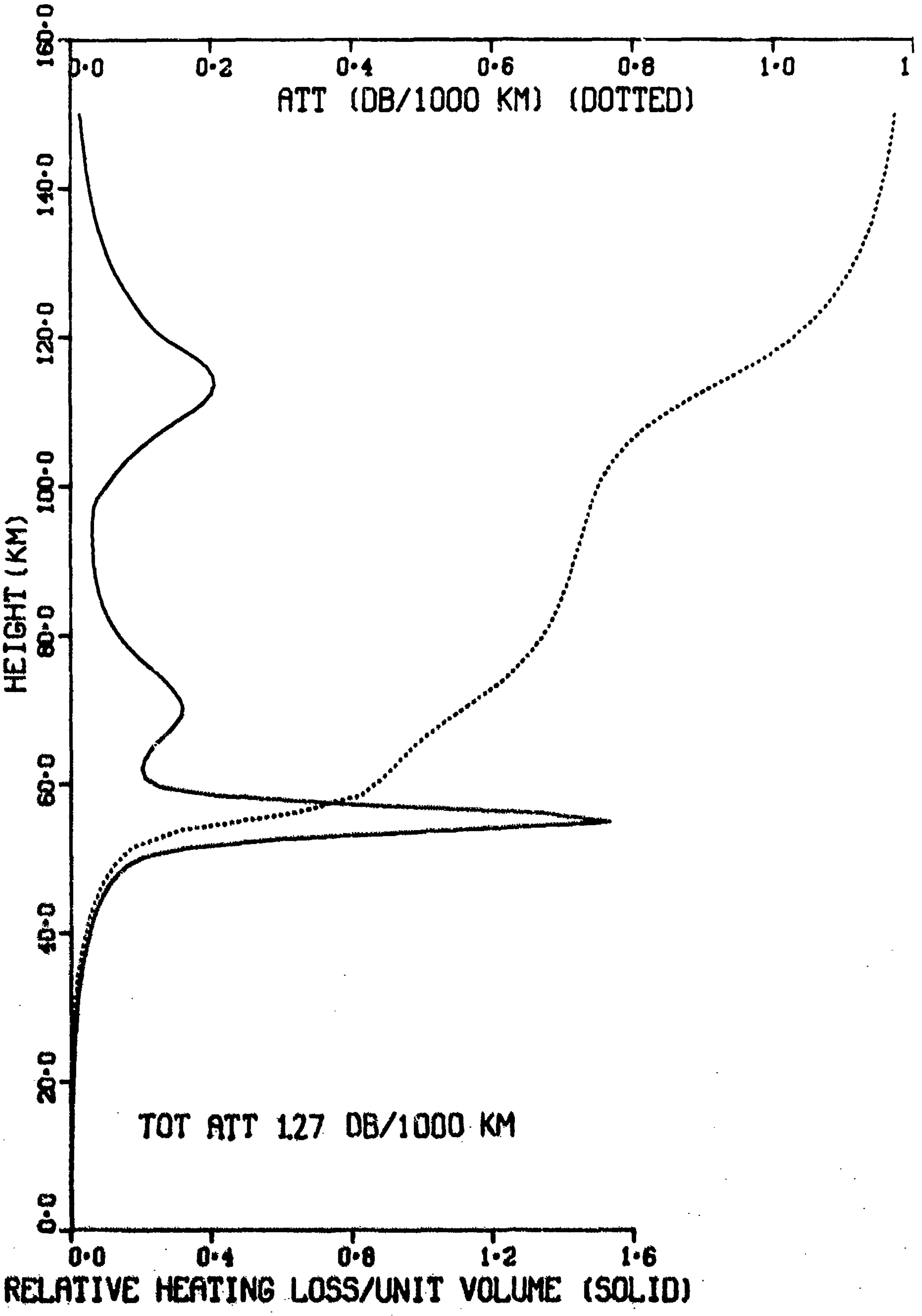

Fig. 3. Day Absorption and Attenuation at 45 Hz. Azimuth = 270°, Dip = 60°, Geomagnetic Field = 0.5 Gauss.

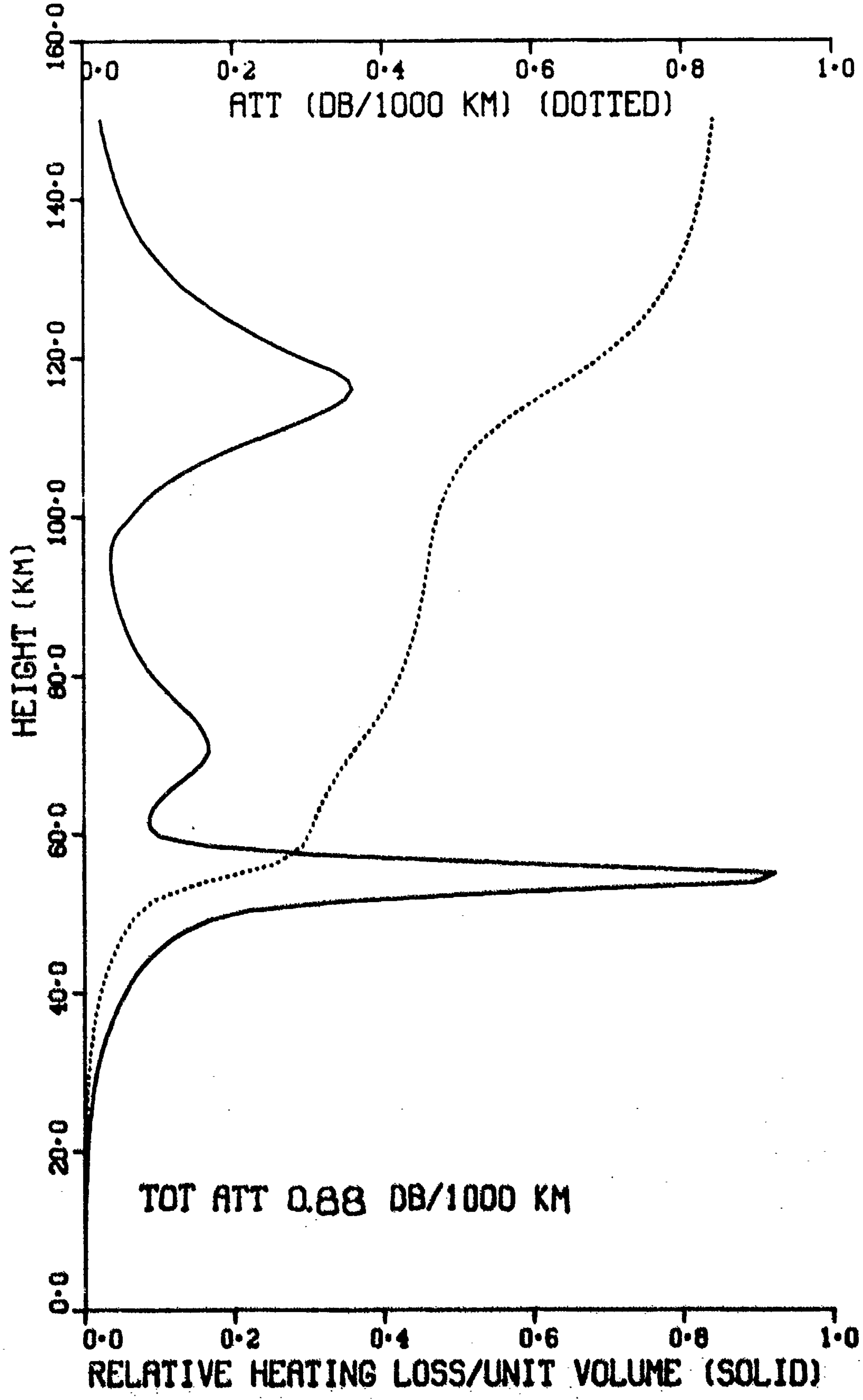

Fig. 4. Day Absorption and Attenuation at 7.5 Hz. Azimuth = 270°, Dip = 60°, Geomagnetic Field = 0.5 Gauss.

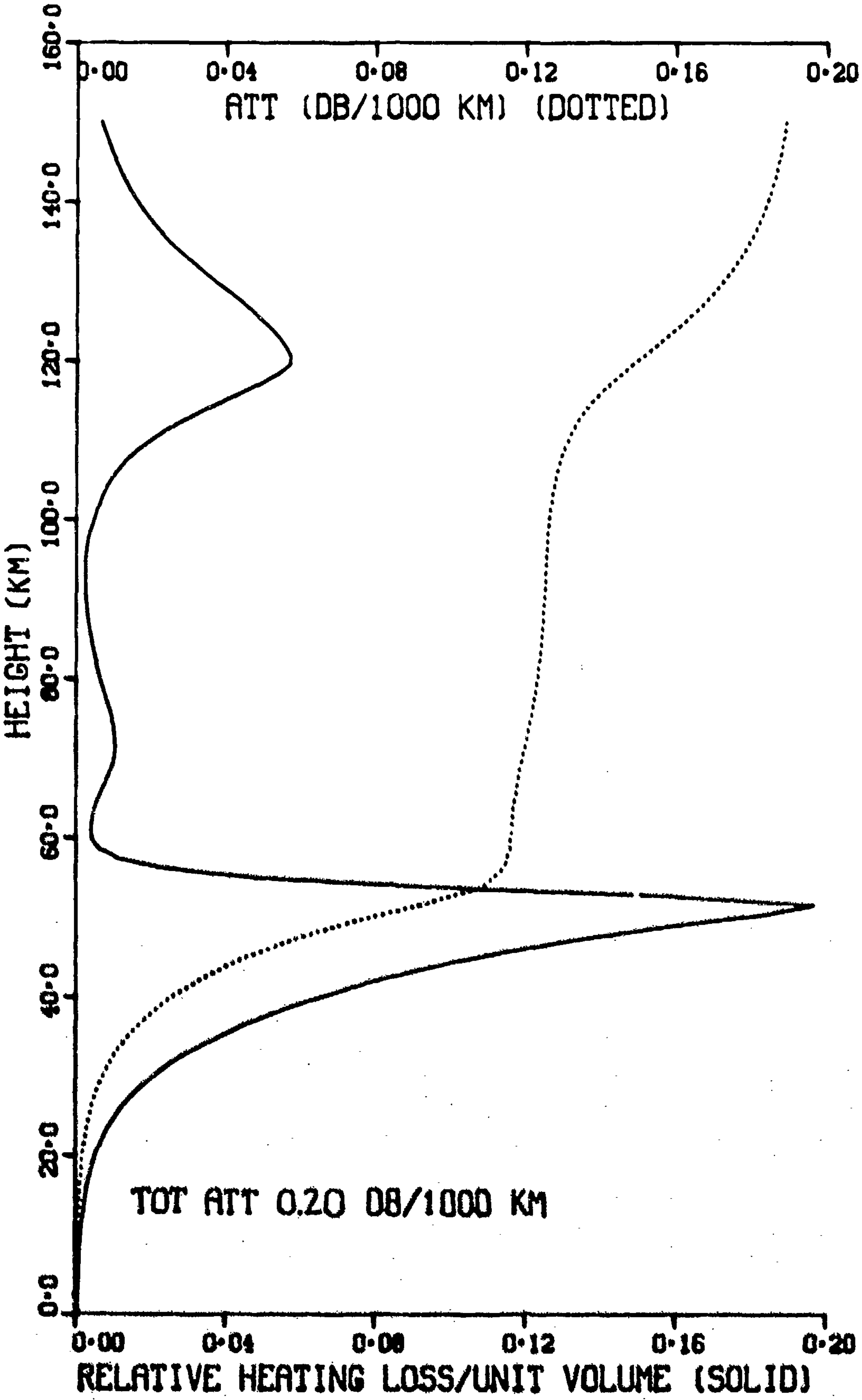

by Eq. (A-6). Comparisons of the full wave low altitude absorption lines (normalized to unity) with the Lorentzian lines are given in Figs. 5 through 7 for 75, 45 and 7.5 Hz. The first thing to observe is that the altitude where the low altitude absorption peaks is quite well predicted by Eq. (A-6). Apart from the wings of the lines, the agreement between the full wave output and the Lorentzian line shape given by Eq. (A-8) is excellent for the 75 Hz and 45 Hz cases but is poor for the 7.5 Hz case. This poor agreement results from several causes. First, the half width of the line is sufficiently broad that the assumption of invariant scale heights over the line is violated. Second, the asymmetry of the line could only be accounted for by retaining higher order terms in the expansion of the denominators of Eqs. (A-7) and (A-8).

The integrated effect of the low altitude absorption line (as measured in units of attenuation) has also been approximated in Appendix A by Eq. (A-13). In particular, the attenuation will be seen from (A-13) to be particularly sensitive to the species scale heights and their collision frequency scale heights in the neighborhood of the absorption peak. From Figures 2 through 4 it will be seen that the low altitude absorption contributes about 0.4 dB/1000 km to the attenuations at 75 Hz, about 0.3 dB/1000 km at 45 Hz and about 0.1 dB/1000 km at 7.5 Hz.

The high altitude absorption peaks occur at about 114 km for 75 Hz, about 116 km for 45 Hz and about 121 km for 7.5 Hz. If the profile densities and collision frequencies vary exponentially in the neighborhood of the absorption peaks and if the scale heights are invariant over the line profile then it is shown in Appendix B that the absorption line shape may be approximated by the Gaussian line shape given by Eq. (B-13).

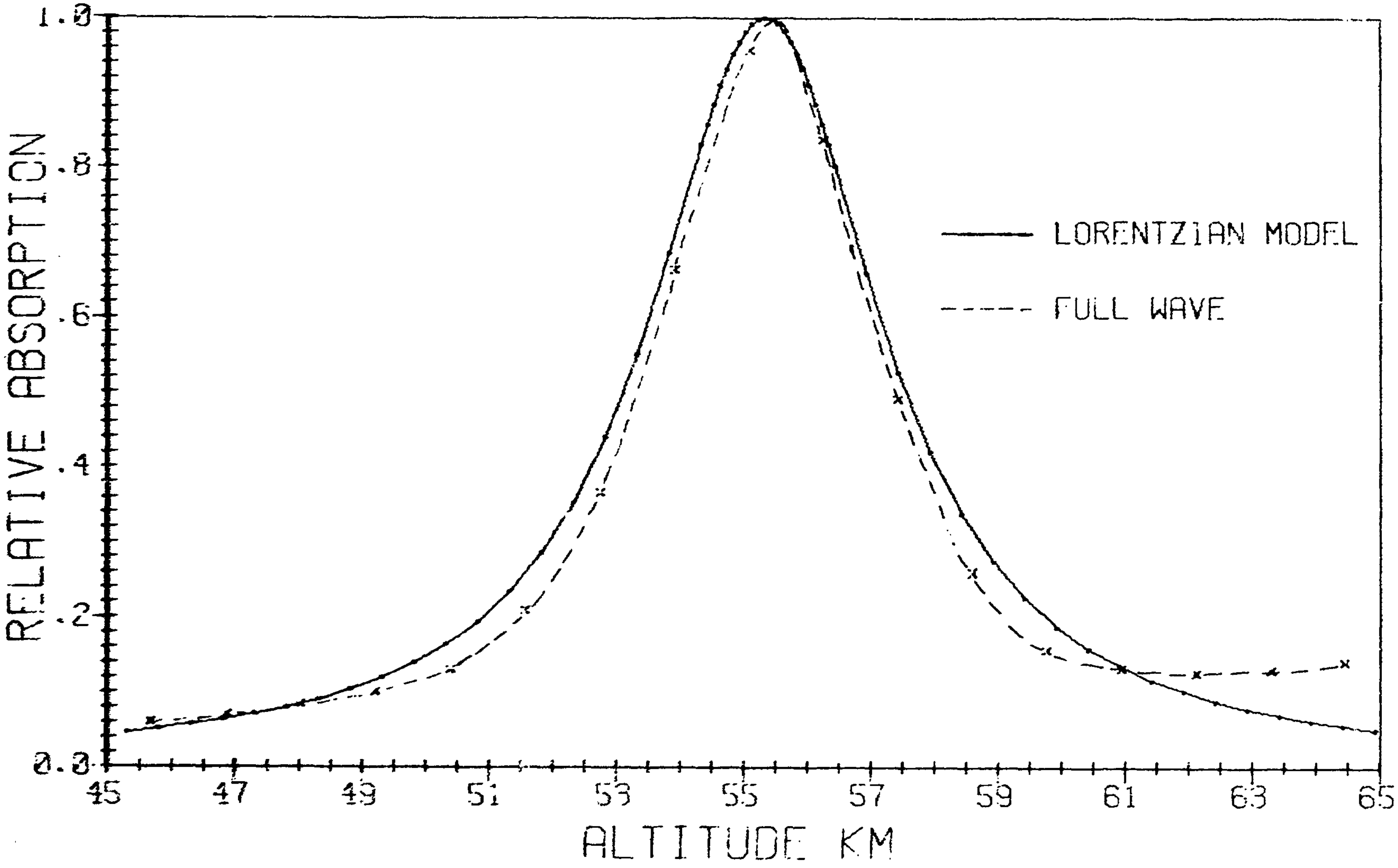

Fig. 5. Low Altitude Daytime Absorption Comparisons at 75 Hz.

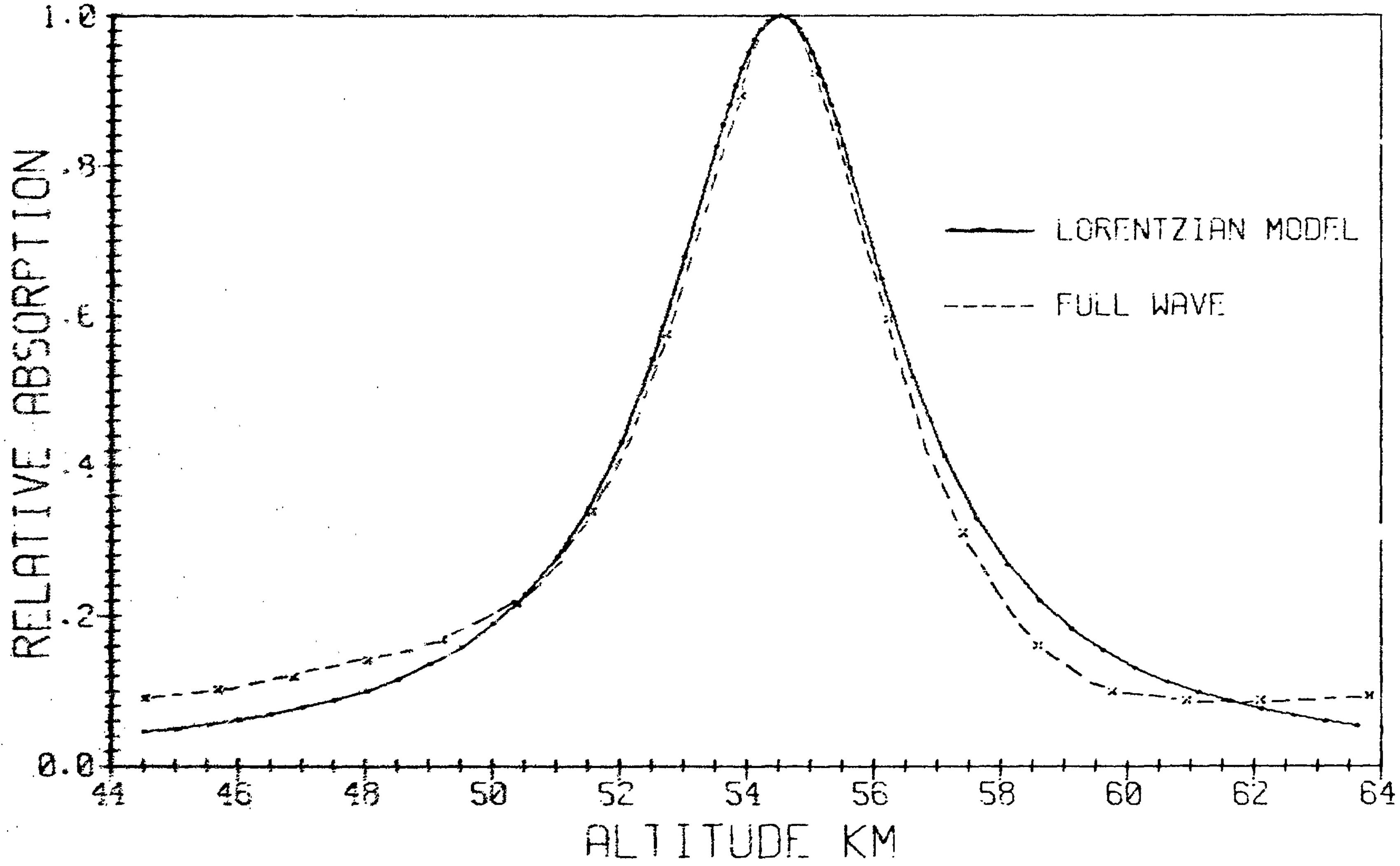

Fig. 6. Low Altitude Daytime Absorption Comparisons at 45 Hz.

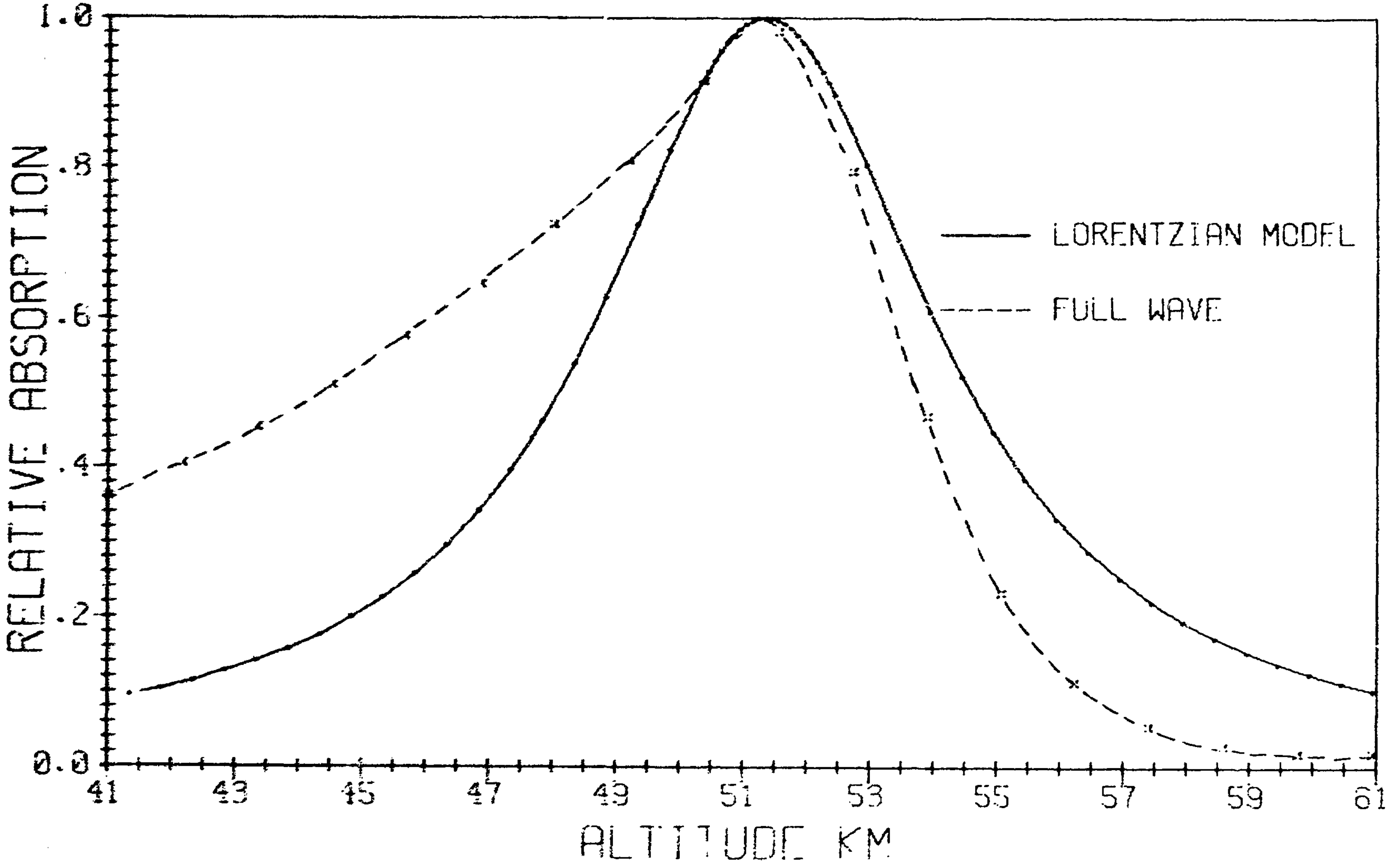

Fig. 7. Low Altitude Daytime Absorption Comparisons at 7.5 Hz.

Also, the position of the peak is given approximately by Eq. (B-12). Comparisons of the full wave absorption lines (normalized to unity) with the Gaussian lines are given in Figure 8 through 10 for 75, 45 and 7.5 Hz. Observe that the altitude where the high altitude absorption peaks is quite well predicted by Eq. (B-12). Apart from the wings of the lines, the agreement between the full wave output and the Gaussian line shape given by Eq. (B-13) is good for the 75 and 45 Hz cases but is poor for the 7.5 Hz case. As was the case with the low altitude absorption line comparisons, this poor agreement results from the fact that the line is sufficiently broad to invalidate the assumption of invariant scale heights. Furthermore, the marked asymmetry of the 7.5 Hz high altitude line could only be accounted for by retaining higher order terms in the expansion of the exponent of Eq. (B-13).

From Figures 2 through 4 it will be seen that the high altitude absorption contributes about 0.2 dB/1000 km to the attenuation at 75 Hz, about 0.4 dB/1000 km at 45 Hz and about 0.06 dB/1000 km at 7.5 Hz (of course it may be one's preference to include these losses as part of a leakage loss out of the top of the guide). Unlike the low altitude absorption, it is not an easy task to give an approximate estimate of the integrated absorption associated with the high altitude line because it depends upon the transmission through the D and E layers. Similarly, the intermediate altitude absorption lines common to Figures 2 through 4 are not readily amenable to analysis since they occur in a region over which upgoing and downgoing magneto-ionic components coexist in variable proportions.

Figures 11 through 13 show full wave absorption results for the nighttime ambient profile of Figure 1. Figure 11 is for 75 Hz, Figure 12

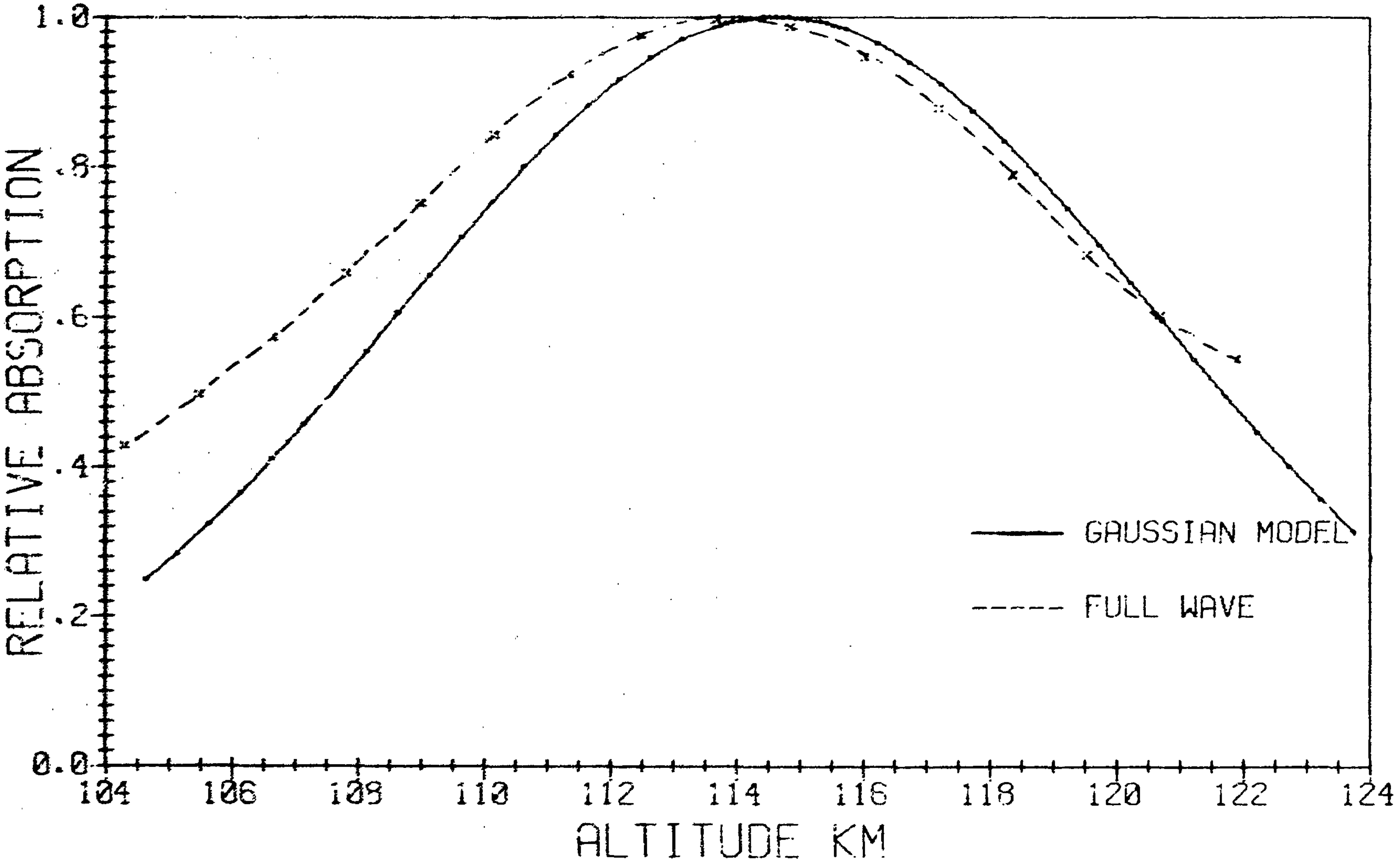

Fig. 8. High Altitude Daytime Absorption Comparisons at 75 Hz.

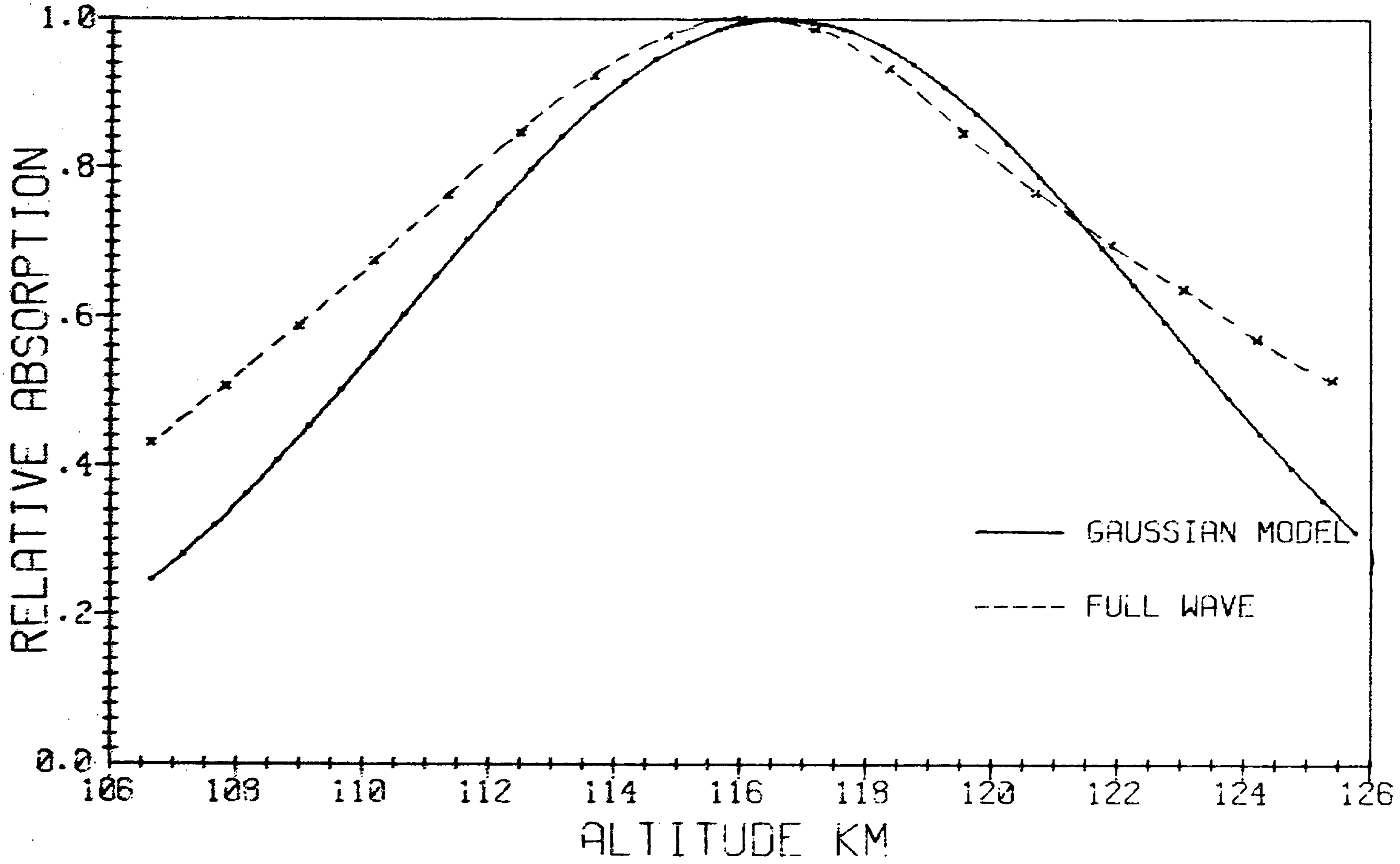

Fig. 9. High Altitude Daytime Absorption Comparisons at 45 Hz.

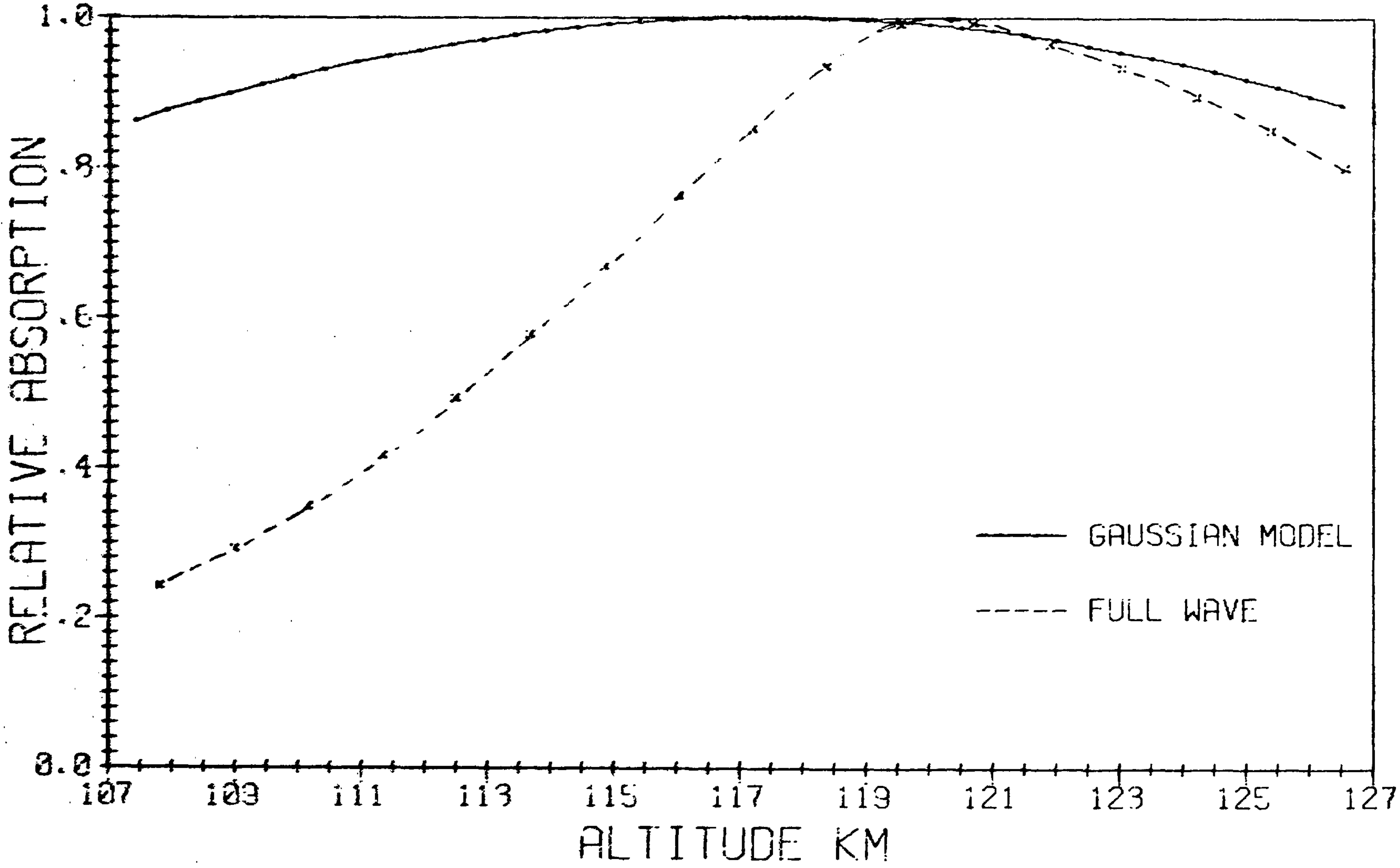

Fig. 10. High Altitude Daytime Absorption Comparisons at 7.5 Hz.

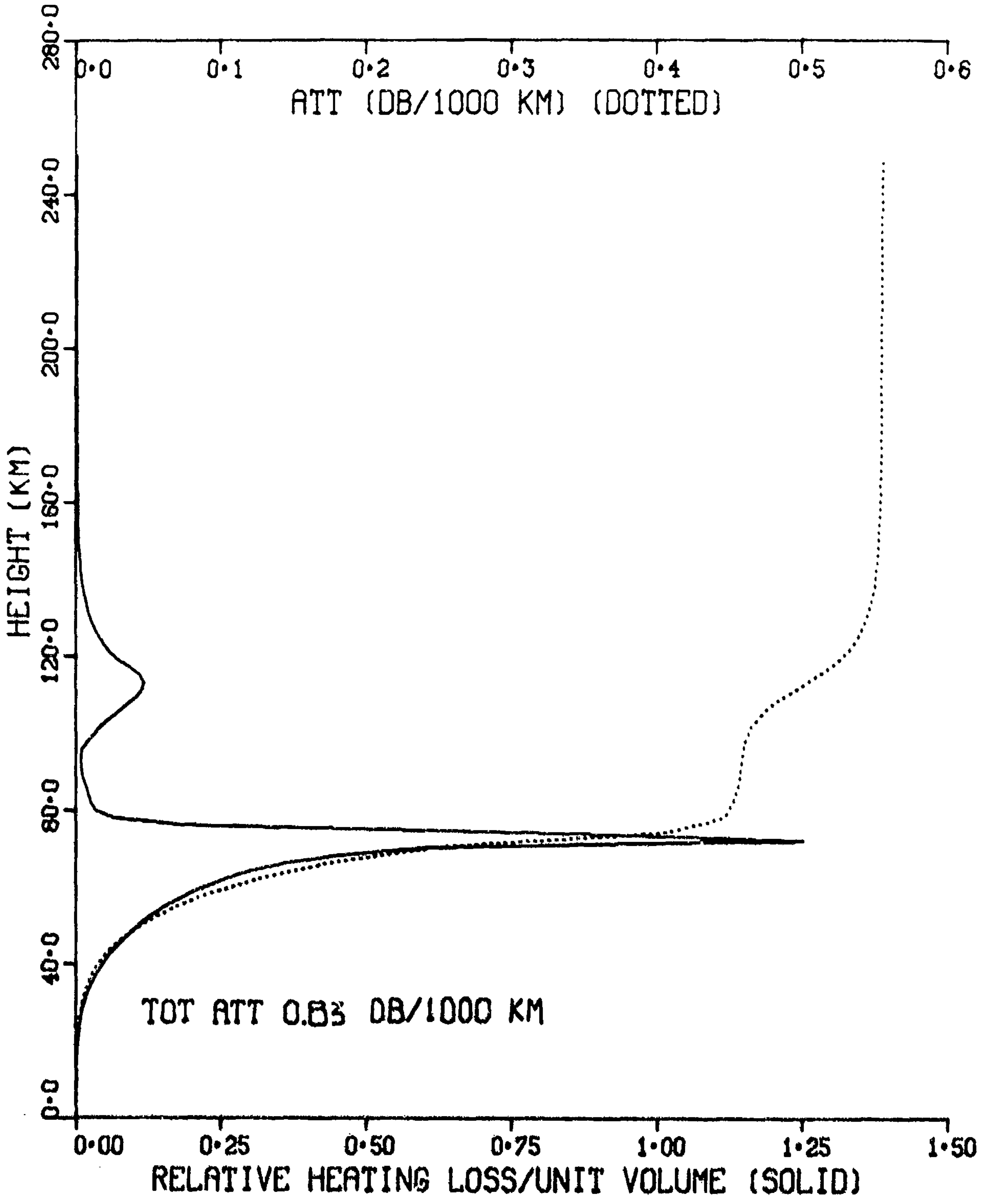

Fig. 11. Night Absorption and Attenuation - 75 Hz. Azimuth = 270°, Dip = 60°, Geomagnetic Field = 0.5 Gauss.

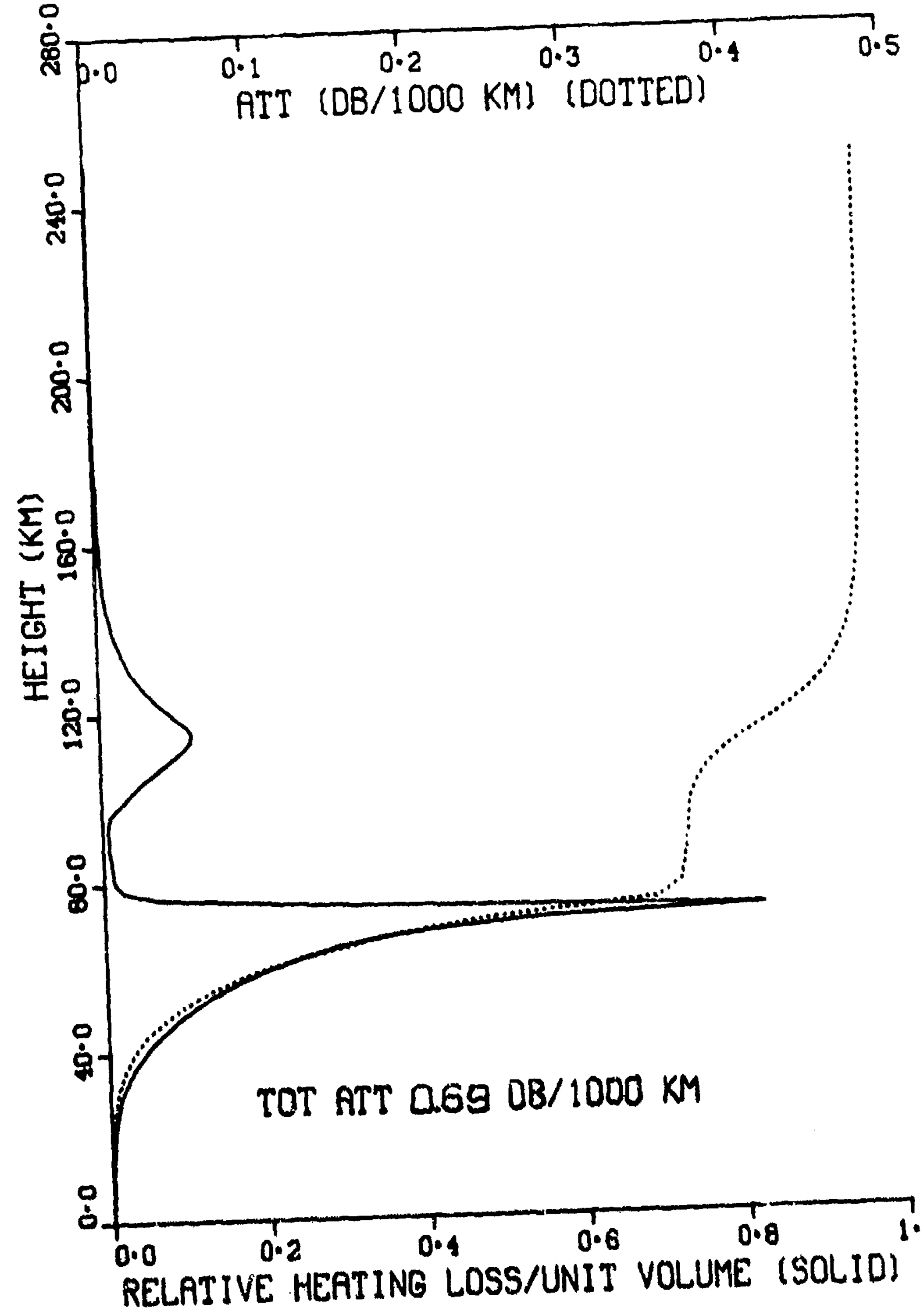

Fig. 12. Night Absorption and Attenuation - 45 Hz. Azimuth = 270°, Dip = 60°, Geomagnetic Field = 0.5 Gauss.

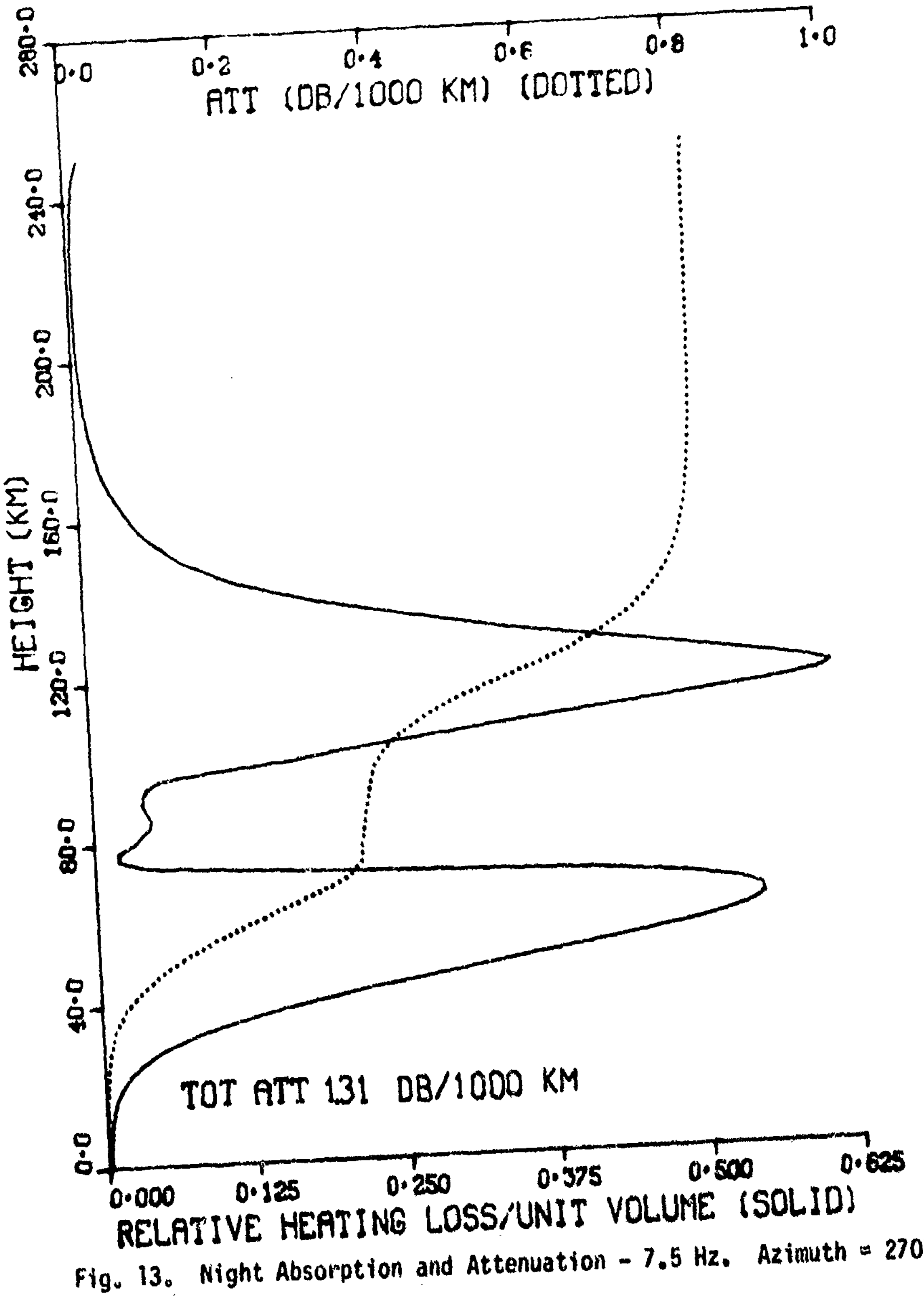

Fig. 13. Night Absorption and Attenuation - 7.5 Hz. Azimuth = 270°, Dip = 60°, Geomagnetic Field = 0.5 Gauss.

for 45 Hz and Figure 13 for 7.5 Hz and all of the curves are for an azimuth of propagation of 270^0 relative to magnetic north a dip of 60^0 and a geomagnetic field strength of 0.5 Gauss. The curves show the same quantities as those of Figures 2 through 4 for the daytime profiles. The total attenuations shown on the figures are in the 45 and 75 Hz cases, compatible with available measurements whereas the attenuation rate of 1.3 dB/1000 km for 7.5 Hz seems quite inconsistent with the observation of Schumann resonances, although the latter, of course, depend upon a global average for which the mid latitude nighttime prototype of Figure 1 may play a relatively minor role. At any rate the nighttime profile of Figure 1 can at least be thought of as empirical for Seafarer band predictions.

As was the case for the daytime profile, Figures 11 through 13 show the common features of low and high altitude absorptions. The low altitude absorption peaks occur at ≈72 km for 75 and 45 Hz and at ≈62 km for 7.5 Hz. As discussed in Appendix A, the analysis given there, with very minor alteration, can also be applied at least approximately to the nighttime low altitude absorption. Comparisons of the full wave low altitude absorption line locations and shapes (normalized to unity) with the Lorentzian line shapes of Appendix A are given in Figures 14 through 16. As was the case with the daytime results, the locations of the peaks are quite well predicted by the simple theory of Appendix A. However, the full wave low altitude line shapes for the nighttime case study show more asymmetry, particularly at 75 and 45 Hz, than did the daytime results. Still, if wing effects are discounted the agreement at all frequencies is fairly good. From Figures 11 through 13 it will be seen that the contribution of the low altitude absorption line is ≈0.5 dB/1000 km at

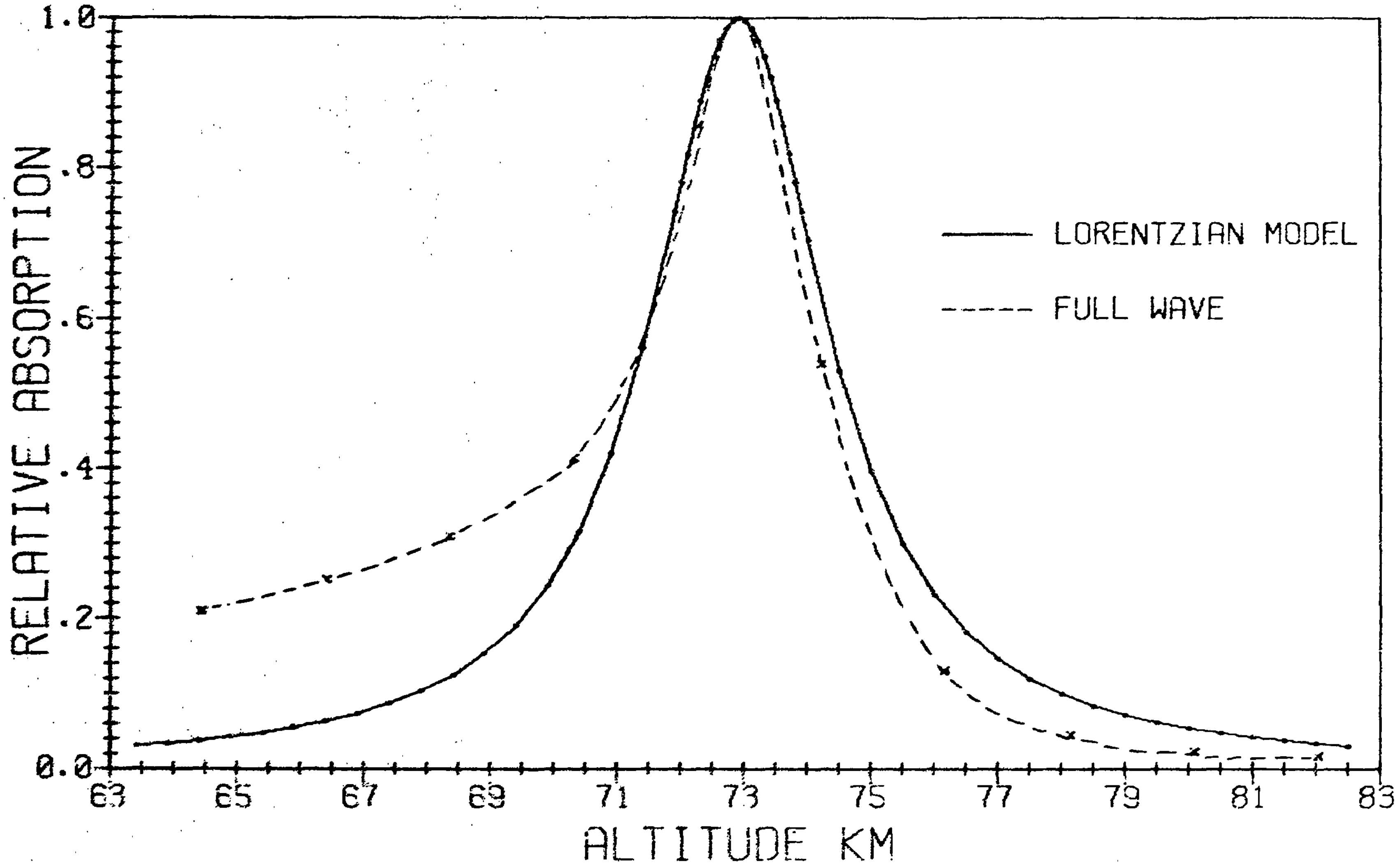

Fig. 14. Low Altitude Nighttime Absorption Comparisons at 75 Hz.

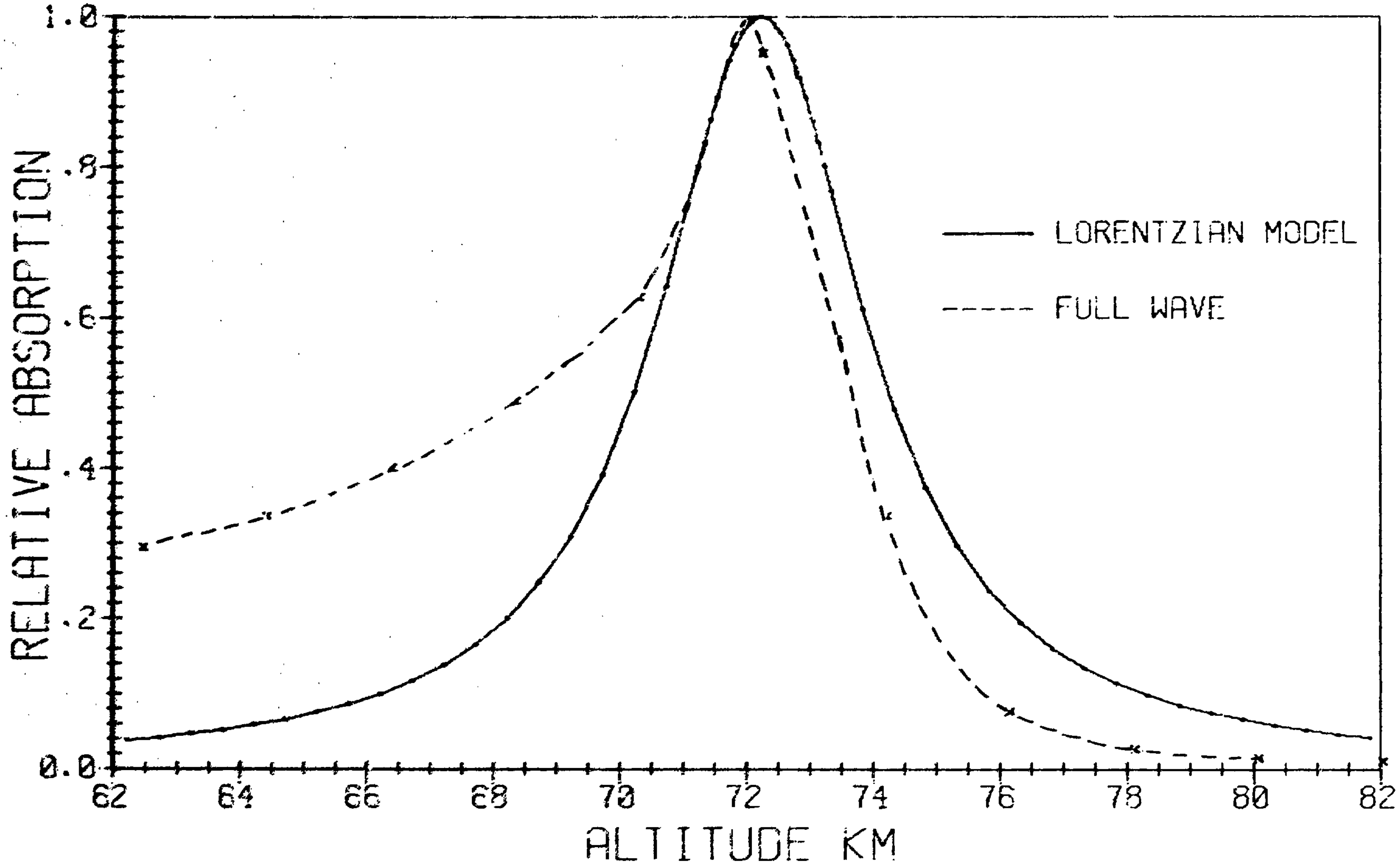

Fig. 15. Low Altitude Nighttime Absorption Comparisons at 45 Hz.

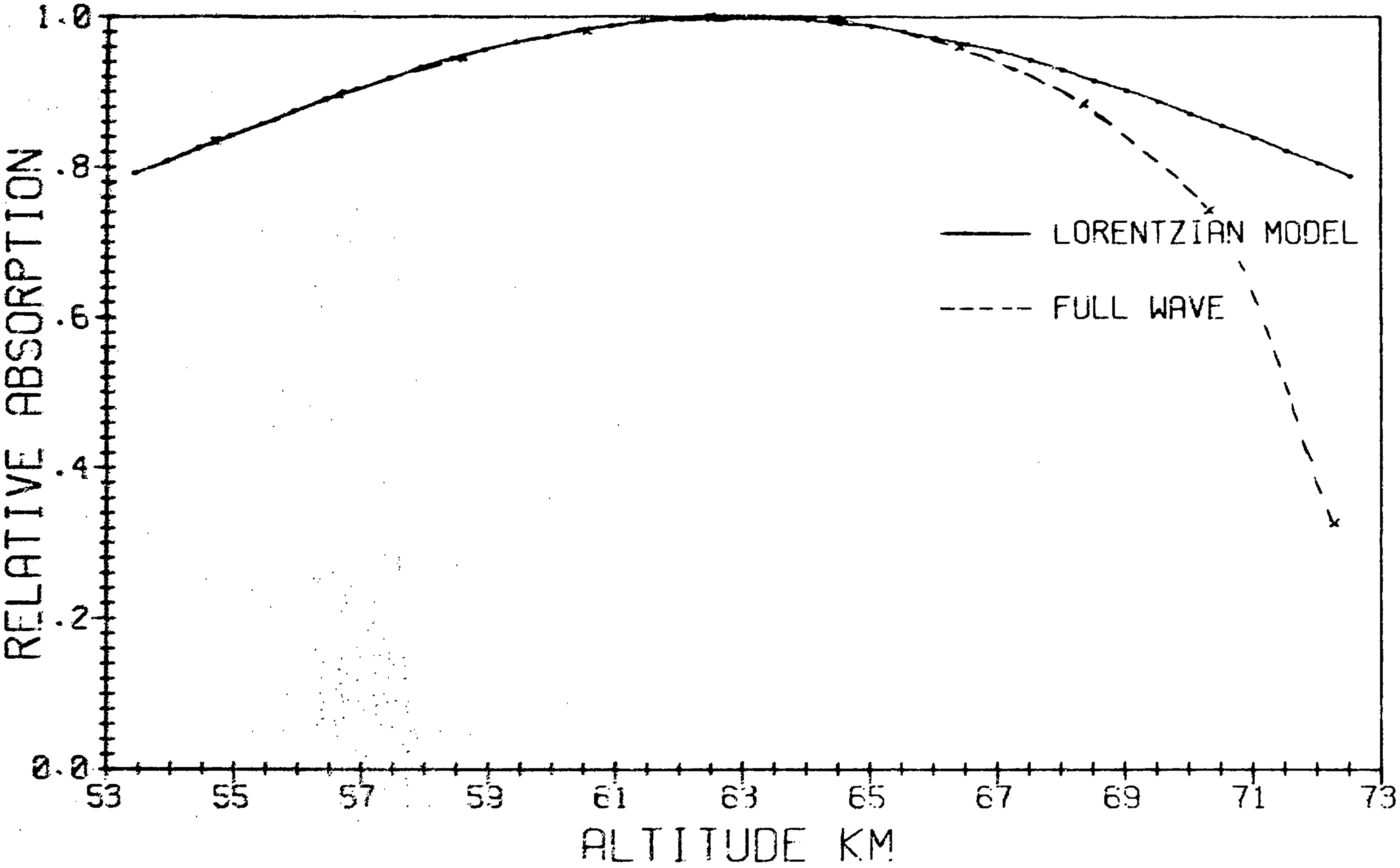

Fig. 16. Low Altitude Nighttime Absorption Comparisons at 7.5 Hz.

75 Hz, ≈0.4 dB/1000 km at 45 Hz and ≈0.4 dB/1000 km at 7.5 Hz.

The high altitude absorption peaks occur at ≈113 km for 75 Hz, at ≈115 km for 45 Hz and at ≈119 km for 7.5 Hz. Comparisons of the full wave line shapes (normalized to unity) with the Gaussian line shapes predicted by the simple theory of Appendix B are shown in Figures 17, 18 and 19. Again if wing effects are discounted, the agreement is quite good with the 7.5 Hz being again the worst of the three frequencies considered.

From Figures 11 through 13 it will be seen that the contribution of the high altitude absorption to the attenuation is ≈0.1 dB/1000 km at 75 and 45 Hz and ≈0.4 dB/1000 km at 7.5 Hz. The latter figure is an indication of the quite appreciable energy penetrating the nighttime ambient ionosphere of Figure 1 to altitudes of 120 km and above. Further evidence of this will be forthcoming.

Figures 20 and 21 show results relevant to reflection properties of the nighttime ambient profiles of Figure 1 as looked at from the point of view of the Darwin-Hartree[21,22] re-radiation theory as discussed in section 3. The figures apply to the same geomagnetic conditions as Figures 11 through 13 and more particularly Figure 20 is for 75 Hz and Figure 21 is for 45 Hz. The vertical scale in each instance is the height in km. The upper horizontal scale applies to the solid curve (Eq. (17) of section 3) and to the dotted curve (Eq. (13) of section 3). The lower horizontal scale applies to the dashed curve (Eq. (4) of section 3). The solid curve represents the buildup of the magnitude of the y component of the reflected $\mathcal{H}$ field at the ground due to the integrated effect of the dipole layer structure below the height indicated on the vertical axis. Because of the normalization used, the value of the magnitude of

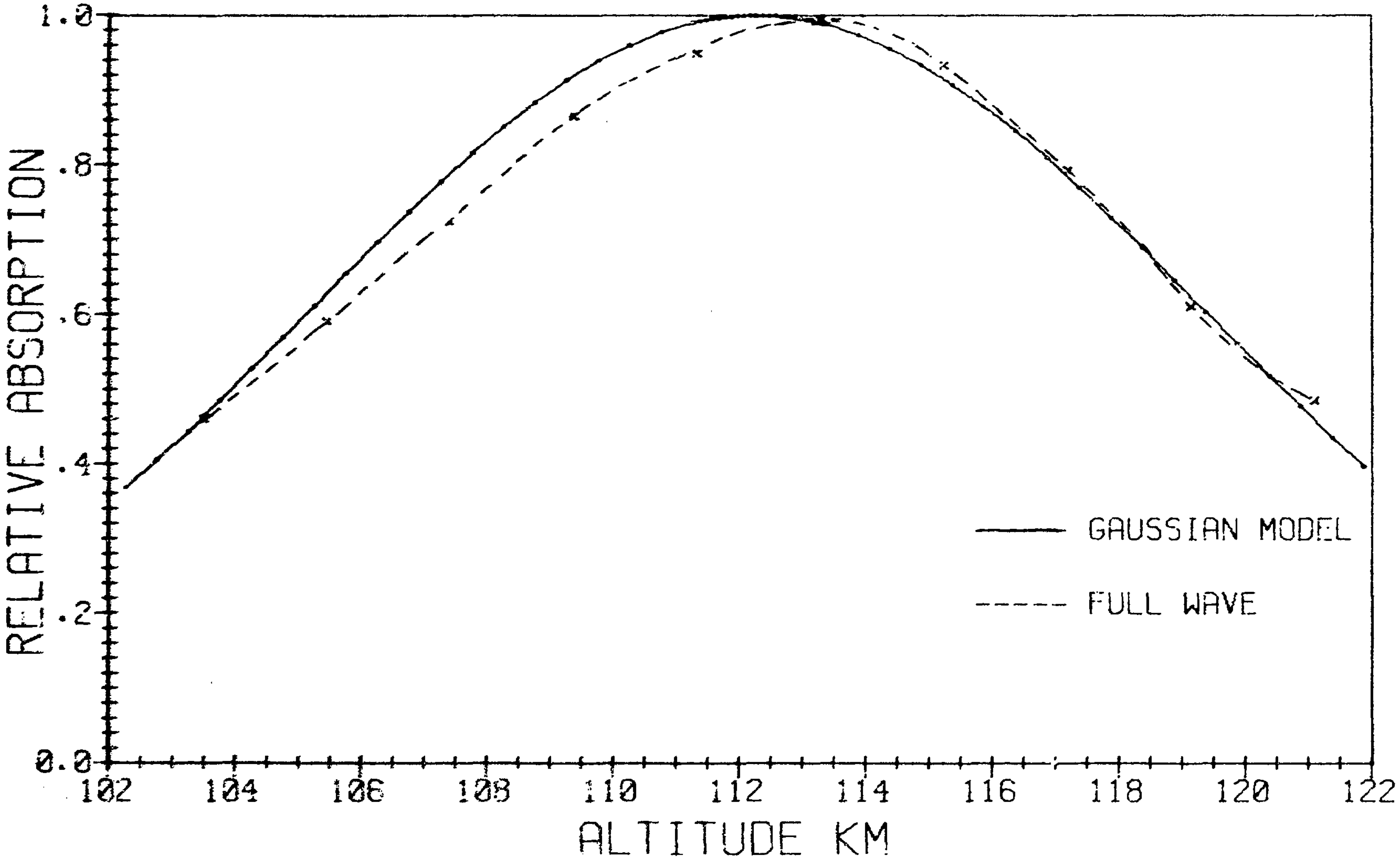

Fig. 17. High Altitude Nighttime Absorption Comparisons at 75 Hz.

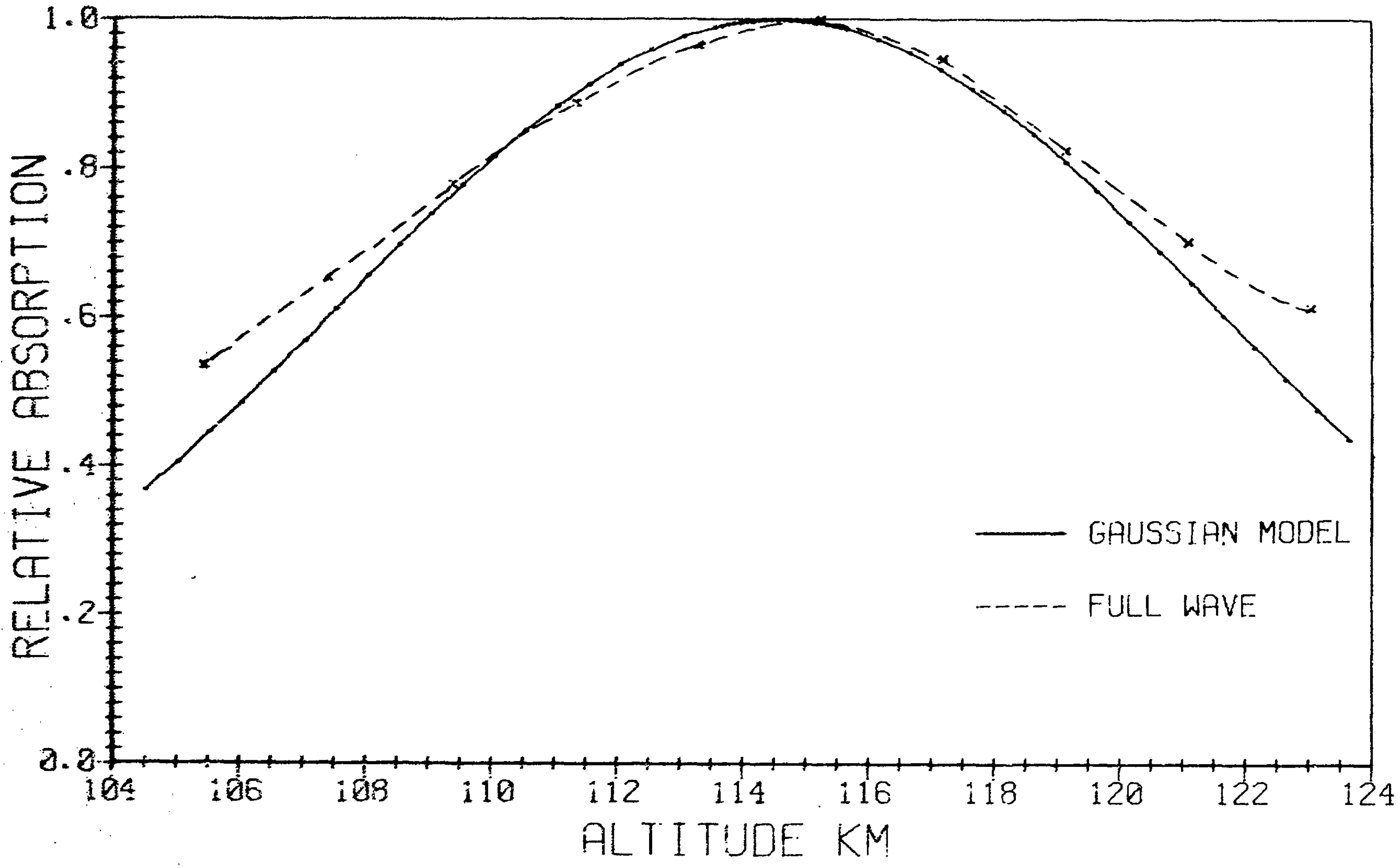

Fig. 18. High Altitude Nighttime Absorption Comparisons at 45 Hz.

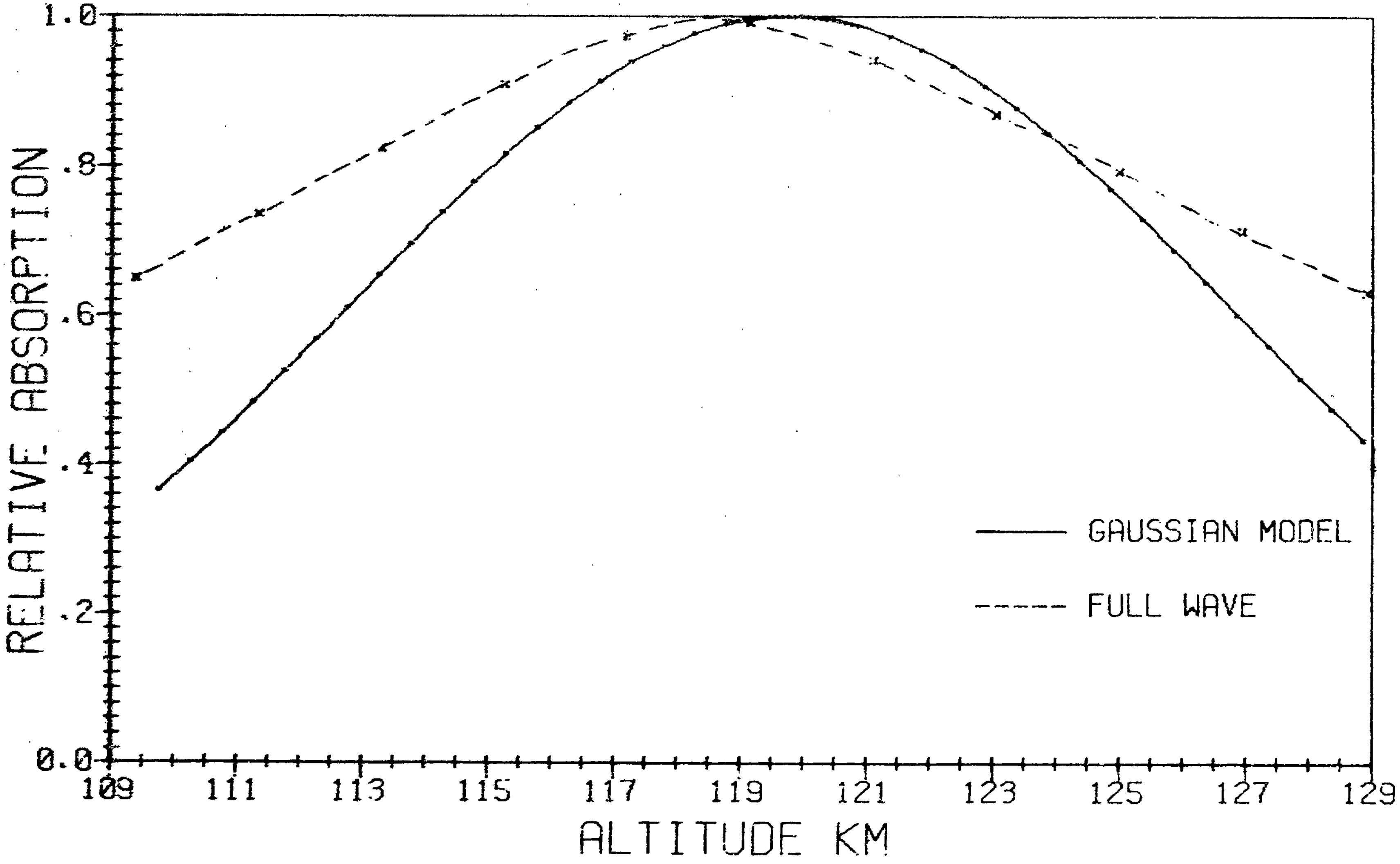

Fig. 19. High Altitude Nighttime Absorption Comparisons at 7.5 Hz.

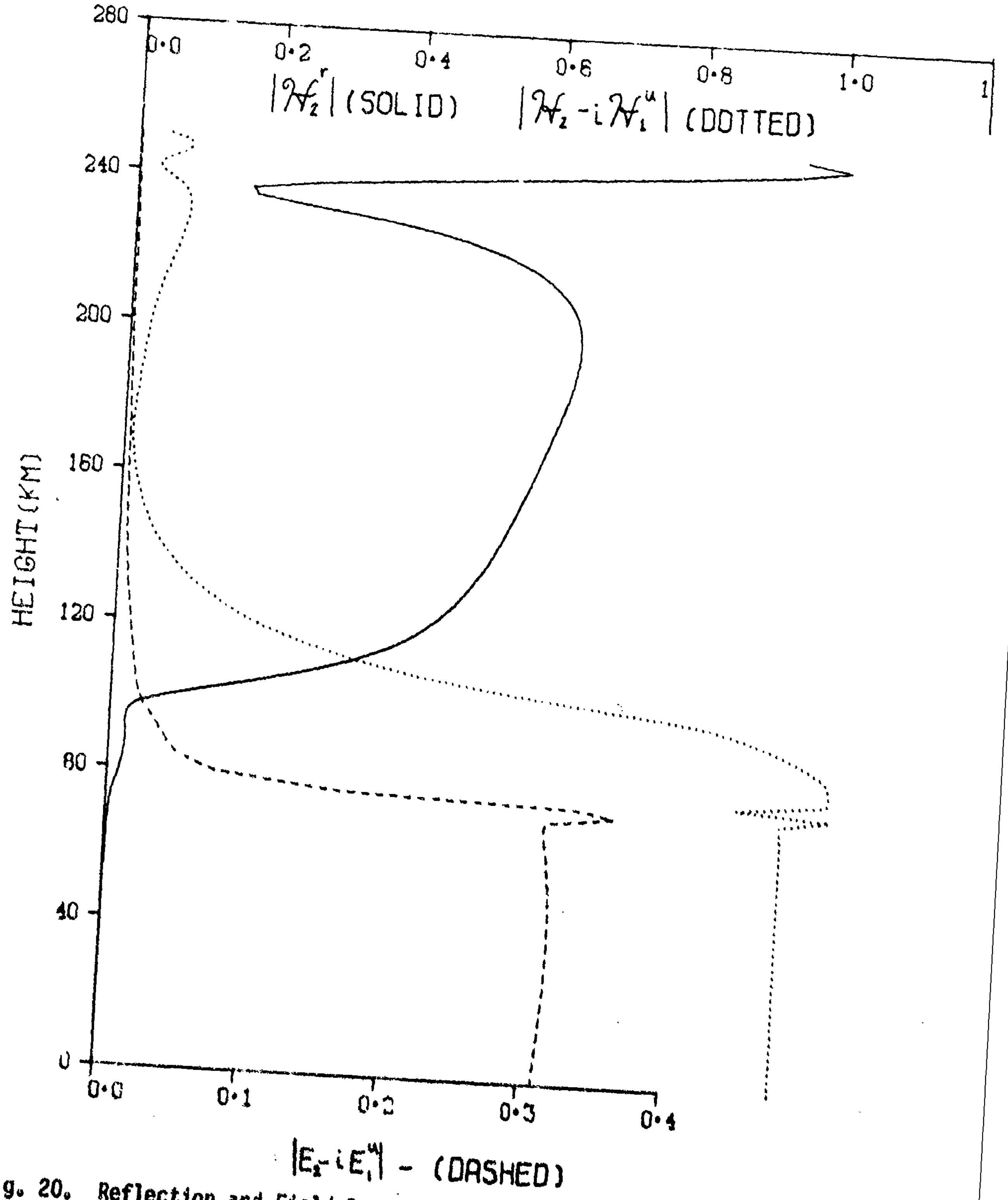

Fig. 20. Reflection and Field Penetration Properties for Night at 75 Hz. Azimuth = 270°, Dip = 60°, Geomagnetic Field = 0.5 Gauss.

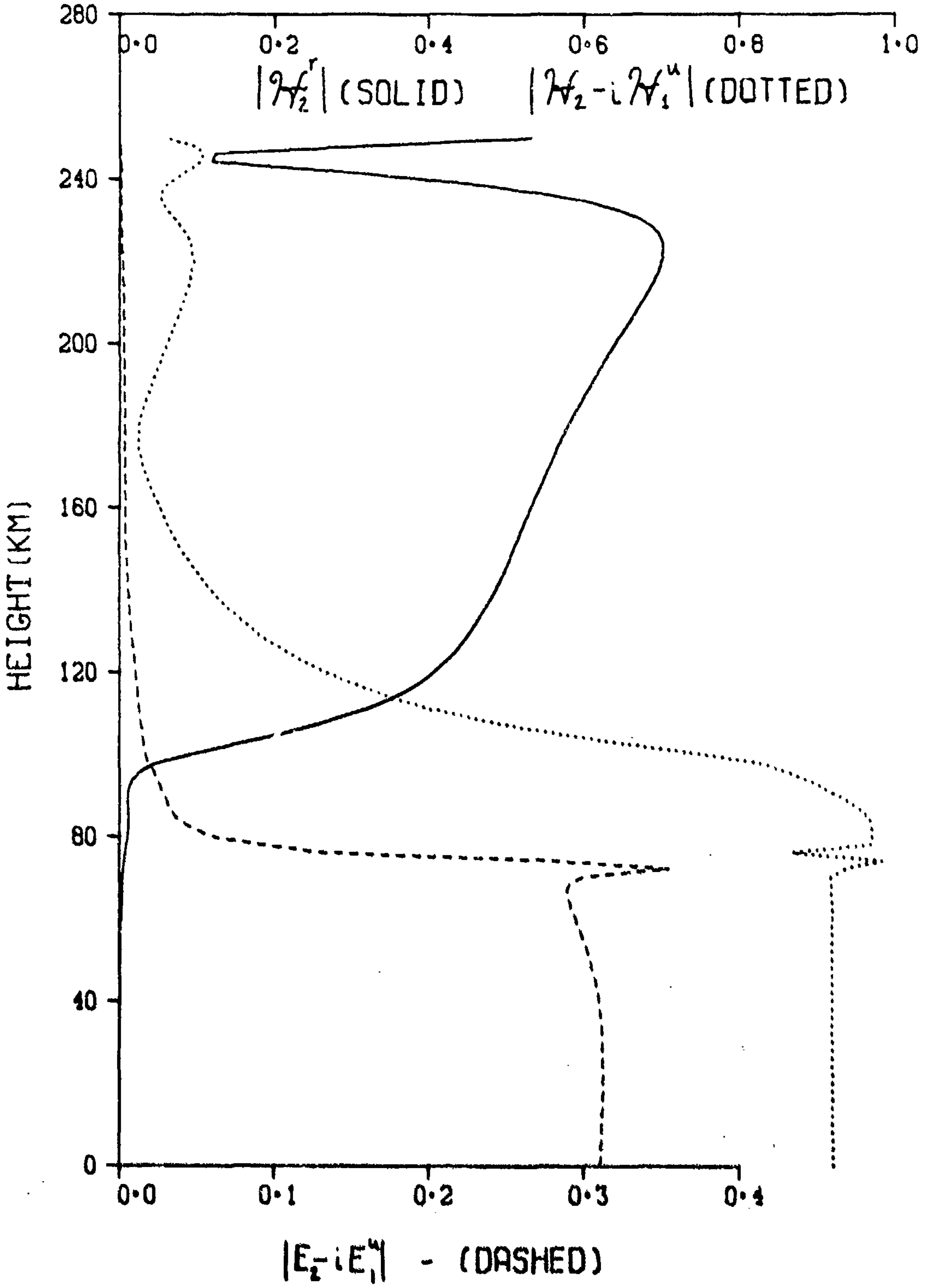

Fig. 21. Reflection and Field Penetration Properties for Night at 45 Hz. Azimuth = 270°, Dip = 60°, Geomagnetic Field = 0.5 Gauss.

the y component of the reflected $\mathcal{H}$ field at the ground associated with the re-radiation from the total ionosphere is 0.5. The dotted curve is the magnitude of $\mathcal{H}_2 - i\mathcal{H}_1^u$ and the dashed curve is the magnitude of $E_2 - iE_1^u$ where the field components are either full wave components or decompositions thereof as discussed in section 3. Thus the dotted and dashed curves may be thought of as measures of the departure of the full wave solutions from the outgoing whistler mode, measures which are meaningful principally at high altitudes, where the total field is expected to be in the outgoing whistler mode.

The solid curve of Figure (20) illustrates, then, that the buildup of the magnitude of the y component of the reflected $\mathcal{H}$ field at the ground begins slowly around 70 km, is quite rapid in the 95 to 120 km range and attains in magnitude its fully developed value of 0.5 at about 133 km. A measure of the integrated contribution of the ionosphere above this height to the y component of the reflected $\mathcal{H}$ field at the ground is the departure of its phase from its fully developed value of 0.0^o. This departure in the case of Figure (20)is known from the full wave output to be only about 11^o and so we interpret this as indicating that the reflection as looked at from the re-radiation point of view is in large measure developed by the ionosphere below the 133 km height, despite the fact that the solid curve does not asymptotically level off beyond there to its final value of 0.5. A necessary (but not sufficient) condition for this to be a valid interpretation is that there be no appreciable downcoming wave above 133 km. That this is in fact the case is indicated by the dashed and dotted curves. These curves show that the fields above about 130 km are very nearly described by the outgoing whistler mode. The large amplitude oscillatory phase of the solid curve above

200 km is due to this whistler mode penetration coupled with the large increase in the electron density associated with the F layer (see Figure 1).

The interpretation of Figure (21) which applies to 45 Hz, not surprisingly, is very much the same as that of Figure (20). In this case the magnitude of the y component of the reflected $\mathcal{H}$ field at the ground attains the value of 0.5 at about 146 km. At that altitude the phase departure of the y component of the reflected $\mathcal{H}$ field at the ground is about 10^0 from its final value of 0.0^0. Thus, as before, it is concluded that the reflection from the re-radiation point of view is in large measure developed by the ionosphere below about 146 km.

An alternative display of the levels contributing to the reflection is given in Figures (22) and (23) where the magnitude of the $\mathcal{H}_2$ reflected field density $d\mathcal{H}_2^r/dz$ as defined by Eq. (18) has been plotted. Also shown on the plots are the relative heating losses previously shown in Figures 11 and 12. The large amplitude increase in $|d\mathcal{H}_2^r/dz|$ above 200 km is discounted for the reasons cited above. It is due to polarizations associated with outgoing (WKB like) wave penetrating the F region and on the basis of the preceding discussion is known to contribute little to the integrated reflected $\mathcal{H}_2$ field at the ground. Thus the major reflection comes in the case of the 75 Hz wave from the region about the peak at about 103 km. In the case of the 45 Hz wave the major reflection comes from the region about the peak at about 102 km. The half widths in both cases are about 20 km. Figures (22) and (23) illustrate quite graphically the significant regions as regards both reflection and absorption.

Figure (24) shows reflection information for the nighttime profile at 7.5 Hz. The solid curve illustrates the buildup of the magnitude of the y component of the reflected $\mathcal{H}$ field at the ground due to the

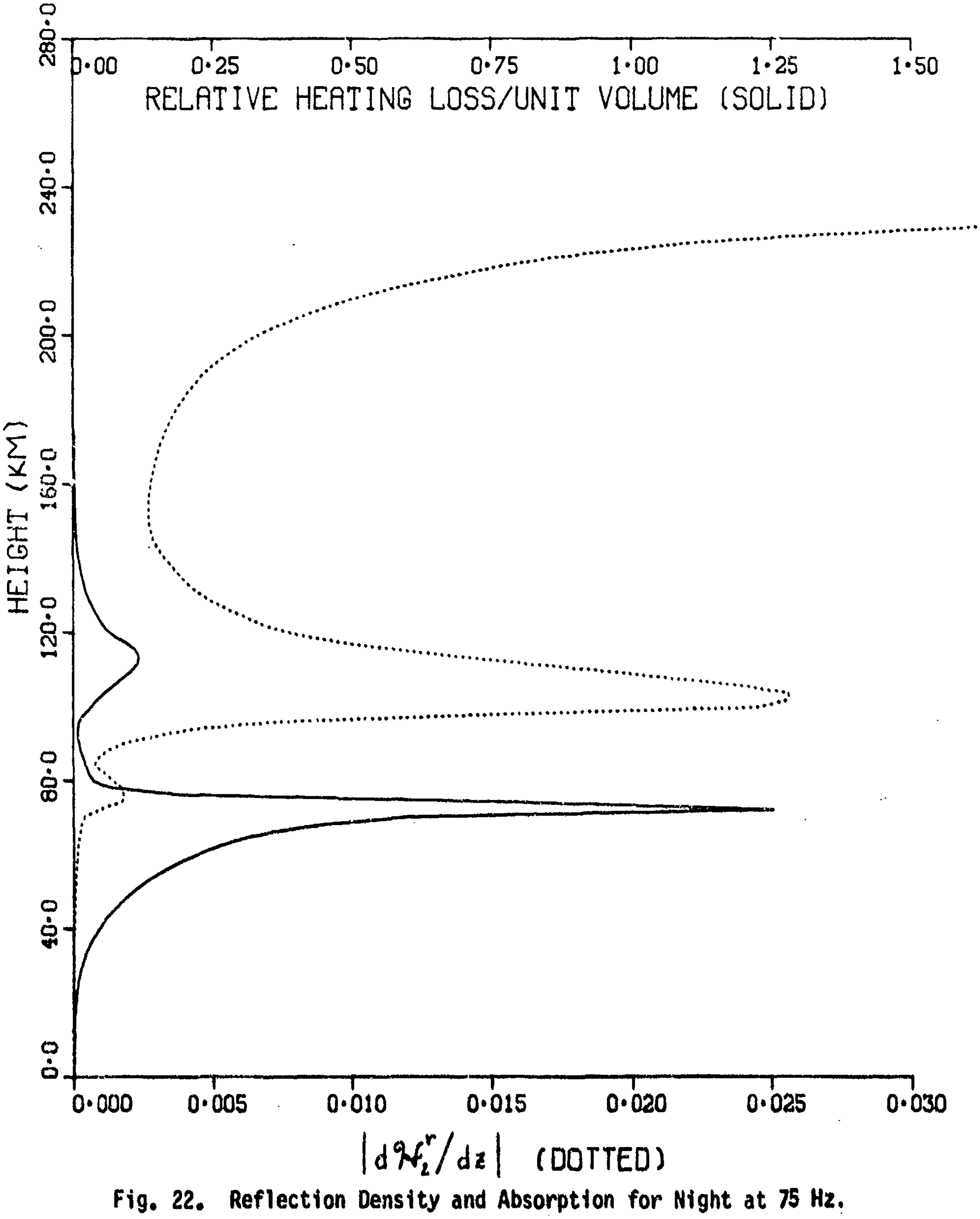

Fig. 22. Reflection Density and Absorption for Night at 75 Hz. Azimuth = 270°, Dip = 60°, Geomagnetic Field = 0.5 Gauss.

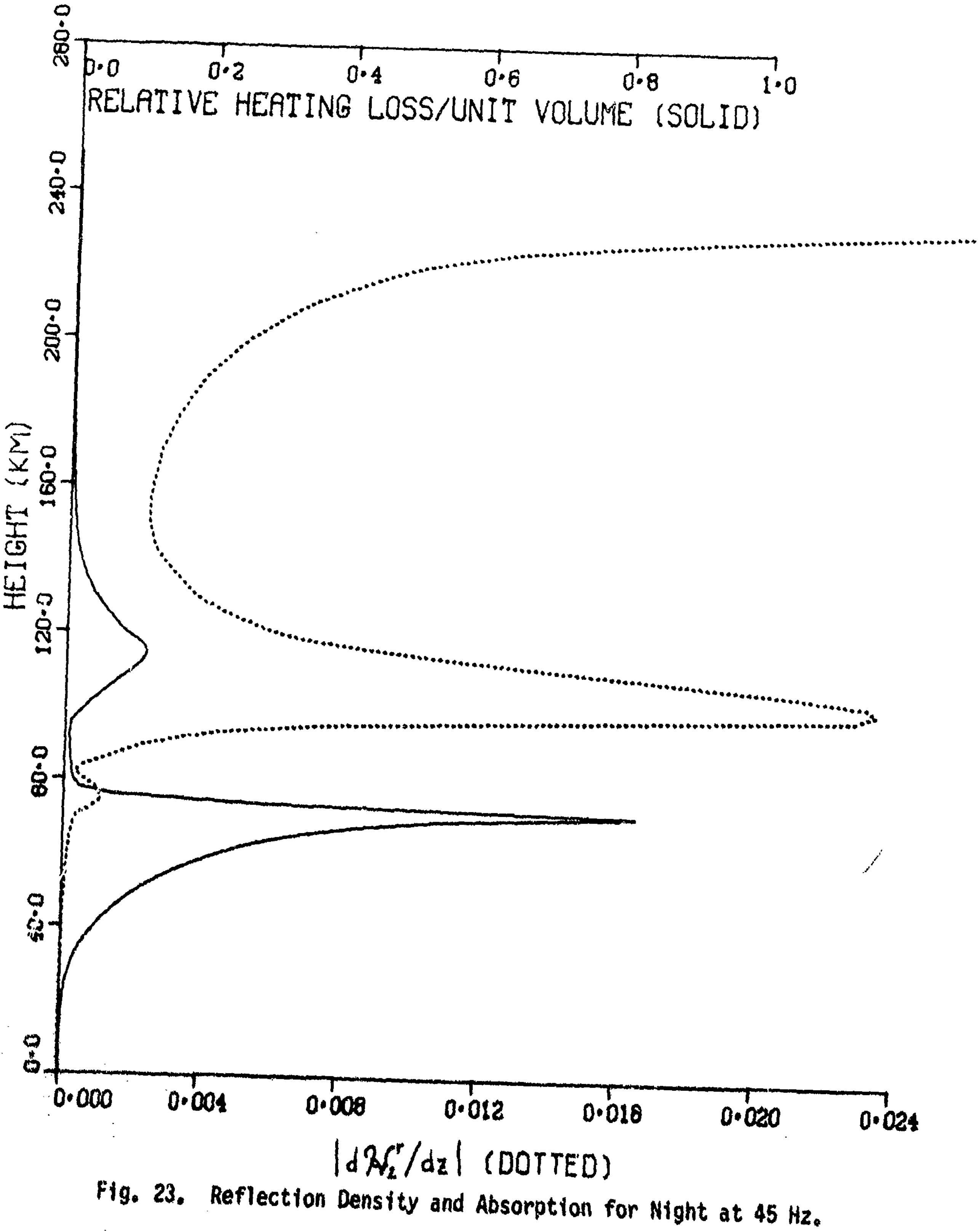

Fig. 23. Reflection Density and Absorption for Night at 45 Hz. Azimuth = 270°, Dip = 60°, Geomagnetic Field = 0.5 Gauss.

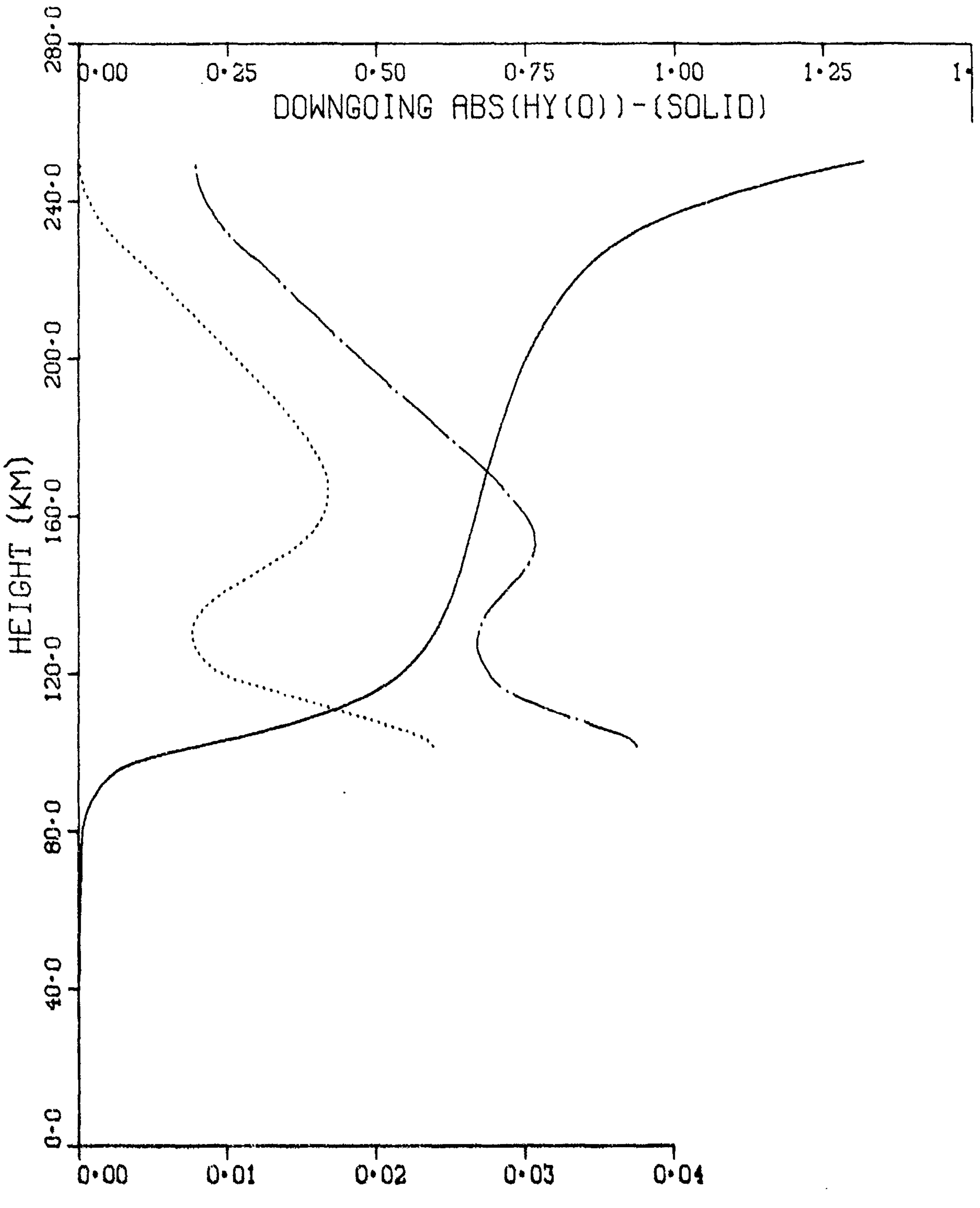

Fig. 24. Reflection Properties Poynting Flux for Night at 7.5 Hz.

Azimuth = 270°, Dip = 60°, Geomagnetic Field = 0.5 Gauss.

integrated effect of the dipole layer structure below the height indicated on the vertical axis. Because the modal height gain at the starting height of 250 km is in this instance composed of two outgoing magnetoionic components, it is not convenient to present field results as for the 75 and 45 Hz cases in terms of departures from the outgoing whistler mode. Rather, we present in Figure (24) for altitudes above 100 km the upgoing and downgoing Poynting flux as defined by Eqs. (11). These curves show that the upgoing and downgoing fluxes are of the same order of magnitude throughout much of this height range, thereby indicating that the final values depend in some measure on reflections occurring at the uppermost altitudes. The solid curve solidifies this conclusion in the following sense. The solid curve achieves the value of 0.5 at an altitude of about 115 km, however the phase of the y component of the reflected $\mathcal{H}$ field at the ground departs from its final value of 0.0^{0} by about 113^{0}. We conclude then that the integrated re-radiation above this level is significant. Apparently because of interference between reflections from disparate ionospheric regions of the ionosphere (see e.g., the steep gradients in the solid curve of Figure (24) around 110 and 240 km) the normal mode polarization is not TM but has in fact a substantial TE admixture. A measure of this mixing is the magnitude of the ratio of $\mathcal{H}_1/\mathcal{H}_2$ at the ground. This value in the present instance is about 1.3.

To understand how interference from ionospheric reflecting layers can lead to polarization mixing we will turn now to a discussion of the ambient nighttime profile of Figure (1) with the superimposed sporadic E layer. Recall that this is a layer around 120 km, about 5 km thick at the top and about 15 km thick at the base with a peak electron density enhancement factor of about 30 over that of the nighttime ambient. Figure (25) shows the attenuation versus frequency for both the nighttime ambient and for the nighttime ambient with the superimposed sporadic E. As will be seen, there exists a strong resonance which at its peak represents about an order of magnitude enchancement over the ambient attenuation. Also it will be seen that the attenuation peaks at about 78 Hz. Figure (26) shows the relative heating loss per unit volume and its integrated effect in attenuation units for this case at 75 Hz. The curve shows the low altitude absorption at about 72 km, a much amplified (over the nighttime ambient profile alone - see Figure (11)) high altitude absorption at about 105 km and an absorption associated with the sporadic E layer. The low altitude absorption contributes less than 1 dB/1000 km to the attenuation. The high altitude absorption contributes about 4 dB/1000 km and the sporadic E layer itself contributes about 2.5 dB/1000 km. The remainder of about 2.5 dB/1000 km can be attributed to leakage beyond the sporadic E layer.

Figure (27) shows again the relative heating loss but along with the magnitude of the reflected $\mathcal{H}_2$ field density defined by Eq. (18) of section 3. The increase in the latter curve in the neighborhood of 240 km is discounted because the rf field above the sporadic E layer is principally in the outgoing whistler mode (See Figure (28) where the quantities $|\mathcal{H}_2-i\mathcal{H}_1^u|$ and $|E_2-iE_1^u|$ have been plotted). Thus Figure (27) shows a reflection region centered about 100 km and another centered at the sporadic E layer. To better understand the origin of the resonance behavior of Figure (25), the preceding two layer reflection behavior

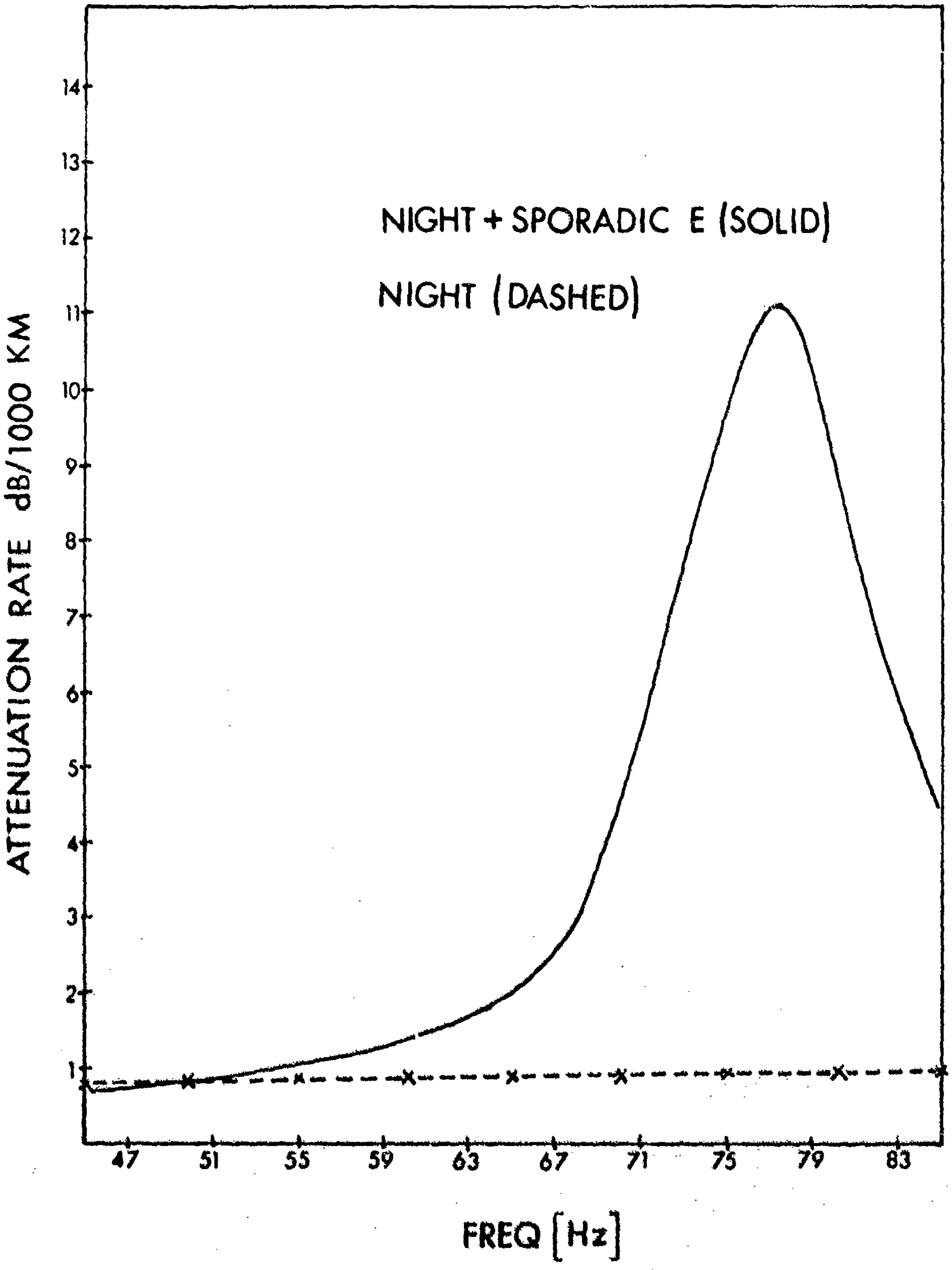

Fig. 25. Attenuation Versus Frequency for Night Ambient and for Night Ambient + Sporadic E. Azimuth = 105°, Dip = 77°, Geomagnetic Field = 0.41 Gauss.

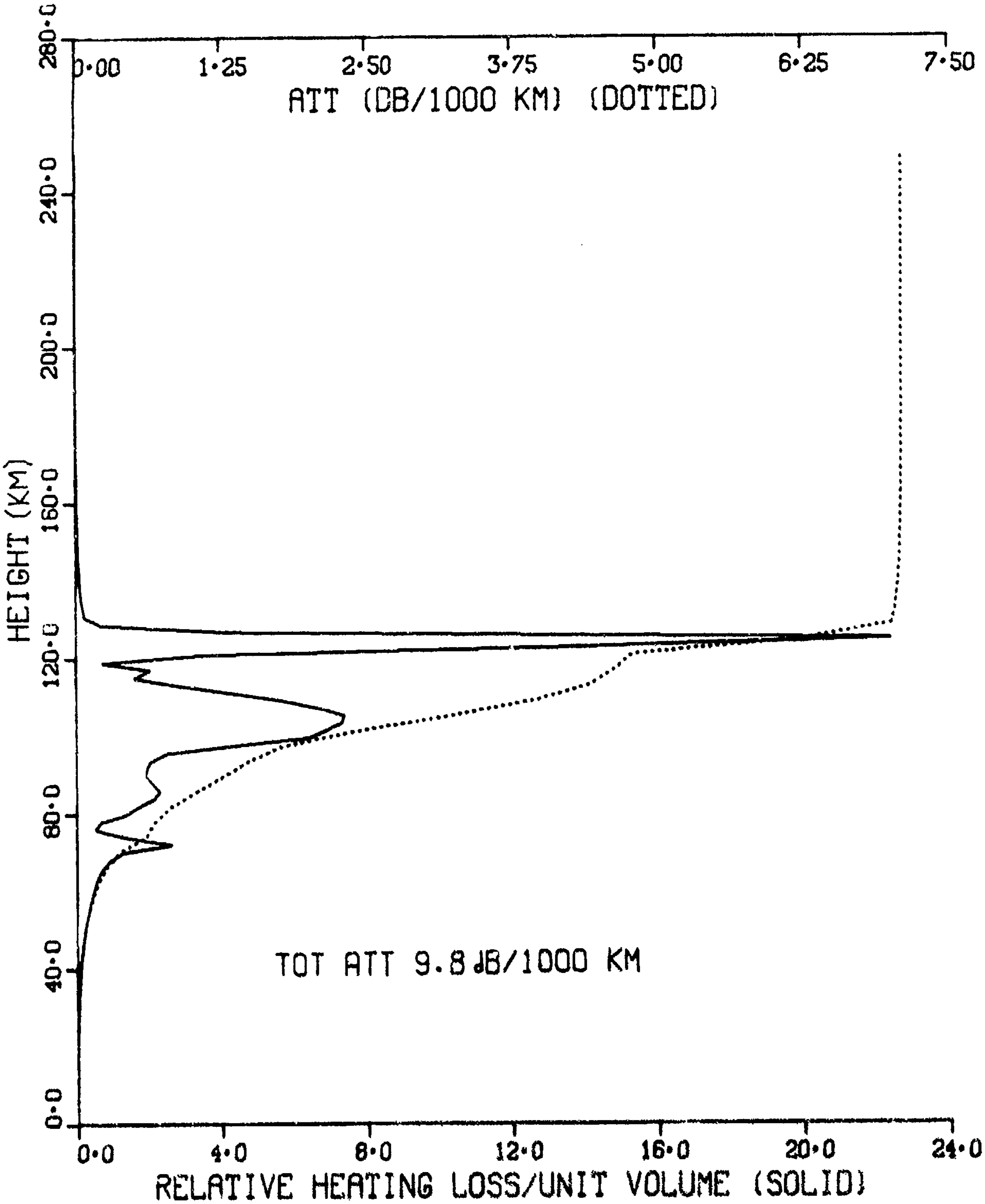

Fig. 26. Absorption and Attenuation for Night Ambient + Sporadic E at 75 Hz. Azimuth = 105°, Dip = 77°, Geomagnetic Field = 0.41 Gauss.

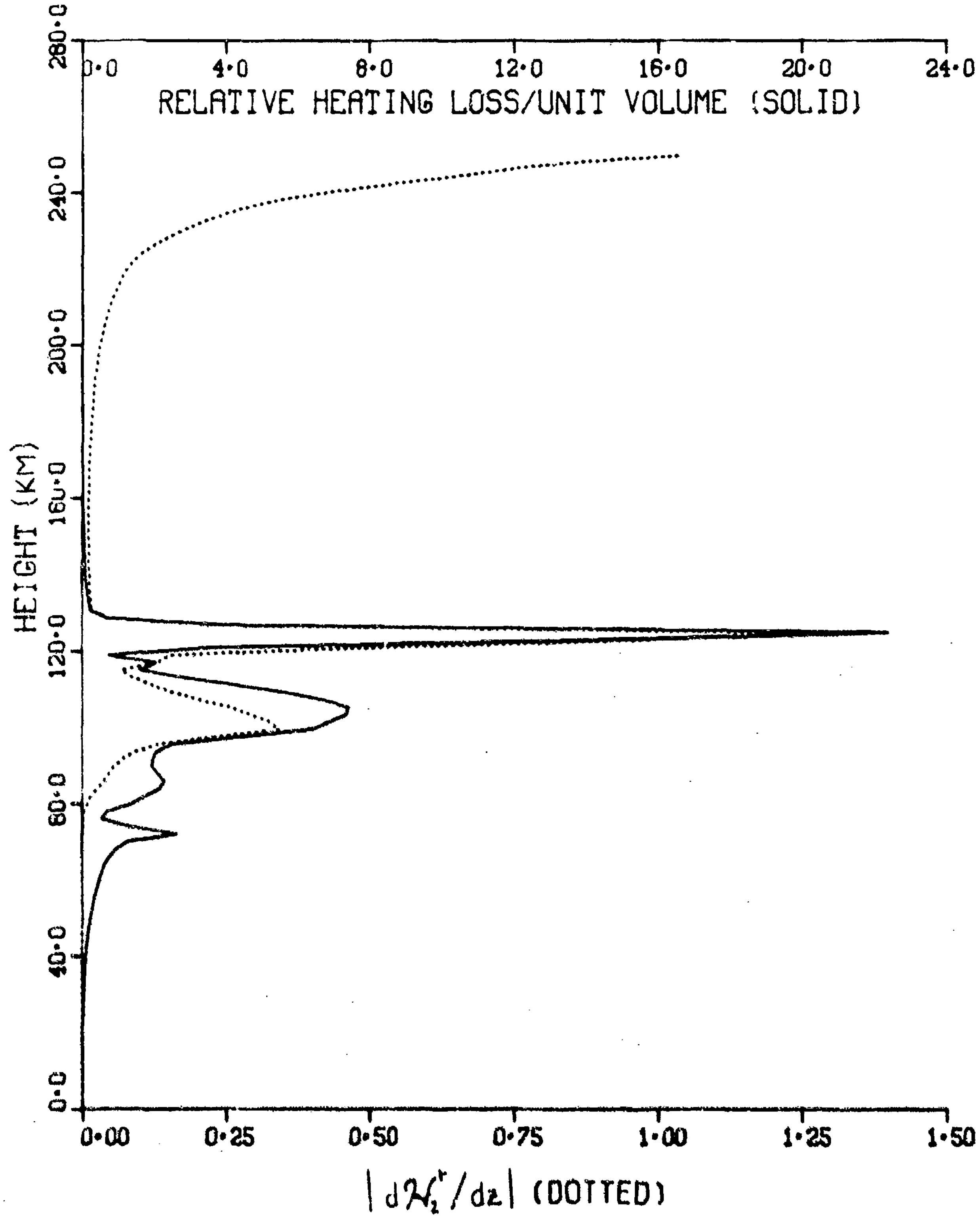

Fig. 27. Reflection Density and Absorption for Night Ambient + Sporadic E at 75 Hz. Azimuth = 105°, Dip = 77°, Geomagnetic Field = 0.41 Gauss.

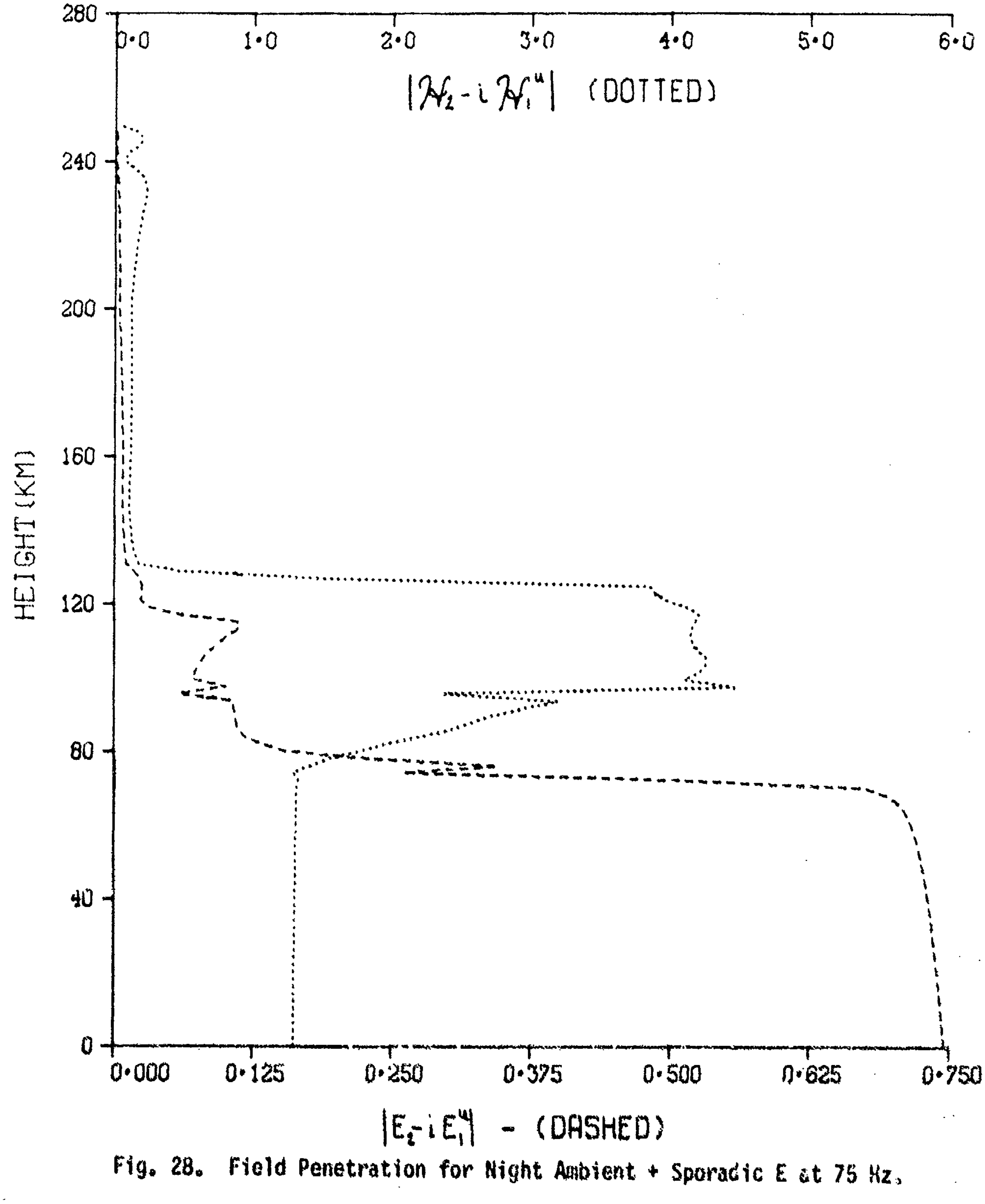

Fig. 28. Field Penetration for Night Ambient + Sporadic E at 75 Hz. Azimuth = 105°, Dip = 77°, Geomagnetic Field = 0.41 Gauss.

suggests the simplified model shown in Figure (29). It consists of vacuum below level 2, equal and homogeneous electron and ion densities N_2, N_3 and N_4 in regions 2, 3, and 4 respectively. The electron and ion collision frequencies are also assumed constant in the different regions. The model also assumes that quasi longitudinal propagation applies in the altitude region above z. The analysis for this model is given in Appendix C. For parameters like those appropriate to Figure (27), the results of Appendix C suggest that a primary condition for an accentuated resonance is that the region between the two reflecting levels (i.e., between z_1 and z_2 in Figure (29)) behave like a quarter wave plate and that simultaneously the sporadic E layer also have a thickness equal to one quarter integer multiples of the local wavelength, thereby reducing leakage through the layer. The resonance is shifted in frequency and considerably diminished if the thickness of the sporadic E layer is half integer multiples of the local wavelength, a condition conducive to leakage out of the top of the layer. Location and strength of the resonance varies between the above limits as the thickness of the sporadic E layer changes from quarter wave length behavior to half wave length behavior. These features are illustrated in Figure (30) which shows attenuation versus frequency for the following parameters of Figure (29) (subscripts e and i stand for electrons and ions respectively):

$$N_2 = N_4 = 2 \times 10^3/\text{cm}^3 \text{ , } N_3 = 6 \times 10^4/\text{cm}^3$$

$$\nu_{e2} = \nu_{e3} = \nu_{e4} = 10^4 \text{ sec}^{-1}$$

$$\nu_{i2} = \nu_{i3} = \nu_{i4} = 3 \times 10^2 \text{ sec}^{-1}$$

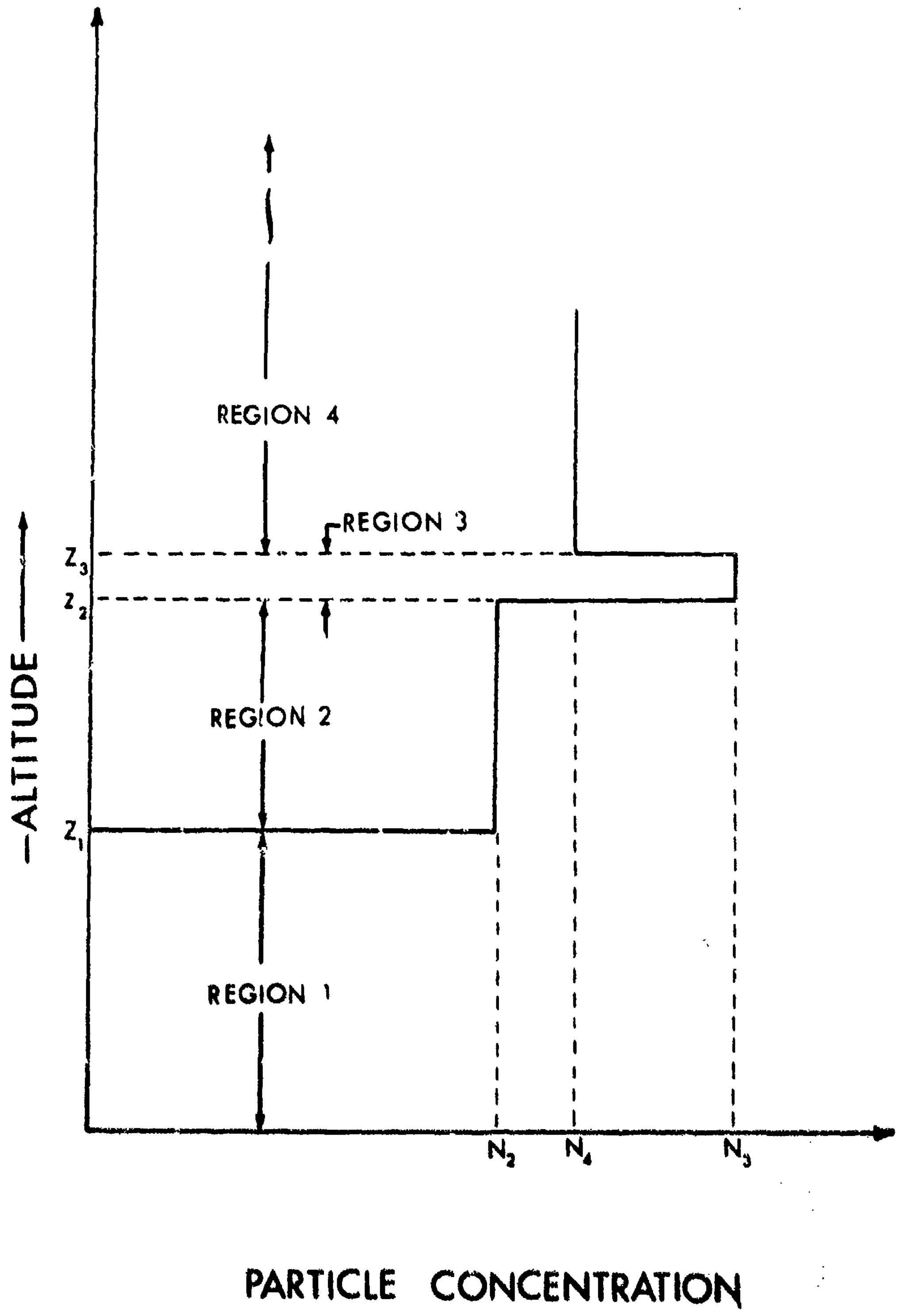

Fig. 29. Simplified Ionosphere and Sporadic E Model.

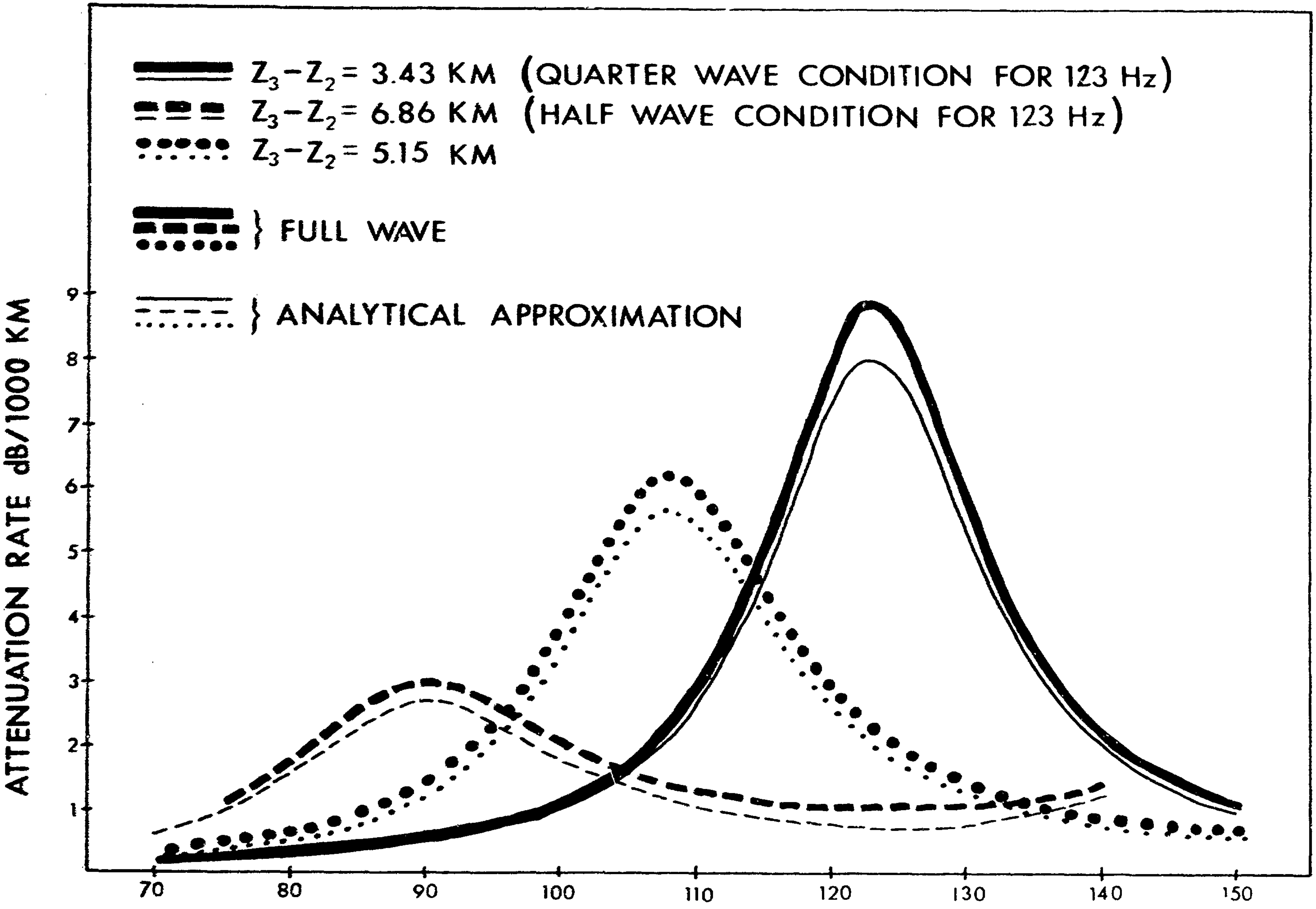

Fig. 30. Attenuation Versus Frequency for Simplified Model. Azimuth = 105°, Dip = 77°, Geomagnetic Field = 0.41 Gauss.

$z_2 - z_1$ = 20 km Quarter wavelength condition at 123 Hz

$z_3 - z_2$ = 3.43 km Quarter wavelength condition at 123 Hz

$z_3 - z_2$ = 5.71 km

$z_3 - z_2$ = 6.86 km Half wavelength condition at 123 Hz

The heavy curves in Figure (30) are full wave output and the light curves are model results calculated using Eqs. C.10, C.23 and C.25 of Appendix C. It will be seen that the full wave results and the simplified model results are in excellent agreement. It will further be noted that the resonance is shifted and diminished, as stated above, when region 3 has a thickness equal to one half of the local wavelength. Figure (31) shows the relative heating loss per unit volume and its integrated effect in attenuation units at 123 Hz for the case when region 3 behaves like a quarter wave plate. The absorption below 120 km contributes close to 5 dB/1000 km to the attenuation and region 3 contributes by virtue of absorption about 1 dB/100 km. The remainder of about 3 dB/1000 km can be attributed to leakage into region 4. These numbers are similar to those quoted in connection with Figure (26) and in fact, not surprisingly, a striking similarity will be noted between Figures (26) and (31). Figure (32) shows the relative heating loss per unit volume and its integrated effect in attenuation units at 90 Hz for the case when the thickness of region 3 is one half of the local wavelength. In this case the reflection by the sporadic E layer into the earth-ionosphere waveguide is much reduced from the previous case so that the field buildup and the attenuation in the 100 to 120 km range is very much reduced from the previous case.

Under the condition of strong attenuation resonance, there is appreciable TE admixture in the normal mode. A measure of this is given by the ratio of $\mathcal{H}_1/\mathcal{H}_2$ at the ground. This ratio is for the conditions appropriate to Figure (31).

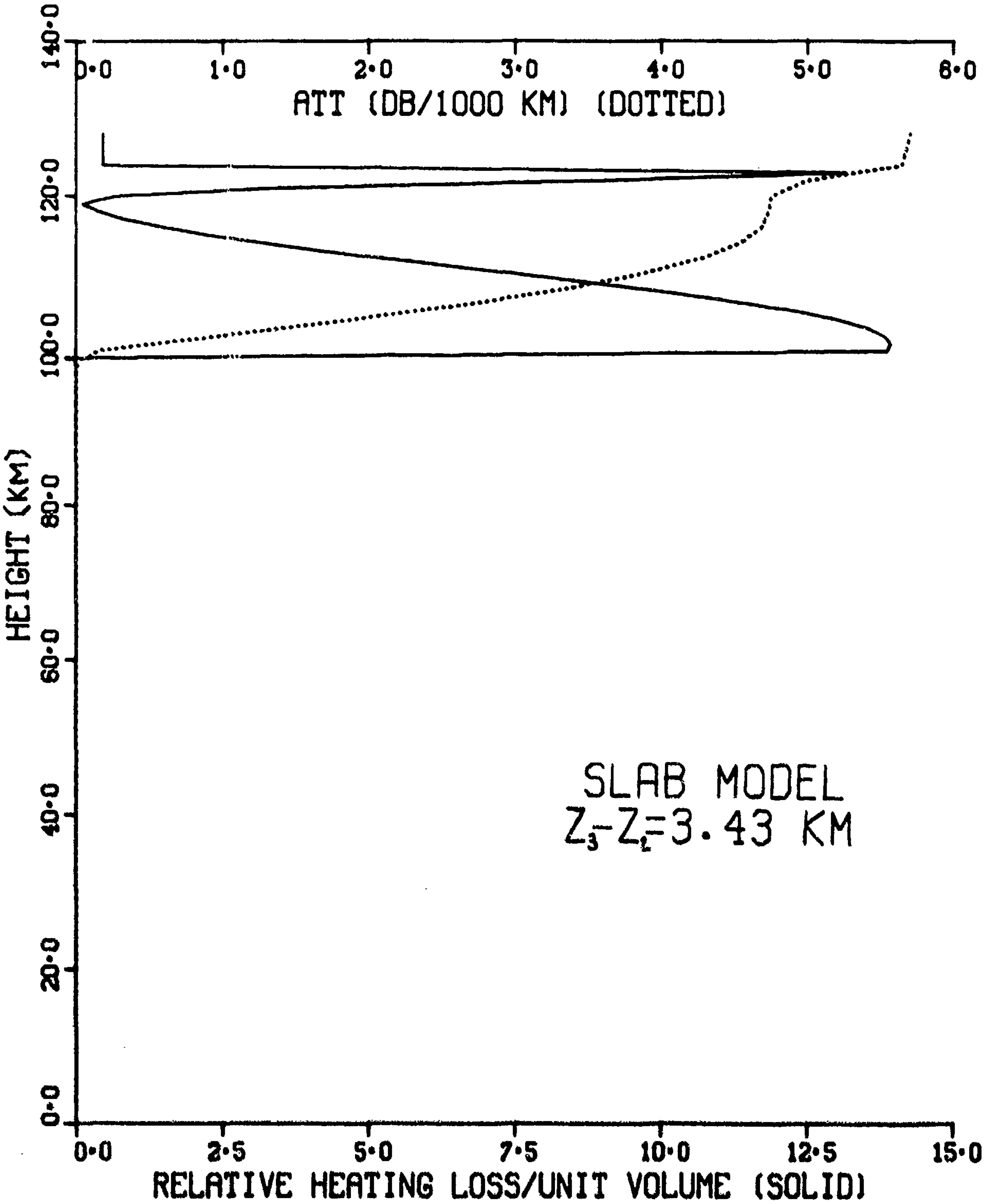

Fig. 31. Simplified Model Absorption and Attenuation for Quarter Wave Behavior at 123 Hz. Azimuth = 105°, Dip = 77°, Geomagnetic Field = 0.41 Gauss.

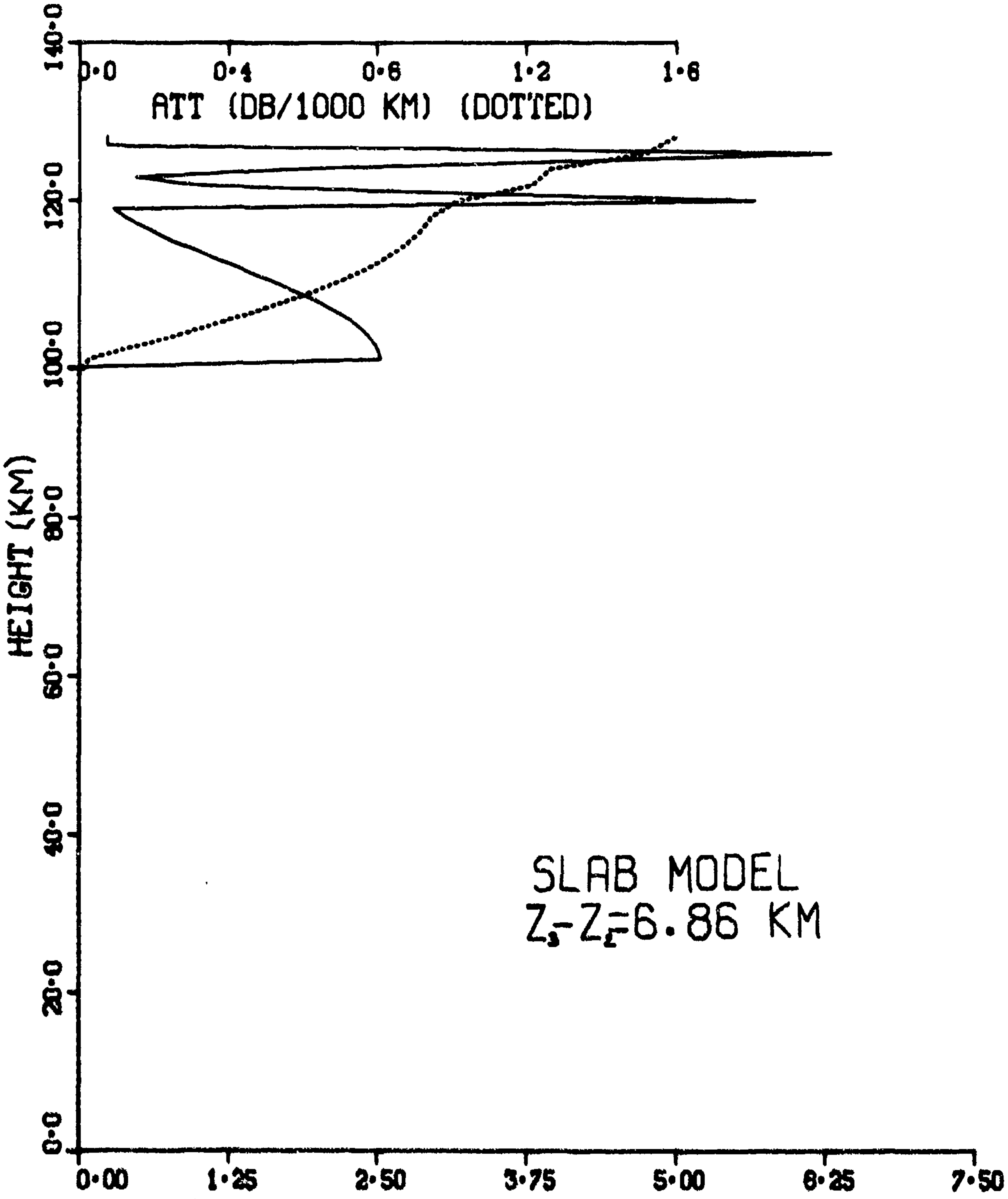

Fig. 32. Simplified Model Absorption and Attenuation for Half Wave Behavior at 90 Hz. Azimuth = 105°, Dip = 77°, Geomagnetic Field = 0.41 Gauss.

$\mathcal{H}_1/\mathcal{H}_2 = 0.747\underline{/-15.7}^\circ$ from full wave calculation

$\mathcal{H}_1/\mathcal{H}_2 = 0.723\underline{/-12.5}^\circ$ from C.23 and C.38

Although the profiles of Figure 1 yield modal parameters which agree quite well with available data in the Seafarer band, they do seem to yield an unreasonably high attenuation rate in the range of the fundamental Schumann frequency. This is because of excessive leakage above the E layer. Booker and Lefeuvre,[23] for this reason, have suggested that profiles with stronger E region ledges may be more reasonable and one might legitimately ask if the resonance behavior shown in Figure 25 would then be wiped out. Comparison of such a profile (referred to as the B-L profile) with the nighttime profile of Figure 1 is shown in Figure (33). The much stronger E region ledge of the B-L profile is evident. Figure 34 shows attenuation rate versus frequency for the nighttime ambient profile with the sporadic E layer superimposed along with the results for the B-L profile with the sporadic E layer and still another curve showing results for the B-L profile with the sporadic E layer lowered by 10 km (i.e., the layer is at about 110 km rather than 120 km). It will be seen that the resonance is most pronounced for the night ambient profile with the superimposed sporadic E layer. The reason for this is, as just discussed, that the quarter wavelength conditions are satisfied. The resonance is diminished and shifted out of the Seafarer band for the case of the sporadic E layer at 120 km superimposed on the B-L profile but is again shifted into the Seafarer band if the sporadic E layer is lowered 10 km and superimposed on the B-L profile. The significance of these results is of course the degree of sensitivity to the ledge ionizations. This is further evidenced by Figure 35 which again shows attenuation rate versus frequency. In this case the sporadic E layer has been modeled as

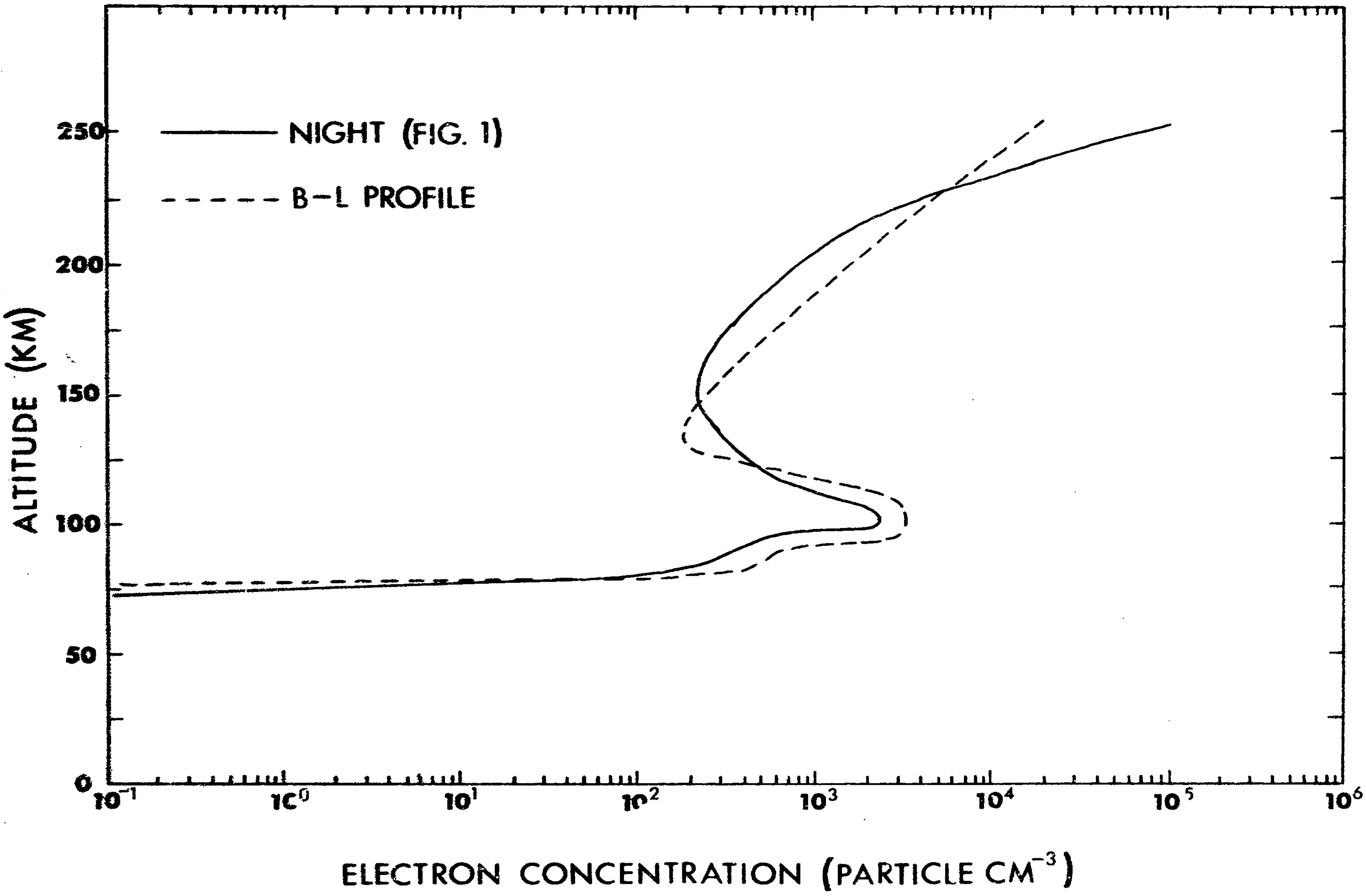

Fig. 33. Night Ambient of Fig. 1 and B-L Profiles.

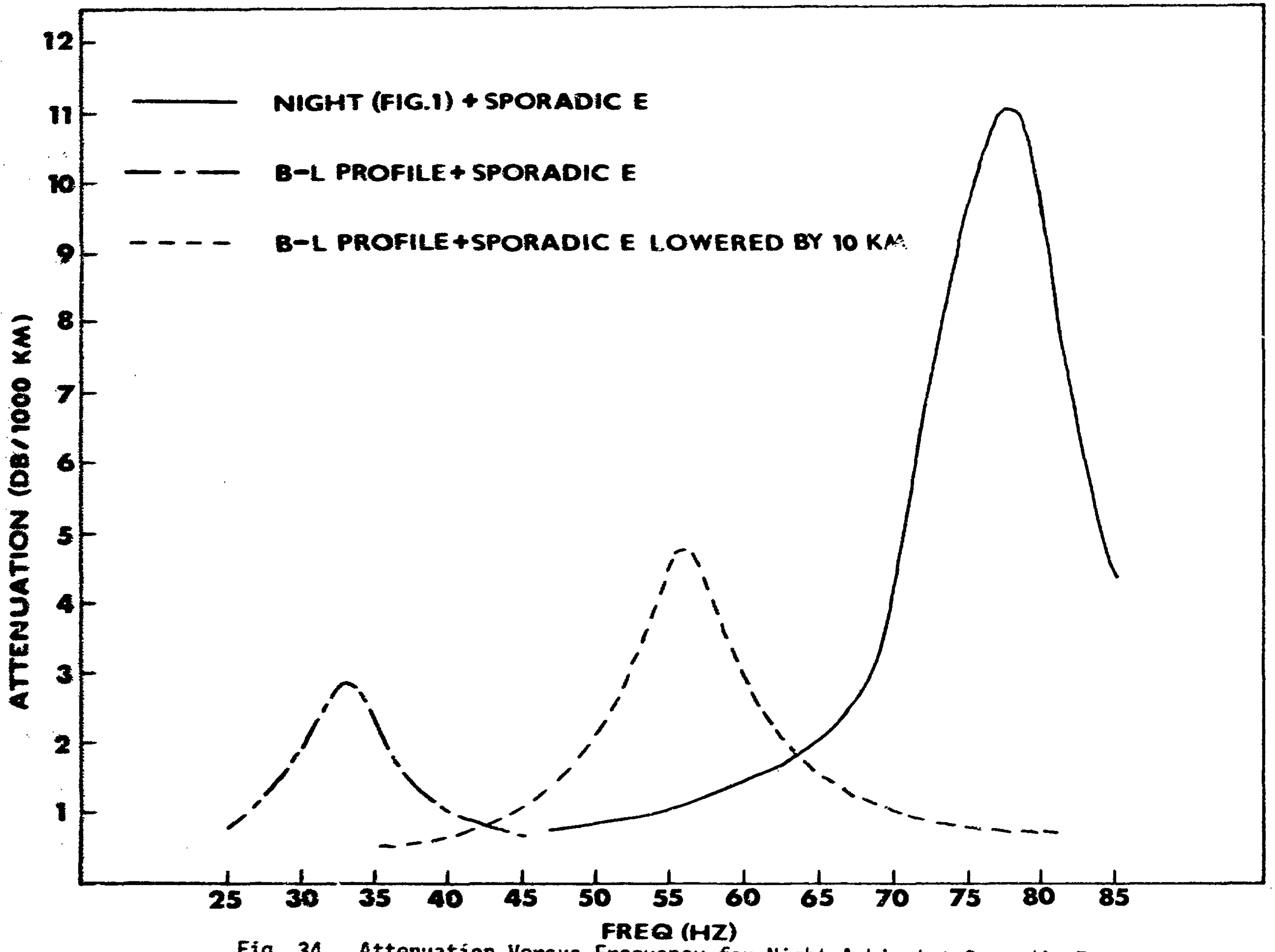

Fig. 34. Attenuation Versus Frequency for Night Ambient + Sporadic E and B-L + Sporadic E. Azimuth = 105°, Dip = 77°, Geomagnetic Field = 0.41 Gauss.

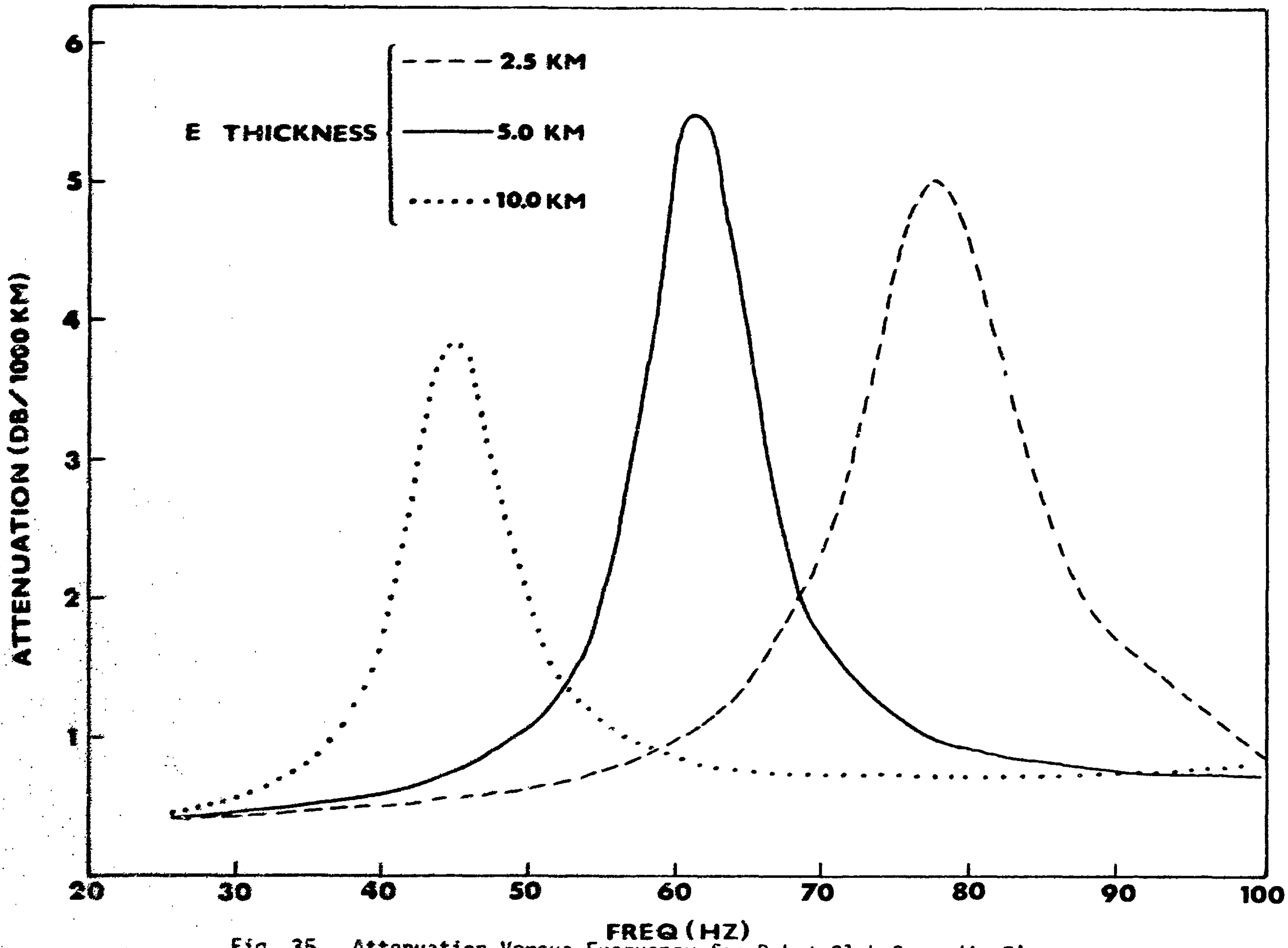

Fig. 35. Attenuation Versus Frequency for B-L + Slab Sporadic E's Starting at 110 km. Azimuth = 105°, Dip = 77°, Geomagnetic Field = 0.41 Gauss.

a sharply bounded homogeneous slab starting at 110 km and having thickness of 2.5, 5.0, and 10.0 km. Again the effect is significant in the Seafarer band and as expected from the previous discussion of the simplified model of Figure 29 shows marked sensitivity to the modeled sporadic E layer thickness.

We now turn to a discussion of reflection properties associated with the daytime profile of Figure 1. In particular Figures 36 through 38 show results relevant to the re-radiation theory as discussed in section 3. The figures apply to the same geomagnetic conditions as Figures 2 through 4 and more particularly Figure 36 is for 75 Hz, Figure 37 for 45 Hz and Figure 38 for 7.5 Hz. The upper horizontal scale applies to the solid curve (Eq. (17) of section 3) and to the dotted curve (Eq. (13) of section 3). The lower horizontal scale applies to the dashed curve (Eq. (14) of section 3). The solid curve represents the buildup of the magnitude of the reflected y component of the $\mathcal{H}$ field at the ground due to the integrated effect of the dipole layer structure below the height indicated on the vertical axis. Because of the normalization used the value of the magnitude of $\mathcal{H}_2^r$ associated with the re-radiation from the total ionosphere is 0.5. The dotted curve is the magnitude of $\mathcal{H}_2 - i\mathcal{H}_1^u$ and the dashed curve is the magnitude of $E_2 - iE_1^u$ where the field components are either full wave components or decompositions thereof as discussed in section 3.

The solid curve of Fig. 36 illustrates, then, that the buildup of the magnitude of the y component of the reflected field at the ground begins slowly around 55 km and achieves its final value in magnitude of 0.5 at about 90 km. Since the total field above about 95 km is almost totally in the outgoing whistler mode, the large amplitude oscillations

Field = 0.41 Gauss.

Fig. 36. Reflection and Field Penetration Properties for Day at 75 Hz.

Azimuth = 270°, Dip = 60°, Geomagnetic Field = 0.5 Gauss.

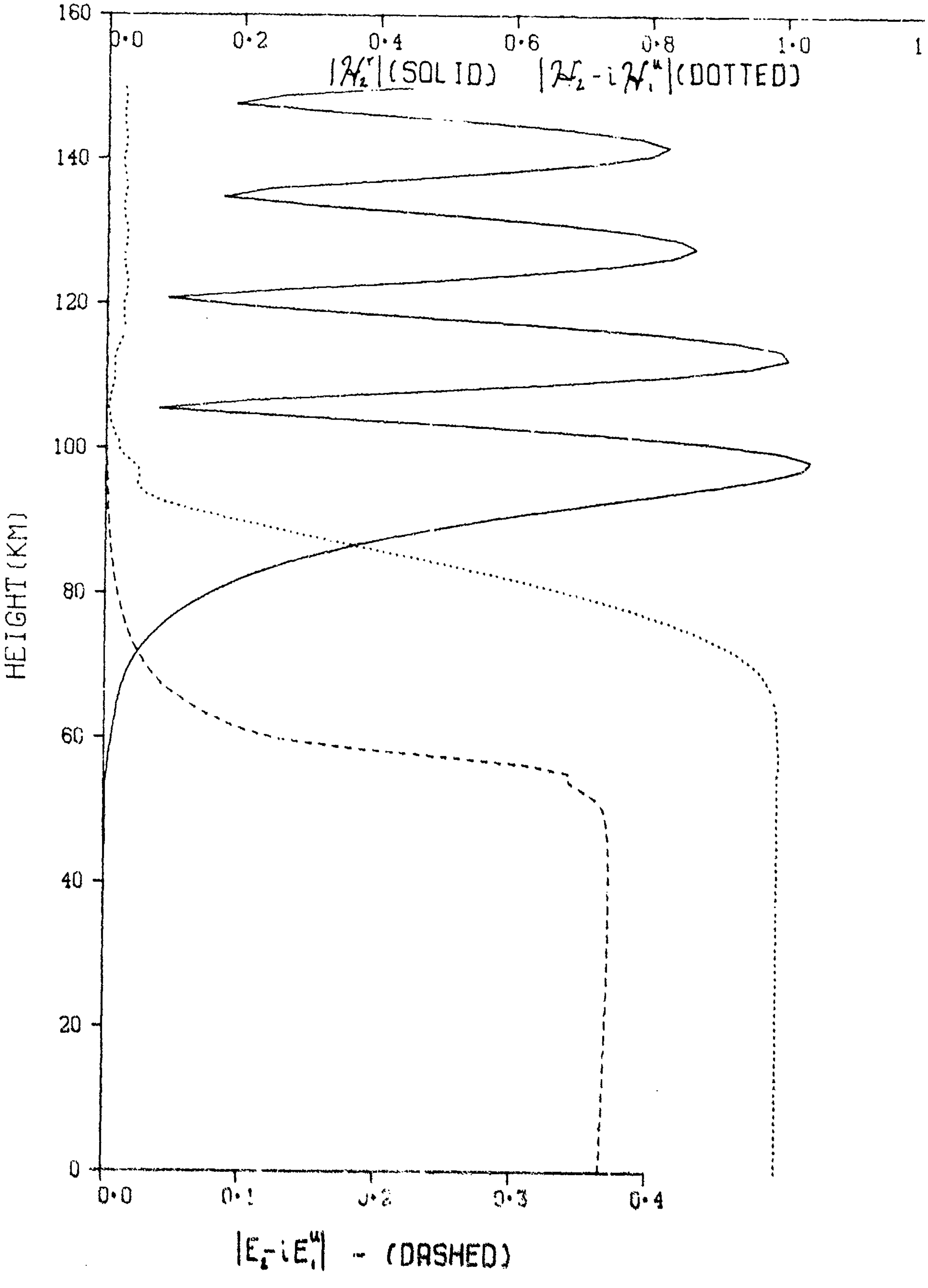

Fig. 37. Reflection and Field Penetration Properties for Day at 45 Hz.

Azimuth = 270°, Dip = 60°, Geomagnetic Field = 0.5 Gauss.

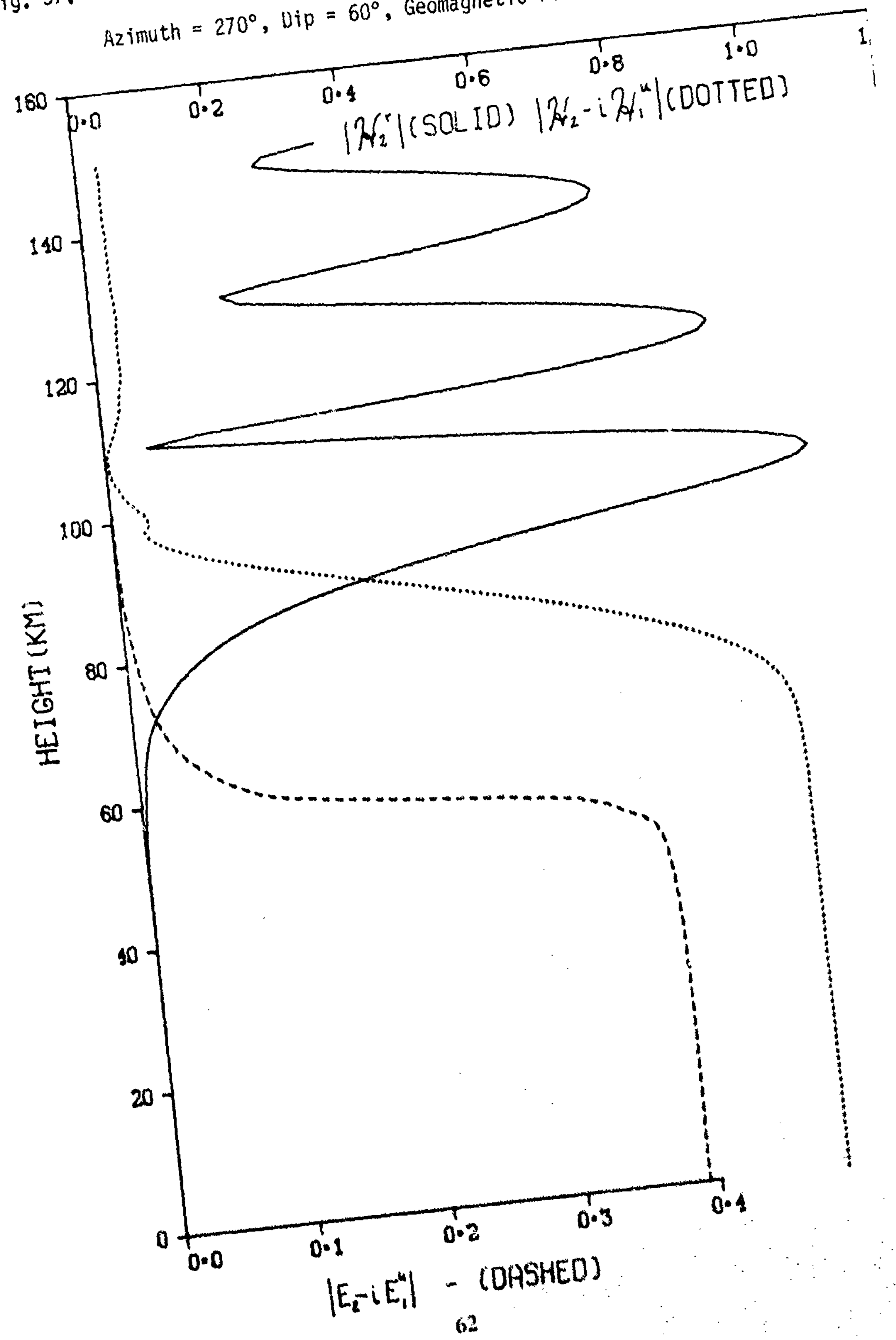

Fig. 38. Reflection and Field Penetration Properties for Day at 7.5 Hz.

Azimuth = 270°, Dip = 60°, Geomagnetic Field = 0.5 Gauss.

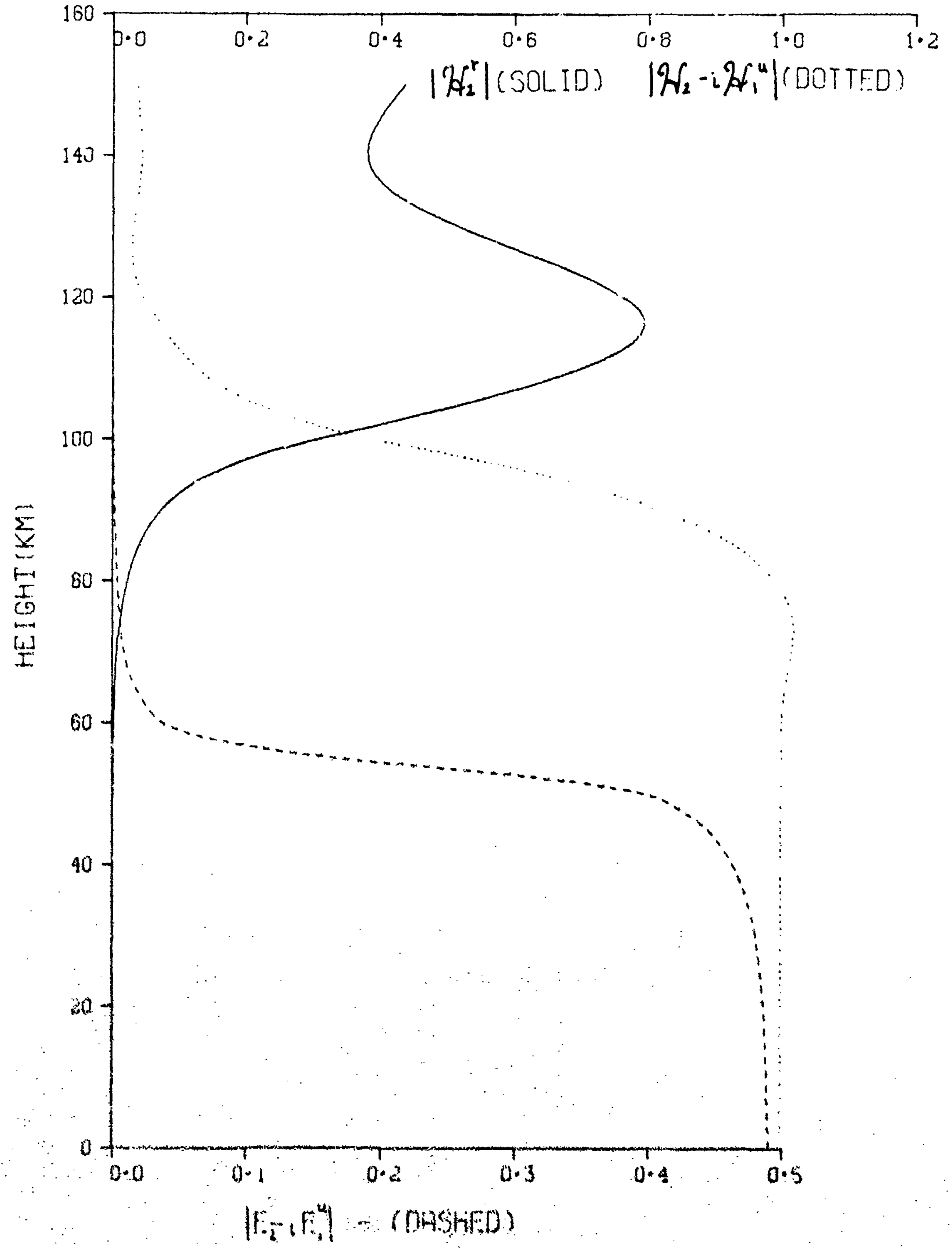

in the solid curve above this height are due almost exclusively to the outgoing whistler mode leakage and the resulting large polarization associated with the daytime ionosphere. On the basis of the combined information conveyed by the solid, dotted and dashed curves of Fig. 36, the conclusion is that the reflection is in large measure accomplished by the dipole structure below the 95 km level. Figure 37 illustrates the same features as those just discussed in connection with Fig. 36. Figure 38 shows the considerably deeper field penetration which occurs for 7.5 Hz. In this case the reflection appears to be determined principally by the dipole structure below about 120 km. Figures 36 through 38 all indicate a reflection behavior similar to that associated with incidence on a pure dielectric and the fact that Figs. 36 through 38 do not indicate clearcut reflecting levels result from this behavior. The penetration depths of 95 km and 120 km quoted above can best be likened to the notion of a skin depth although the ionosphere is behaving in some respects more like a dielectric reflector rather than a metallic reflector.

There are circumstances when the ionosphere behaves like a metallic reflector. Absorption properties for these special cases, especially as regards the influence of low level ions, has been discussed rather extensively by Field.[26] One of the special cases is when propagation in the ionosphere can be approximated by quasi transverse propagation. This requires, as discussed by Booker and Lefuvre,[23] propagation in a narrow angular sector about the magnetic equator and Figs. 39 through 41 show what can be expected under those circumstances. The figures apply to the daytime profile under geomagnetic conditions of east to west propagation at the magnetic equator. The upper scale applies to the solid curve and

Fig. 39. Reflection Density and Absorption for Day at the Magnetic Equator at 75 Hz. Azimuth = 270°, Dip = 0°, Geomagnetic Field = 0.5 Gauss.

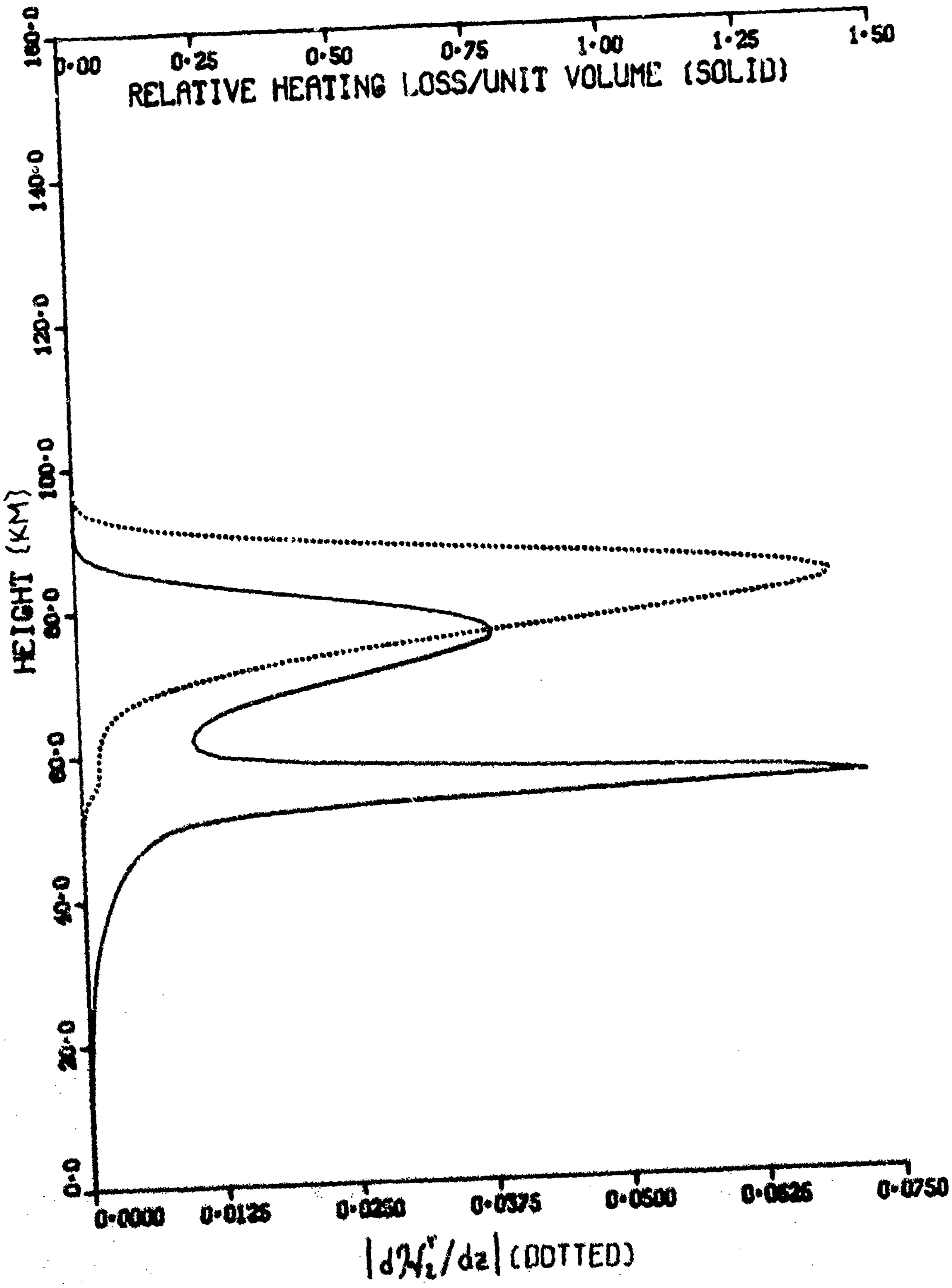

Fig. 40. Reflection Density and Absorption for Day at the Magnetic Equator at 45 Hz. Azimuth = 270°, Dip = 0°, Geomagnetic Field = 0.5 Gauss.

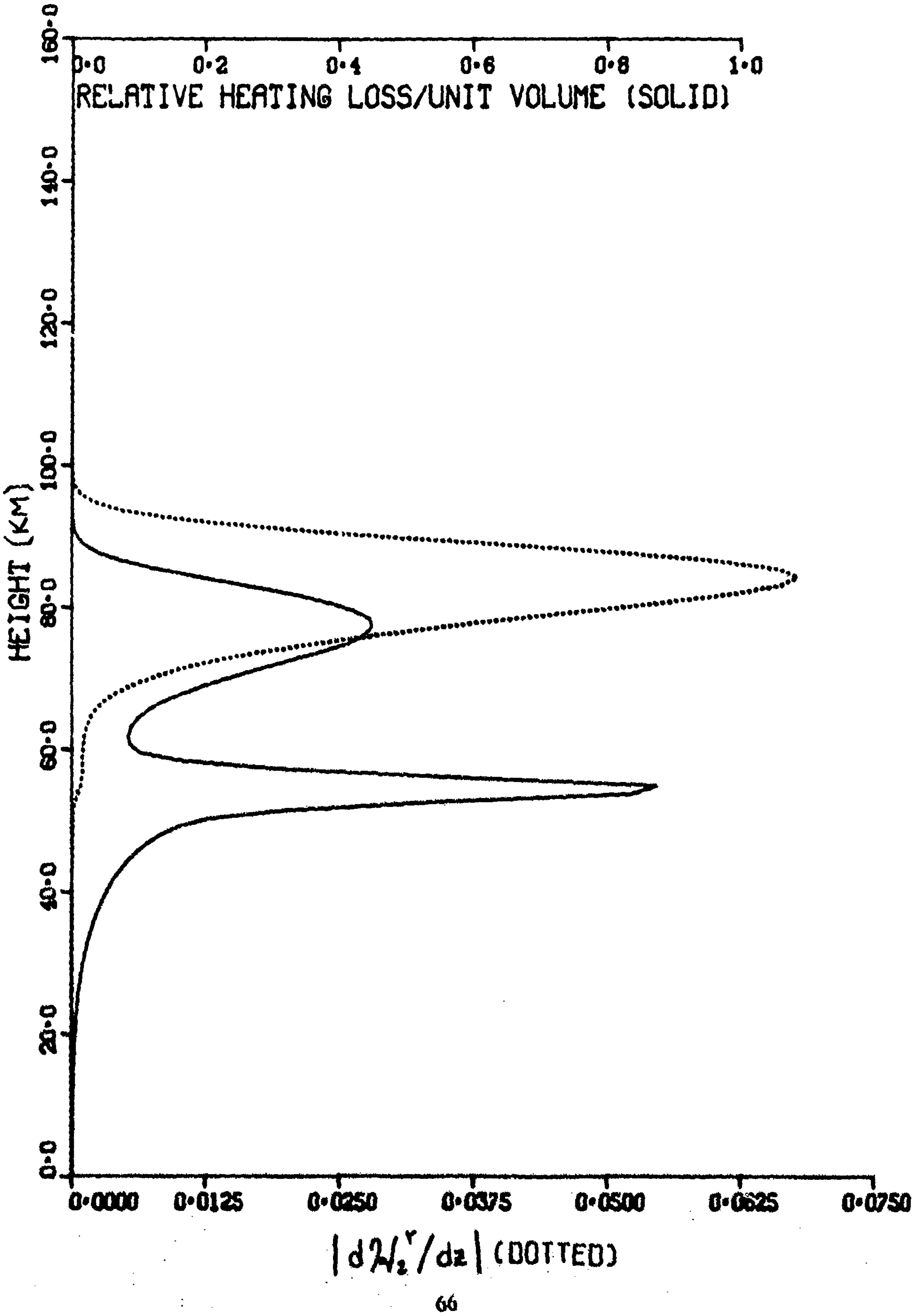

Fig. 41. Reflection Density and Absorption for Day at the Magnetic Equator at 7.5 Hz. Azimuth = 270°, Dip = 0°, Geomagnetic Field = 0.5 Gauss.

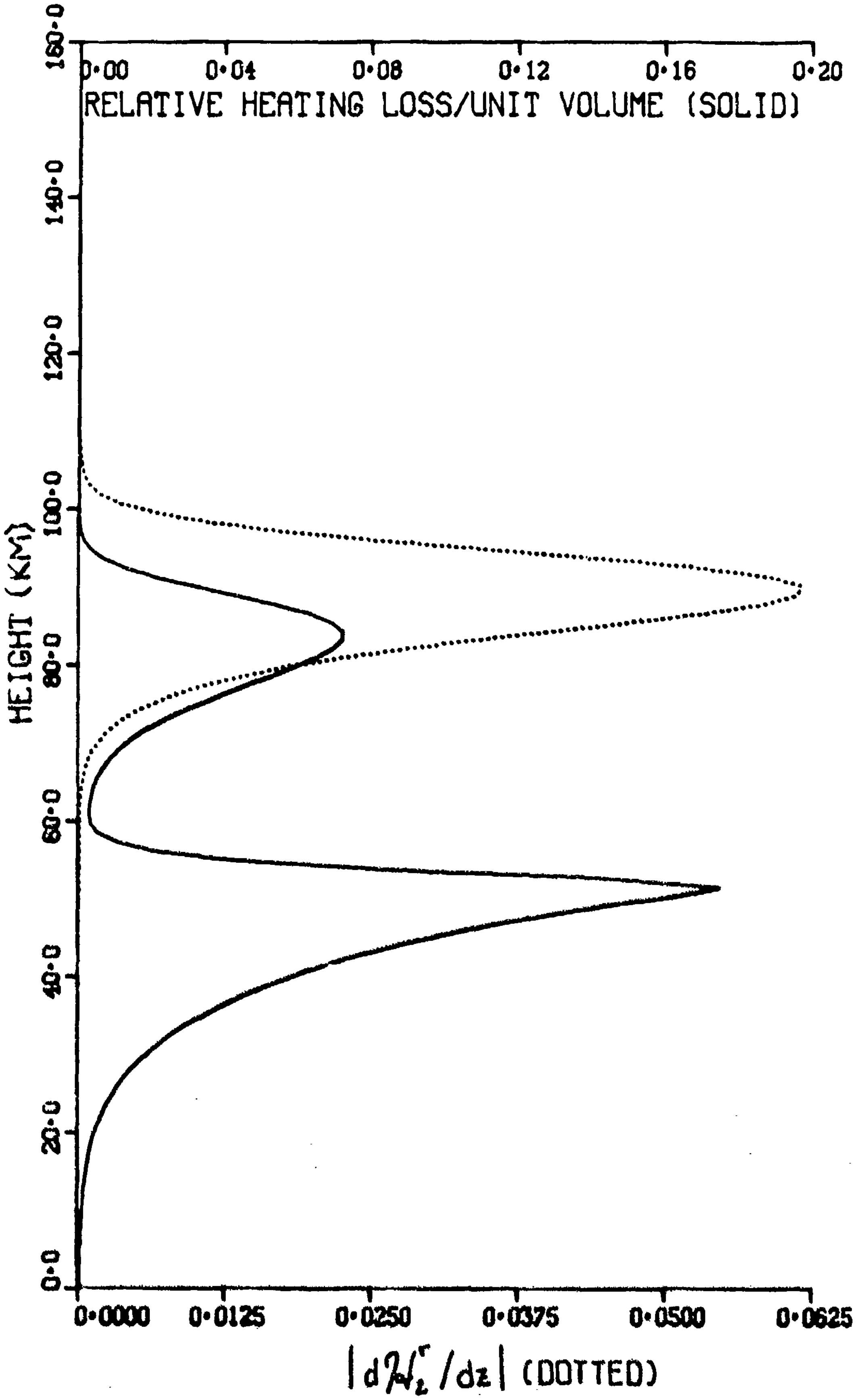

the lower scale applies to the dotted curve. The solid curve is the relative heating loss per unit volume and the dotted curve is the magnitude of the $\mathcal{H}_2$ reflected field density ($d\mathcal{H}_2^r/dz$) and shows in these instances well defined reflection levels in the neighborhood of 84 km for the 75 and 45 Hz cases and in the neighborhood of 90 km for the 7.5 Hz case. The integrated buildup of the magnitude of the y component of the reflected $\mathcal{H}_2$ field at the ground due to the dipole structure beneath the ordinate value (Eq. (17) of section 3) for these cases is shown in Figs. 42 through 44. The leveling off of the curve at a value of 0.5 should be compared with the oscillating behavior shown in Figs. 36 through 38.

When the ionosphere is highly depressed it again acts like a metallic reflector. This is illustrated in Figs. 46 through 48. These figures are for the hypothetically depressed ionosphere shown in Fig. 45. The curves show the same information and have the same scale legends as Figs. 39 through 41. They show clearcut reflection levels at about 65 km for the 75 and 45 Hz cases and a considerably broader reflection stratum centered about 70 km for the 7.5 Hz case. Note also that in these cases there are two relatively low altitude absorption lines, the lowest being centered about 40 km (due to ions) and the other about 60 km. Figs. 49 through 51 show the integrated buildup of the magnitude of the y component of the reflected $\mathcal{H}$ field at the ground due to the integrated dipole structure of the ionosphere below the ordinate value. Note again the rather rapid (compared to Figs. 36 through 38) asymptotic approach of the curves to the 0.5 value.

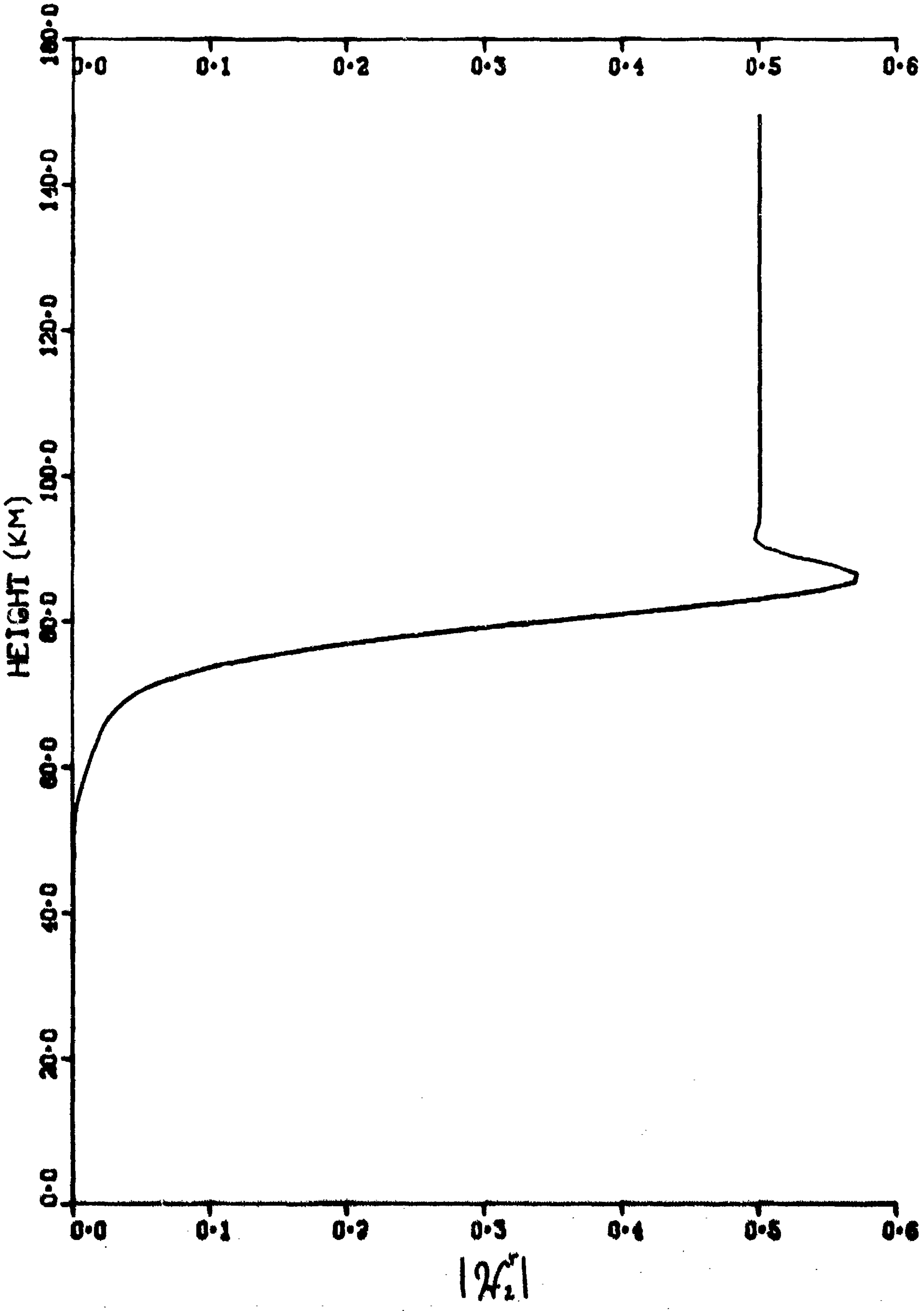

Fig. 42. Reflection Buildup for Day at the Magnetic Equator at 75 Hz.

Azimuth = 270°, Dip = 0°, Geomagnetic Field = 0.5 Gauss.

Fig. 43. Reflection Buildup for Day at the Magnetic Equator at 45 Hz.
Azimuth = 270°, Dip = 0°, Geomagnetic Field = 0.5 Gauss.

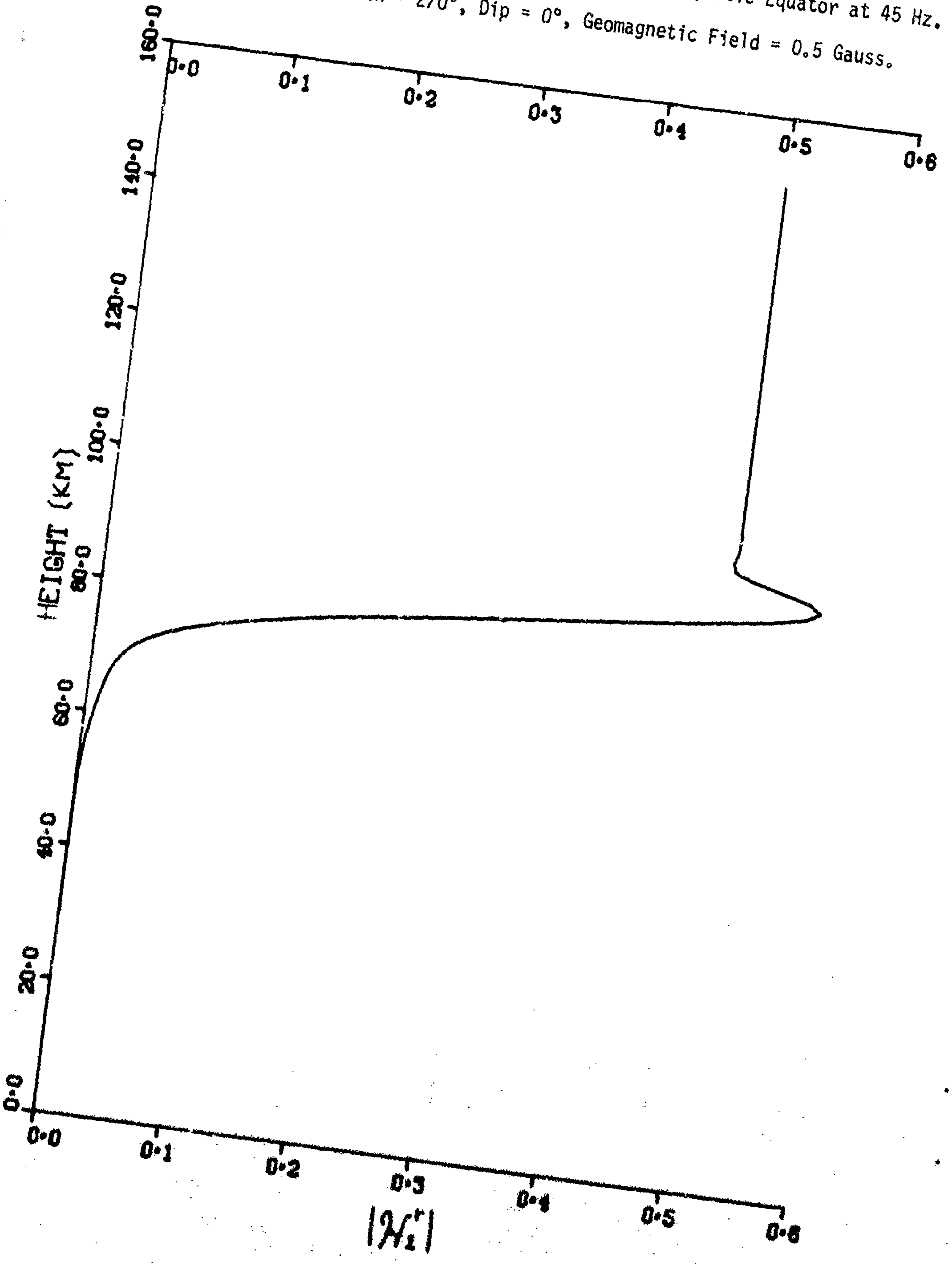

Fig. 44. Reflection Buildup for Day at the Magnetic Equator at 7.5 Hz.

Azimuth = 270°, Dip = 0°, Geomagnetic Field = 0.5 Gauss.

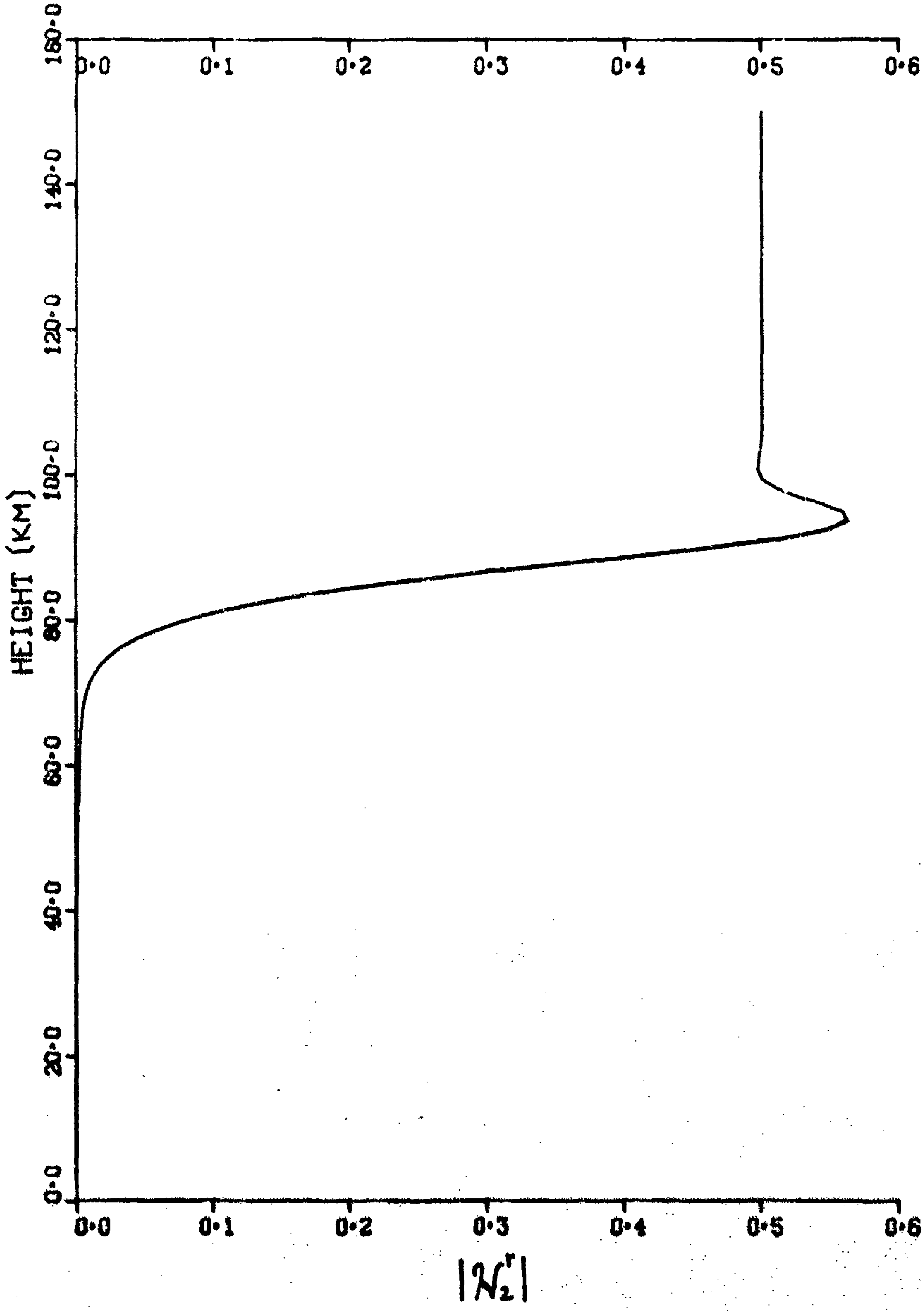

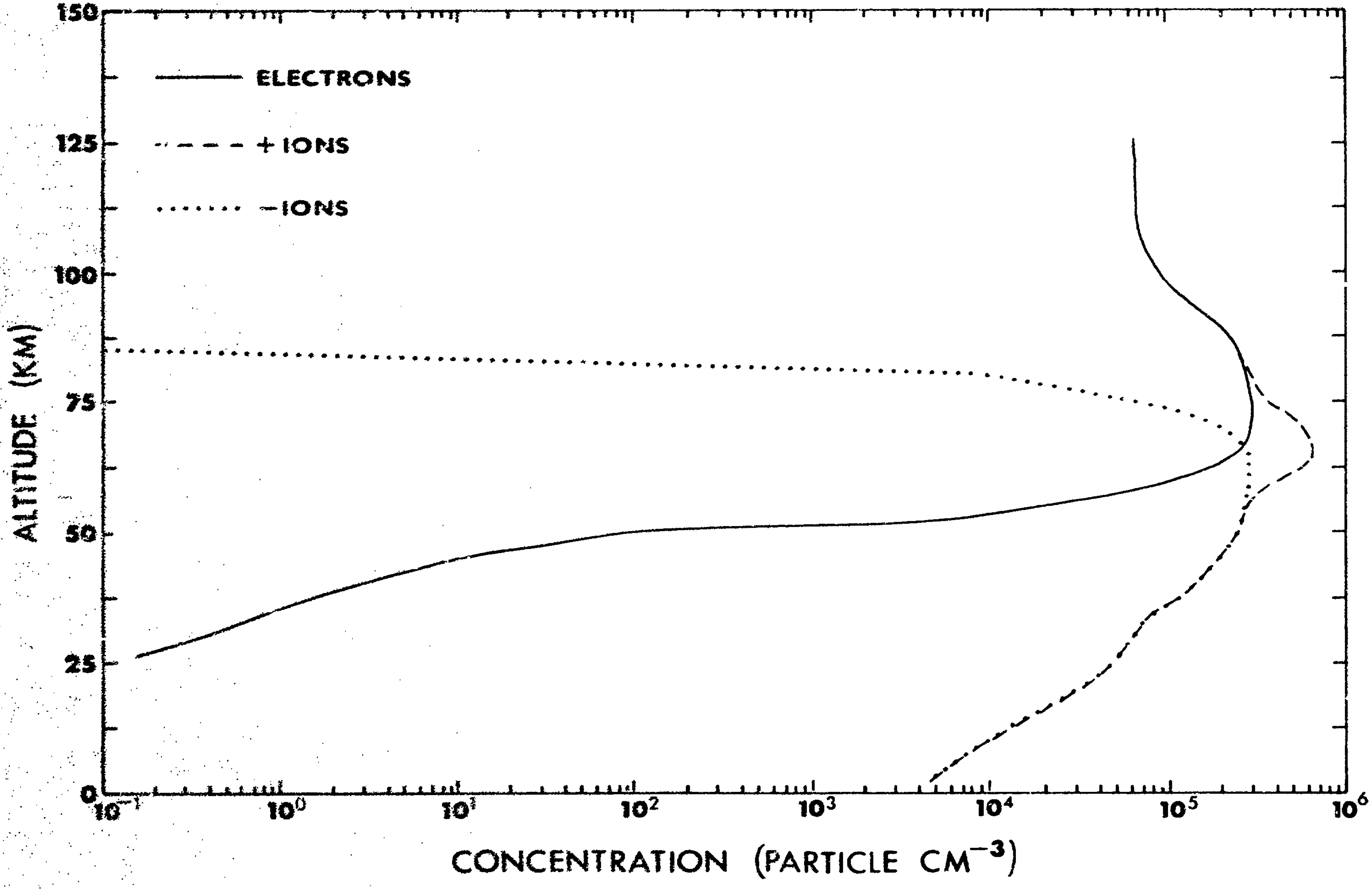

Fig. 45. Depressed Ionosphere Model.

Fig. 46. Reflection Density for Depressed Ionosphere at 75 Hz.

Azimuth = 45°, Dip = 75°, Geomagnetic Field = 0.5 Gauss.

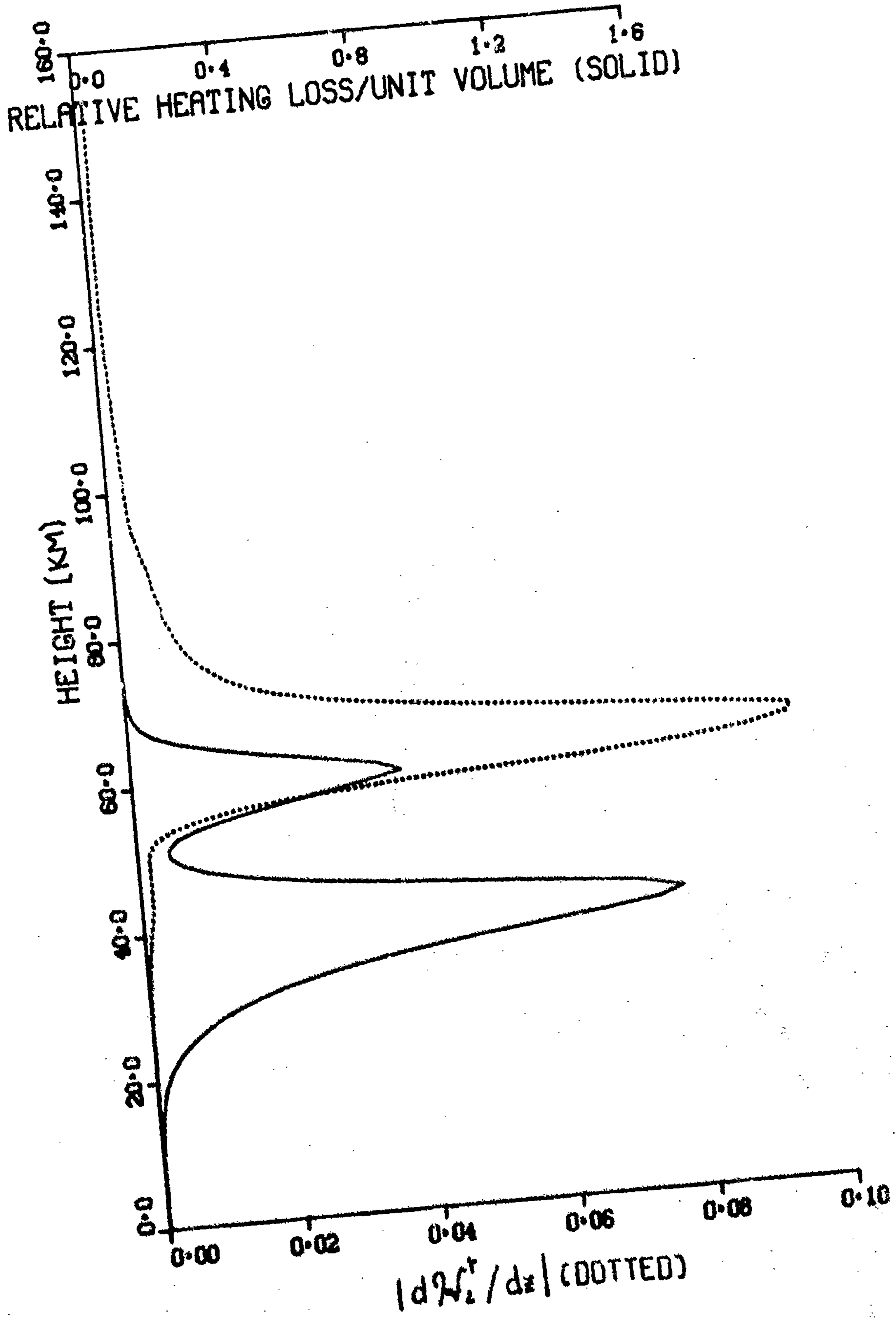

Fig. 47. Reflection Density for Depressed Ionosphere at 45 Hz. Azimuth = 45°, Dip= 75°, Geomagnetic Field = 0.5 Gauss.

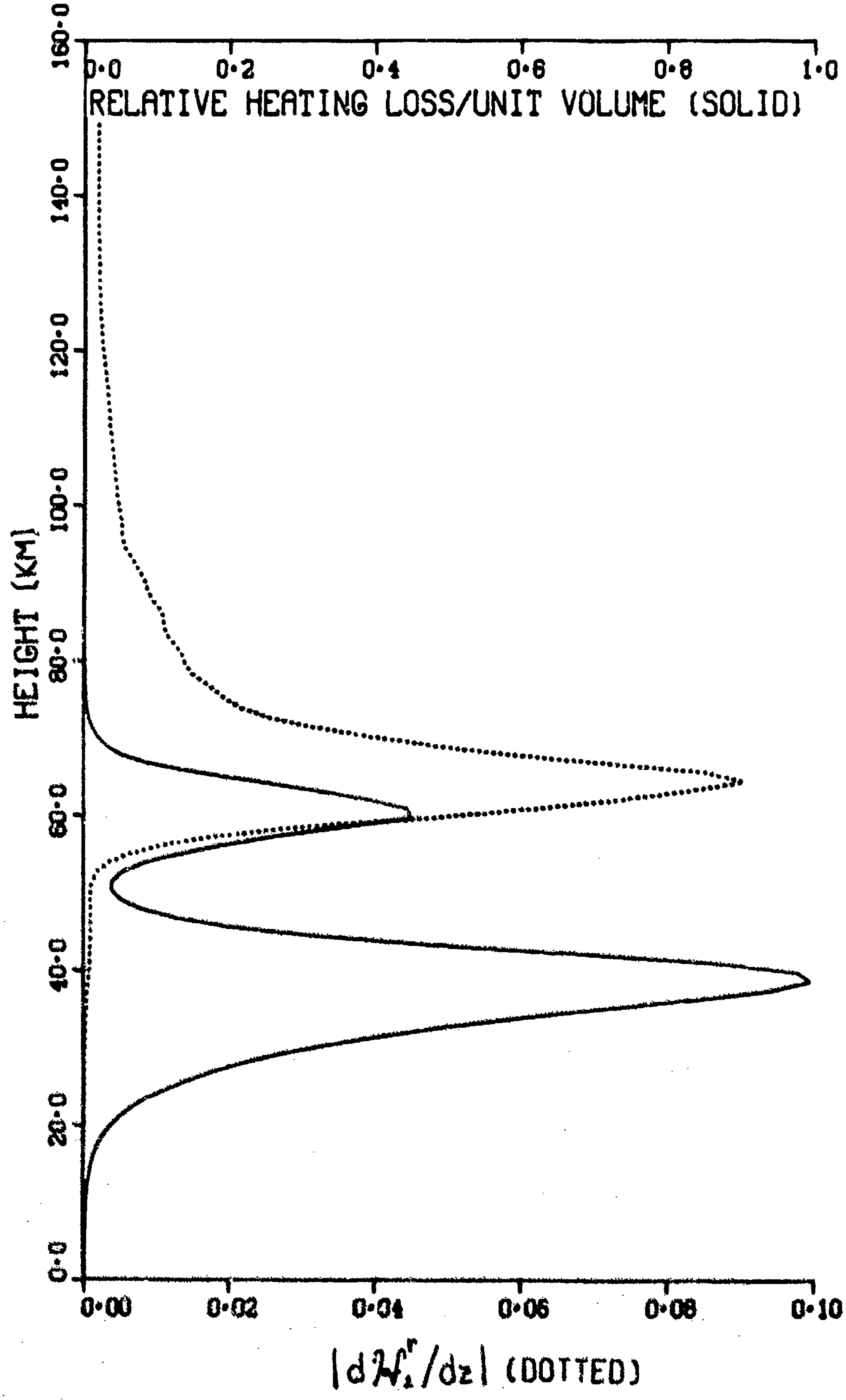

Fig. 48. Reflection Density for Depressed Ionosphere at 7.5 Hz.

Azimuth = 45°, Dip = 75°, Geomagnetic Field = 0.5 Gauss.

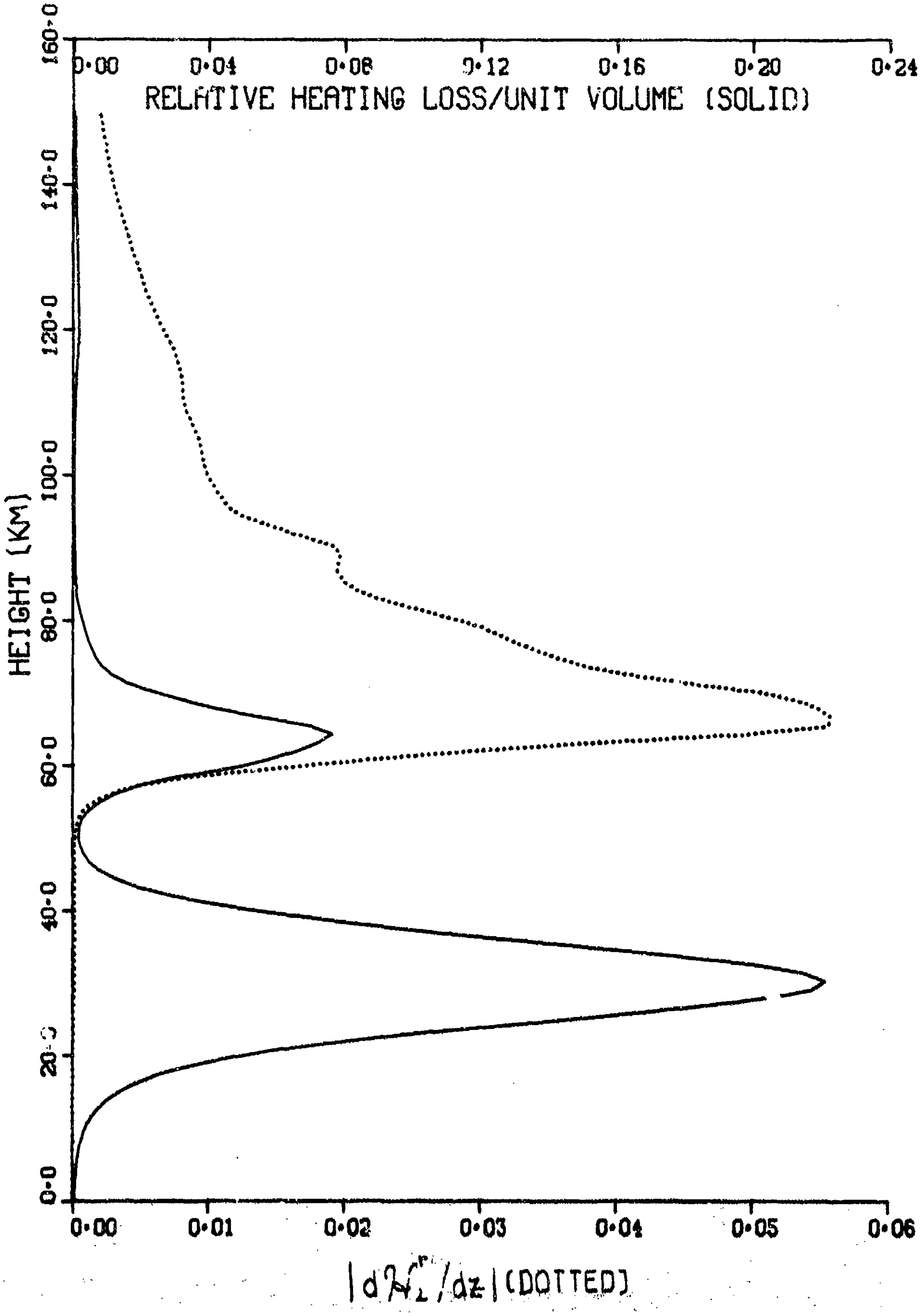

Fig. 49. Reflection Buildup for Depressed Ionosphere at 75 Hz, Azimuth = 45°, Dip = 75°, Geomagnetic Field = 0.5 Gauss.

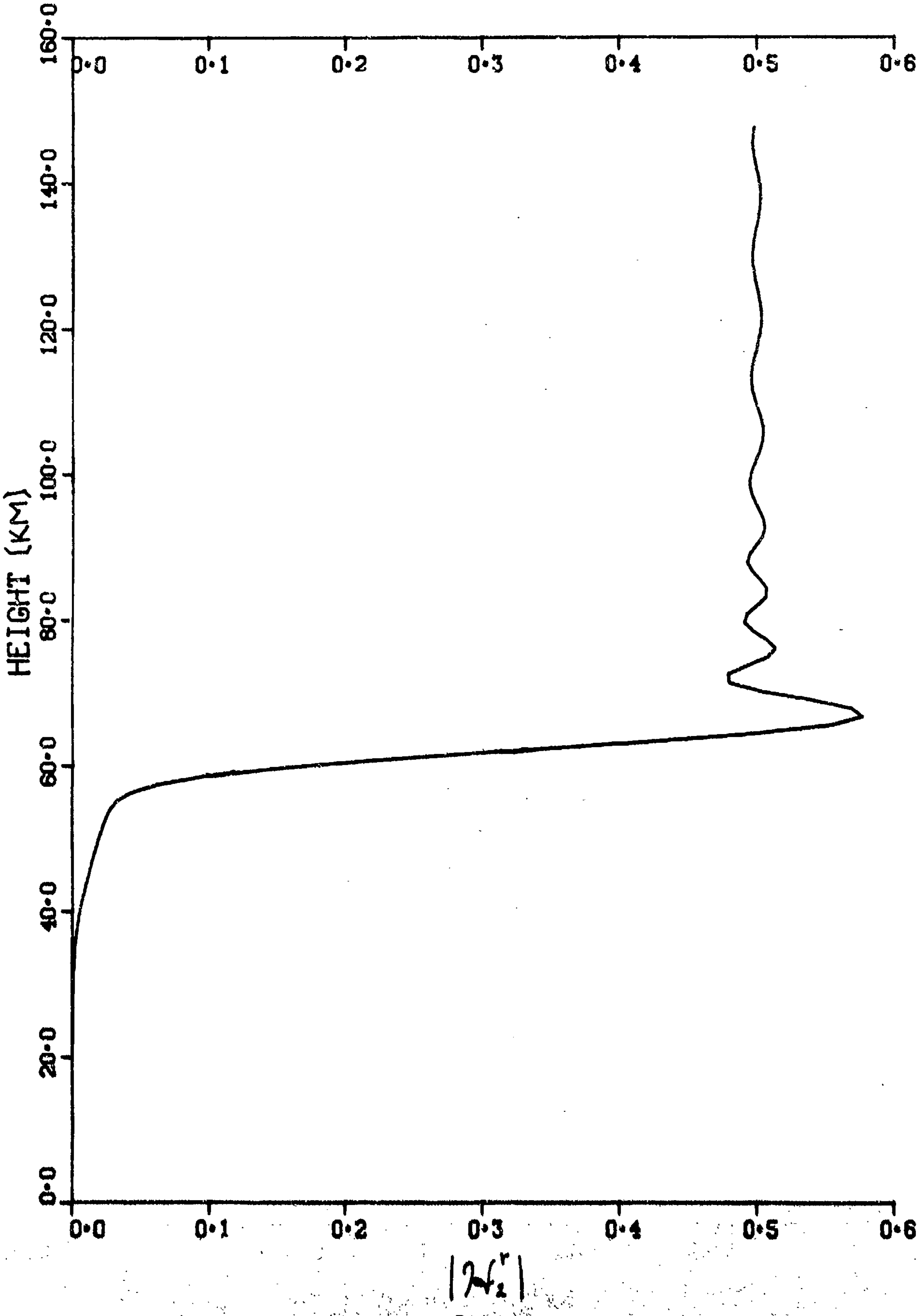

Fig. 50. Reflection Buildup for Depressed Ionosphere at 45 Hz.
Azimuth = 45°, Dip = 75°, Geomagnetic Field = 0.5 Gauss.

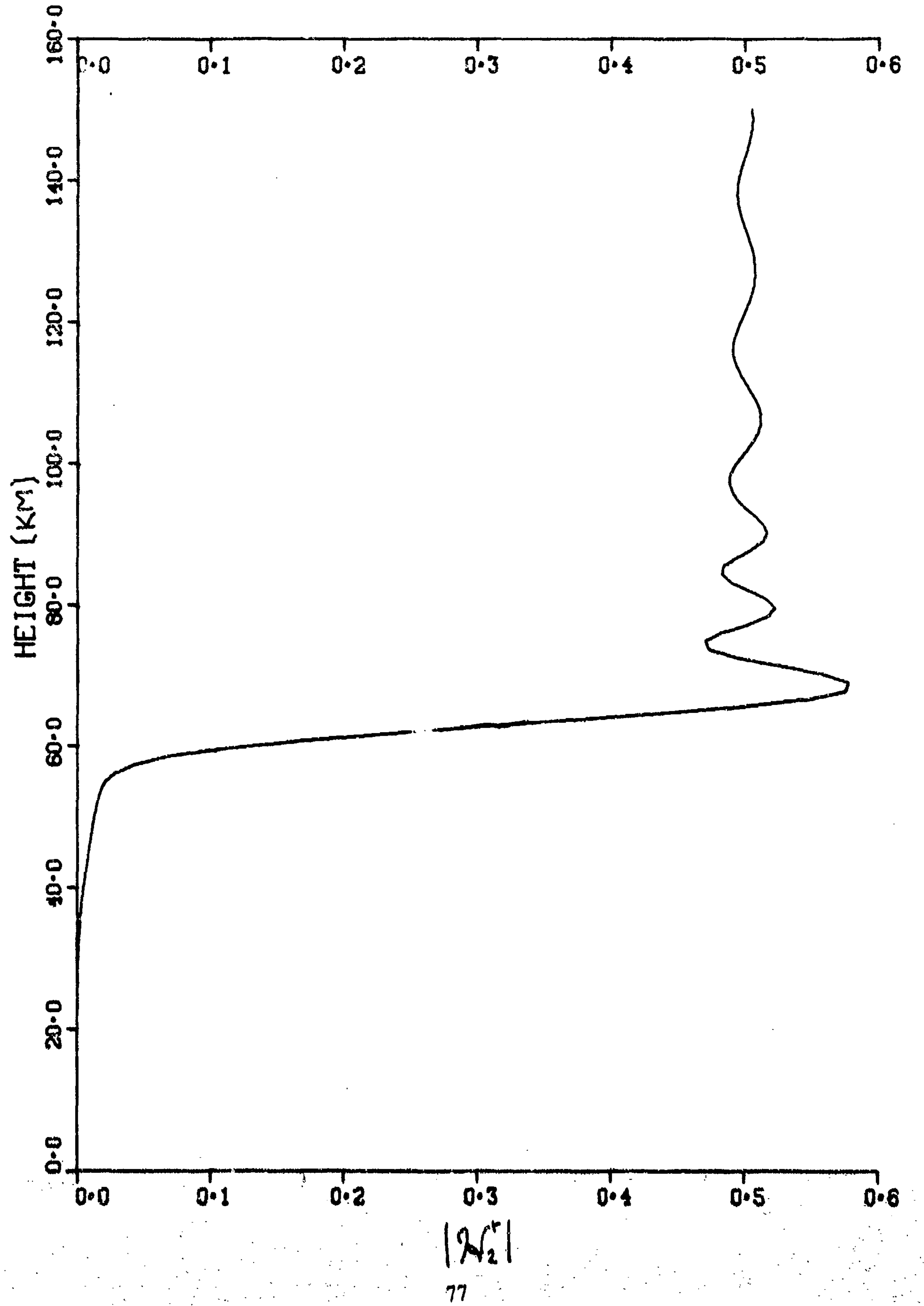

Fig. 51. Reflection Buildup for Depressed Ionosphere at 7.5 Hz.

Azimuth = 45°, Dip = 75°, Geomagnetic Field - 0.5 Gauss.

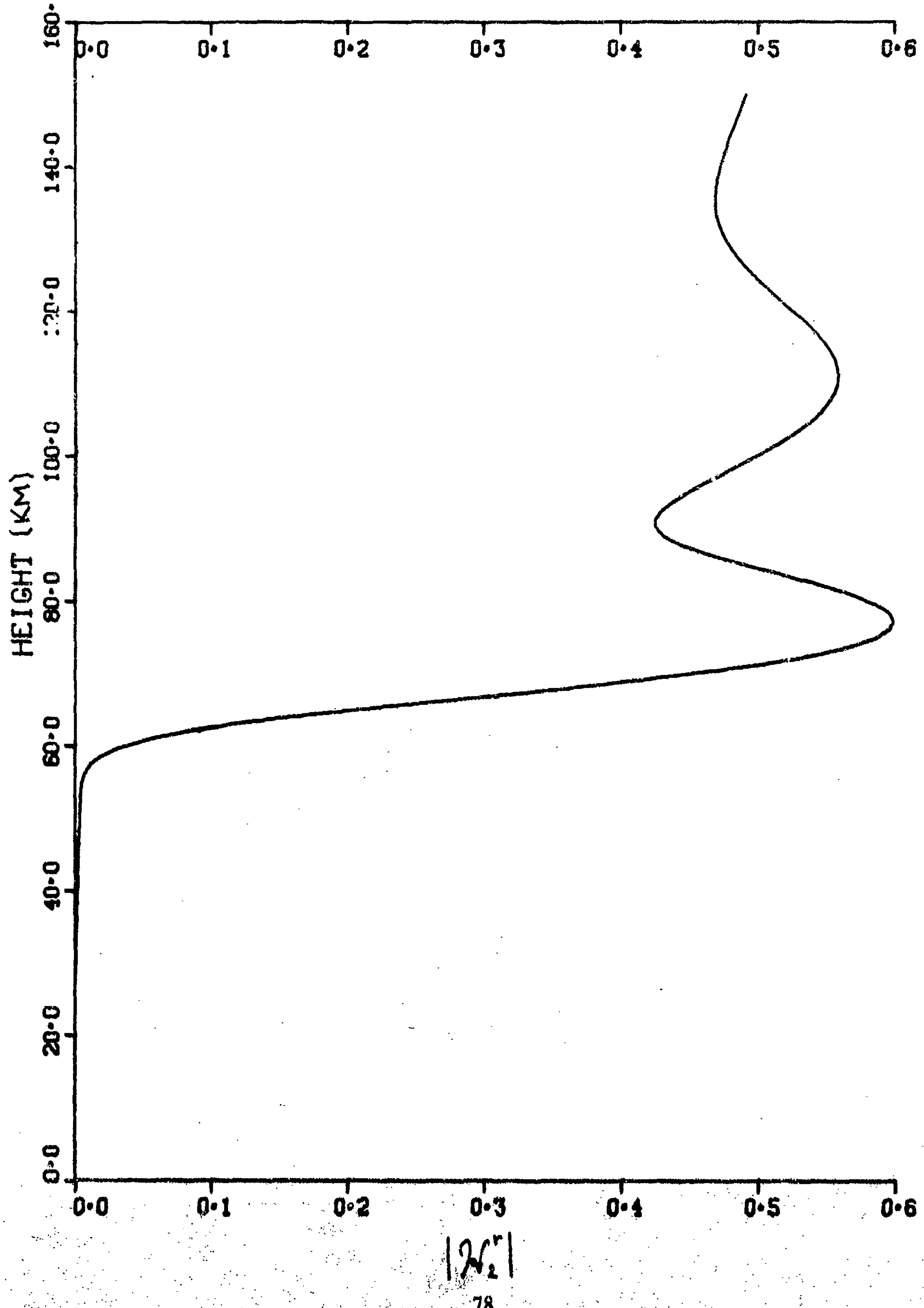

5. CONCLUSIONS

Under conditions of mid latitude propagation the full wave solutions for the day/night ambient profiles of Fig. 1 exhibit a low altitude absorption line, due principally to electrons, which peaks at about 55 km during the day and around 70 km during the night as well as a high altitude absorption line, due to ions, which peaks around 115 km for both day and night. Theoretical analysis, based on the assumption of scale height invariance of the profile species and their collision frequencies over the absorption line, suggests that the low altitude line shape should be essentially Lorentzian, whereas the high altitude absorption line shape should be approximately Gaussian. For the case studies examined, agreement between these theoretical line shapes and the fullwave line shapes is reasonably good in the Seafarer band (see Figs. 5, 6, 8, 9, 14, 15, 17, 18) but generally poor at the fundamental Schumann frequency because of the large halfwidths (see Figs. 7, 10, 16, 19).

Considerable attention has been given to the question of resonances in the attenuation associated with nighttime sporadic E layering. Fig. 25 shows that the sporadic E layer of Fig. (1) causes an order of magnitude enhancement in the attenuation at 78 Hz over the nighttime ambient result. About 40% of the enhanced value is due to the high altitude absorption, about 25% to absorption which occurs in the layer itself, about 25% to leakage above the sporadic E layer and about 10% to the low altitude absorption (see Fig. 26). It is concluded from the dipole reradiation theory that most of the reflection from the nighttime ambient profile close to the resonance frequency comes from a region about 20 km thick centered at 100 km. The sporadic E layer provides a strong reflection level at 120 km. This two level reflection characteristic suggested the simplified model of Fig. (29) and on the basis of this simplified model it has been concluded that the fundamental attenuation resonance is most accentuated when the separation between the two reflecting layers is one quarter of the local wavelength and when, simultaneously, the sporadic E layer thickness is also a quarter of the local wavelength. Both of these conditions are conducive to waveguiding between the two reflection levels. Although the effect is diminished for an ambient nighttime profile with a stronger E region ledge (as suggested by Booker and Lefeuvre[23]) it appears that the resonance could still be of practical significance (see Figs. 34, 35).

Subject to conditions of strong resonance, unlike the normal situation, the normal mode polarization contains significant amount of TE admixture. Thus, in future measurements of anomalous propagation of the type discussed in references 8 and 9 it is strongly recommended that a provision be made for measuring the extent of TE contaminant.

In the Seafarer band field penetration and re-radiation for the day ambient profile of Fig. 1 at mid latitudes, occurs up to at least altitudes of 90 km (see Figs. 36, 37). For the nighttime ambient profile of Fig. 1 at mid latitudes, significant field penetration and re-radiation occurs to altitudes of about 130 km (Fig. 20) for 75 Hz and to altitudes of about 145 km (Fig. 21) at 45 Hz.

For the daytime profile the re-radiation theory does not give a clearcut picture of the level where maximum re-radiation occurs, but rather yields an indecisive picture somewhat reminiscent of incidence on a pure dielectric. Unlike the daytime case, the level of maximum reflection based on the re-radiation theory for the satellite nighttime profile occurs at slightly above 100 kms for both 75 (Fig. 22) and 45 Hz (Fig. 23).

In a narrow angular band about the magnetic equator where quasi transverse propagation applies in the ionosphere the ambient profiles behave like metallic reflectors and the re-radiation theory gives very clearcut pictures of the reflective process in terms of levels and half widths (Figs. 39-41). This is also true for highly depressed ionospheres (Figs. 46-48).

REFERENCES

1. Budden, K.G., "The Waveguide Mode Theory of Wave Propagation," London, Logos, 1961.

2. Budden, K.G., "The Influence of the Earth's Magnetic Field on Radio Propagation by Waveguide Modes," Proc. Roy. Soc., Ser. A, vol. 265, pp. 538-553, 1962.

3. Wait, J.R., "Electromagnetic Waves in Stratified Media," New York, Pergamon, 1972.

4. Galeis, J., "Terrestrial Propagation of Long Electromagnetic Waves," New York, Pergamon, 1972.

5. Krasnushkin, P.E., "On the Propagation of Long and Very Long Radio Waves Around the Earth," Nuovo Cimento, Supp., vol. 26, pp. 50-112, 1962.

6. Private communication, W.F. Moler, Naval Ocean Systems Center, San Diego, Calif.

7. Imhof, W.L., Larsen, T.R., Reagan, J.B. and Gaines, E.E., "Analysis of Sattellite Data on Precipitating Particles in Coordination with ELF Propagation Anomalies," Lockheed Missiles and Space Company Report LMSC-D502063, 30 April 1976, pp. 99.

8. Bannister, P.R. "Variations in Extremely Low Frequency Propagation Parameters," J. Atmos. Terr. Phys., 37, pp. 1203-1210, 1975.

9. Davis, J.R., "Localized Nighttime D-Region Disturbances and ELF Propagation," J. Atmos. Terr. Phys. 38, pp. 1309-1317.

10. Smith, R.R., "A Program to Compute Ionospheric Height Gain Functions and Field Strengths," Interim Report No. 711, prepared for Defense Atomic Support Agency by the Naval Electronics Laboratory Center, Dec. 1970, pp.110.

11. Inoue, Y. and Horowitz, S., "Numerical Solution of Full-Wave Equation with Mode Coupling," Radio Science, Vol. 1, No. 8, pp. 957-970, 1966.

12. Pitteway, M.L.V., "The Numerical Calculation of Wave-Fields, Reflection Coefficients and Polarizations for Long Radio Waves in the Lower Ionosphere - I," Phil. Trans. Roy. Soc. (London), Ser. A257, No. 1079, pp. 219-241, 1965.

13. Pappert, R.A., Moler, W.F., "Propagation Theory and Calculations at Lower Extremely Low Frequencies (ELF)," IEEE Trans. on Comm., Vol. COM-22, No. 4, pp. 438-451, 1974.

14. Clemmow, P.C., and Heading, J., "Coupled Forms of the Differential Equations Governing Radio Propagation in the Ionosphere," Proc. Cambridge Phil. Soc. 50, pp. 319-333, 1954.

15. Budden, K.G., Radio Waves in the Ionosphere, London, Cambridge, 1961.

16. Westcott, B.S., Ionospheric Reflection Processes for Long Radio Waves-I, J. Atmos. Terr. Phys. 24, pp. 385-399, 1962.

17. Westcott, B.S., Ionospheric Reflection Processes for Long Radio Waves-II, J. Atmos. Terr. Phys., 24, pp. 619-631, 1962.

18. Westcott, B.S., Ionospheric Reflection Processes for Long Radio Waves-III, J. Atmos. Terr. Phys., 24, pp. 701-713, 1962.

19. Westcott, B.S., Ionospheric Reflection Processes for Long Radio Waves-IV, J. Atmos. Terr. Phys., 24, pp. 921-936, 1962.

20. Westcott, B.S., Ionospheric Reflection Processes for Long Radio Waves-V, J. Atmos. Terr. Phys., 26, pp. 341-350, 1964.

21. Hartree, D.R., "The Propagation of Electromagnetic Waves in a Stratified Medium," Proc. Cambridge Phil. Soc., 25, pp. 97-120, 1929.

22. Darwin, C.G., "Optical Constants of Matter", Trans. Cambridge, Phil. Soc., 50, pp. 137-160, 1924.

23. Booker, H.G. and Lefeuvre, F., "The Relation Between Ionospheric Profiles and ELF Propagation in the Earth-Ionosphere Transmission Line" To be published in JATP.

24. Booker, H.G., "The Elements of Wave Propagation Using the Impedance Concept", Journal of the IEE 94, pp. 171-204, 1948.

25. Gilbert, J.L., "Sporadic E-Layer Effects on ELF Propagation: A Simple Model", MRC-N-265 Prepared for Dept. of Navy, Naval Electronics Systems Command by Mission Research Corp., Nov. 1976, pp.43.

26. Field, E.C., "Propagation of ELF Waves under Normal and Naturally Disturbed Conditions," Journal of Geophysical Research, 74, No. 14, pp. 3639-3650, 1969.

APPENDIX A

Low Altitude Absorption

The low altitude absorption occurs where the electric field components of the rf wave satisfy the following inequality

$$|E_3| >> |E_1|, |E_2| \qquad \text{A.1}$$

where the indices 1, 2, 3 stand for x, y and z respectively. Thus the low altitude absorption is due principally to the vertical electric field component so that

$$\begin{aligned} J &\simeq \mathrm{Re}\ [\, i E_3^* E_3 M_{33}\,] \\ &\simeq \mathrm{Re}\left[i \frac{E_b^*}{(1+M_{33})^*} \frac{E_b}{(1+M_{33})} M_{33} \right] \end{aligned} \qquad \text{A.2}$$

where E_b represents the vertical electric field component at the base of the ionosphere (E_b to very good approximation may be taken equal to the vertical electric field at the ground). The substitution of $E_b/(1 + M_{33})$ for E_3 is a consequence of continuity of the vertical component of the displacement vector along with the inequality A.1. We will first limit the discussion to the case for which $\nu_j >> \Omega_j$, ω for all species. Then

$$M_{33} \simeq -i \sum_{j=1}^{N} X_j \qquad \text{A.3}$$

where j is a species index including both electrons and ions and

$$X_j = \frac{\omega_{pj}^2}{\omega \nu_j} \qquad \text{A.4}$$

Observe that X_j is real. Substituting A.3 into A.2 yields,

$$J \simeq |E_b|^2 \frac{1}{\sum_{j=1}^{N} X_j + \left(\sum_{j=1}^{N} X_j \right)^{-1}} \qquad \text{A.5}$$

This maximizes at that altitude, z_0, for which

$$\sum_{j=1}^{N} X_j(z_0) = 1 \qquad \text{A.6}$$

From (A.5) the line shape in the neighborhood of z_0 may be written as

(normalization is to unity at $z=z_0$)

$$J \simeq \frac{1}{1+\frac{1}{2}\left[(z-z_0)\sum_{j=1}^{N} X_j'(z_0)\right]^2} \qquad \text{A.7}$$

where the prime denotes the derivative with respect to z. If the profile densities and collision frequencies are assumed to vary exponentially in the neighborhood of z_0 with scale heights that are invariant over the line profile then A.7 becomes

$$J \simeq \frac{1}{1+\frac{1}{2}\left[(z-z_0)\sum_{j=1}^{N} X_j(z_0)(\alpha_j+\gamma_j)\right]^2} \qquad \text{A.8}$$

where α and γ are inverse scale heights at z_0 for the profiles and collision frequencies respectively. Equation A.8 has been compared with the full wave low altitude absorption line shape in section 4.

Equation (5) can be used, along with the preceding equations to estimate the integrated effect of the low altitude absorption line. Since π_1 decreases quite rapidly above the level z_0 and since it is nearly constant between z_0 and the ground it follows that

$$\int_0^h \pi_1\,dz \simeq \int_0^{z_0} \pi_1\,dz \simeq \frac{|H_2|^2}{2Z_0}\,\mathrm{Re}\,(S)\,z_0 \qquad \text{A.9}$$

Using the Lorentzian line profiles just discussed, the integral of J over the line becomes

$$\int_{\mathrm{Line}} J\,dz \simeq \pi\sqrt{2}\;\epsilon_0\omega\,|S|^2\,|H_2|^2/(4\beta) \qquad \text{A.10}$$

where

$$\beta = \sum_{j=1}^{M} X_j'(z_0) \qquad \text{if A.7 is used} \qquad \text{A.11}$$

$$= \sum_{j=1}^{M} X_j(z_0)(\alpha_j+\gamma_j) \qquad \text{if A.8 is used} \qquad \text{A.12}$$

Combining factors, Eq (8) yields the following estimate for the integrated low altitude absorption (measured in terms of attenuation)

$$\beta_A \simeq \frac{0.2\, f\, |S|^2}{\mathrm{Re}(S)\, \beta\, z_o} \ \mathrm{dB}/_{1000\ \mathrm{km}} \qquad \text{A.13}$$

with f the frequency in Hz.

Recall that the preceding equations have been developed subject to the condition that $\nu_j >> \Omega_j$ for all species. This condition is satisfied for the daytime low altitude absorption and is also true for all species, except possibly electrons, for the low altitude nighttime absorption. If for a given species

$$|n|\omega_{cj} >> \nu_j \qquad \text{A.14}$$

then the only change in the preceding development is that the term in A.3 corresponding to that species is to be multiplied by n^2 where n is the direction cosine between the geomagnetic field and the z axis. Although A.14 is only marginally satisfied, this factor has been included for electrons in the 45 and 75 Hz results for the nighttime profile discussed in section 4.

APPENDIX B

High Altitude Absorption

To arrive at an estimate for the location of the high altitude absorption and a formula for its line shape, it will be assumed that it occurs in an altitude region where only the outgoing whistler mode has survived. The index of refraction, assuming just a single species of + ions, for the whistler mode is (in this appendix the subscript e is for electrons and i for ions):

$$N^2 = 1 + \frac{\omega_{pe}^2}{\omega(-\omega + \Omega_e + i\nu_e)} + \frac{\omega_{pi}^2}{\omega(-\omega - \Omega_i + \nu_i)} \qquad \text{B.1}$$

where

$$\Omega_e = |n|\omega_{ce}, \ \Omega_i = |n|\omega_{ci} \qquad \text{B.2}$$

Since $\Omega_e >> \omega, \ \nu_e$, Eq (B.1) becomes

$$\begin{aligned} N^2 &\simeq 1 + \frac{\omega_{pe}^2}{\omega\Omega_e}\left(1 - \frac{i\nu_e}{\Omega_e}\right) - \frac{\omega_{pi}^2(\omega + \Omega_i + i\nu_i)}{\omega[(\omega + \Omega_i)^2 + \nu_i^2]} \\ &= 1 + \frac{\omega_{pe}^2}{\omega\Omega_e}\left(1 - \frac{\Omega_i(\omega + \Omega_i)}{[(\omega + \Omega)_i^2 + \nu_i^2]}\right) \\ &\quad - i\frac{\omega_{pe}^2}{\omega\Omega_e}\left(\frac{\Omega_i\nu_i}{(\omega+\Omega_i)^2+\nu_i^2} + \frac{\nu_e}{\Omega_e}\right) \end{aligned} \qquad \text{B.3}$$

Now in the altitude region of interest B.4

$$\frac{\Omega_i\nu_i}{(\omega + \Omega_i)^2 + \nu_i^2} >> \frac{\nu_e}{\Omega_e} \text{ and } \frac{\omega_{pe}^2}{\omega\Omega_e} >> 1$$

and to a reasonable approximation B.5

$$1 >> \frac{\Omega_i(\omega + \Omega_i)}{(\omega + \Omega_i)^2 + \nu_i^2}$$

Thus B.3 is further approximated to give

$$N^2 \simeq \frac{\omega_{pe}^2}{\omega\Omega_e}\left(1 - i\,\frac{\Omega_i\,\nu_i}{(\omega+\Omega_i)^2+\nu_i^2}\right) \qquad \text{B.6}$$

The second term in the parenthesis of B.6 can be no larger than 0.5, thus we assume

$$\frac{\Omega_i\nu_i}{(\omega+\Omega_i)^2+\nu_i^2} << 1 \qquad \text{B.7}$$

and finally obtain

$$N \simeq \sqrt{\frac{\omega_{pe}^2}{\omega\Omega_e}}\left(1 - \frac{1}{2}\,i\,\frac{\Omega_i\nu_i}{(\omega+\Omega_i)^2+\nu_i^2}\right) \qquad \text{B.8}$$

From (B.6) the conductivity may be identified to be

$$\sigma = \epsilon_0\frac{\omega_{pe}^2\,\Omega_i\nu_i}{\Omega_e\,[(\omega+\Omega_i)^2+\nu_i^2]} = \epsilon_0\frac{\omega_{pi}^2\nu_i}{(\omega+\Omega_i)^2+\nu_i^2}$$

whereas the imaginary part of N from (B.8) is

$$\operatorname{Im} N = -\frac{1}{2}\sqrt{\frac{\omega_{pe}^2}{\omega\Omega_e}}\;\frac{\Omega_i\nu_i}{(\omega+\Omega_i)^2+\nu_i^2} = -\frac{1}{2}\,\omega_{pi}\sqrt{\frac{\Omega_i}{\omega}}\;\frac{\nu_i}{(\omega+\Omega_i)^2+\nu_i^2} \qquad \text{B.9}$$

Thus in the high altitude region the absorption per unit volume varies as

$$J \sim \frac{\omega_{pi}^2\,\nu_i}{(\omega+\Omega_i)^2+\nu_i^2}\,e^{-\frac{\sqrt{\omega\Omega_i}}{c}\int^z \frac{\omega_{pi}\,\nu_i}{(\omega+\Omega_i)^2+\nu_i^2}\,dz} \qquad \text{B.10}$$

The problem of finding the height, z_0, where the high altitude absorption maximizes is tantamount to maximizing the function

$$G(z) = \ln[\omega_{pi}^2\nu_i/((\omega+\Omega_i)^2+\nu_i^2)] - \frac{\sqrt{\omega\Omega_i}}{c}\int^z \frac{\omega_{pi}\nu_i}{(\omega+\Omega_i)+\nu_i^2}\,dz \qquad \text{B.11}$$

Assuming that the ion density and collision frequency vary exponentially in the neighborhood of z_0 with scale heights that are invariant over the line profile then (B.10) maximizes at that height, z_0, for which

$$\frac{\sqrt{\omega \Omega_i}}{c} \; \frac{\omega_{pi} \nu_i}{(\omega + \Omega_i)^2 + \nu_i^2} - \frac{2\gamma_i \, \nu_i^2}{(\omega + \Omega_i)^2 + \nu_i^2} + \alpha_i - \gamma_i = 0 \qquad \text{B.12}$$

where α and γ are inverse scale heights for the density and collision frequency respectively.

In the neighborhood of z_0 the absorption line assumes a Gaussian line shape with half width determined by evaluating the second derivative of G (i.e., B.11) at z_0. Carrying through this procedure yields for the high altitude line shape

$$J \sim \exp\left[-\frac{1}{2} \left(\frac{\alpha_i^2}{2} + \gamma_i^2 - \frac{3}{2} \; \alpha_i \gamma_i \, \frac{(\omega + \Omega_i)^2 - \nu_i^2}{(\omega + \Omega_i)^2 + \nu_i^2} \right) (z - z_0)^2 \right] \qquad \text{B.13}$$

Equation B.13 along with B.12 has been used in section 4 to compare with the location and shape of the full wave high altitude absorption. The integrated intensity of the line, unlike the low altitude absorption line, cannot be so easily approximated since it depends upon the transmission through the D and E layers.

APPENDIX C

Resonance For A Simplified Model

The discussion in this appendix is based on the simplified model shown in Fig. (29). It will be assumed that the altitude range $z_2 - z_1$, is sufficiently large that although both extraordinary and ordinary wave exists at the altitude z_1 only extraordinary wave exists at z_2. Denoting the extraordinary wave by the superscript x and the ordinary wave by the superscript o, the total rf field components E_1, E_2, $\mathcal{H}_1$, $\mathcal{H}_2$ at the ground z=o, in terms of the extraordinary and ordinary field components, $E_1^{x,o}$, $E_2^{x,o}$, $\mathcal{H}_1^{x,o}$, $\mathcal{H}_2^{x,o}$ at z_1 are

$$E_1 = E_1^x \cos kCz_1 + E_1^o \cos kCz_1 + iC\mathcal{H}_2^x \sin kCz_1 + iC\mathcal{H}_2^o \sin kCz_1 \qquad \text{C.1}$$

$$E_2 = E_2^x \cos kCz_1 + E_2^o \cos kCz_1 - \frac{i}{C}\mathcal{H}_1^x \sin kCz_1 - \frac{i}{C}\mathcal{H}_1^o \sin kCz_1 \qquad \text{C.2}$$

$$\mathcal{H}_1 = \mathcal{H}_1^x \cos kCz_1 + \mathcal{H}_1^o \cos kCz_1 - iCE_2^x \sin kCz_1 - iCE_2^o \sin kCz_1 \qquad \text{C.3}$$

$$\mathcal{H}_2 = \mathcal{H}_2^x \cos kCz_1 + \mathcal{H}_2^o \cos kCz_1 + \frac{i}{C} E_1^x \sin kCz_1 + \frac{i}{C} E_1^o \sin kCz_1 \qquad \text{C.4}$$

With allowance for co-ordinate system differences, these equations can be derived following Booker.[24]

In the following development it is assumed that the extraordinary index of refraction, n_{xj}, and the ordinary index of refraction n_{oj}, for regions j=2, 3 and 4 satisfy the condition

$$|n_{oj}^2|, |n_{xj}^2| >> |S^2| \qquad j=2,3,4$$

Assuming, then, vertical propagation of the extraordinary wave between z_1 and z_2 and the total decay of the ordinary wave at z_2 the field components $E_1^{x,o}$, $E_2^{x,o}$, $\mathcal{H}_1^{x,o}$, $\mathcal{H}_2^{x,o}$ at z_1 may all be expressed in terms of two independent quantities A and B as follows

$$E_1^x = \frac{A}{n_{x2}}(1-Q) \quad , \quad E_1^o = \frac{B}{n_{o2}} \qquad \text{C.5}$$

$$E_2^x = i\,\frac{A}{n_{x2}}(1-Q) \quad , \quad E_2^o = -i\,\frac{B}{n_{o2}} \qquad \text{C.6}$$

$$\mathcal{H}_1^x = -i\,A\,(1+Q) \quad , \quad \mathcal{H}_1^o = iB \qquad \text{C.7}$$

$$\mathcal{H}_2^x = A(1+Q) \quad , \quad \mathcal{H}_2^o = B \qquad \text{C.8}$$

where

$$Q = R\exp(-2\,ikn_{x2}(z_2 - z_1)) \qquad \text{C.9}$$

$$R = \frac{r_{23} + r_{34}\exp(-2\,ikn_{x3}(z_3 - z_2))}{1 + r_{23}r_{34}\exp(-2\,ikn_{x3}(z_3 - z_2))} \qquad \text{C.10}$$

$$r_{23} = \frac{n_{x3} - n_{x2}}{n_{x3} + n_{x2}} \qquad \text{C.11}$$

$$r_{34} = \frac{n_{x4} - n_{x3}}{n_{x4} + n_{x3}} \qquad \text{C.12}$$

Substituting C.5 through C.8 into C.1 through C.4 yields

$$E_1 = \left[\frac{1-Q}{n_{x2}}\cos kCz_1 + iC(1+Q)\sin kCz_1\right]A + \left[\frac{1}{n_{o2}}\cos kCz_1 + iC\sin kCz_1\right]B \qquad \text{C.13}$$

$$E_2 = \left[\frac{i(1-Q)}{n_{x2}}\cos kCz_1 - \frac{(1+Q)}{C}\sin kCz_1\right]A + \left[-\frac{i}{n_{o2}}\cos kCz_1 + \frac{1}{C}\sin kCz_1\right]B \qquad \text{C.14}$$

$$\mathcal{H}_1 = \left[-i(1+Q)\cos kCz_1 + \frac{C}{n_{x2}}(1-Q)\sin kCz_1\right]A + \left[i\cos kCz_1 - \frac{C}{n_{o2}}\sin kCz_1\right]B \qquad \text{C.15}$$

$$\mathcal{H}_2 = \left[(1+Q)\cos kCz_1 + \frac{i}{Cn_{x2}}(1-Q)\sin kCz_1\right] A + \left[\cos kCz_1 + \frac{i}{Cn_{o2}}\sin kCz_1\right] B \qquad \text{C.16}$$

Assuming a perfectly conducting ground, the conditions

$$E_1 = E_2 = 0 \qquad \text{C.17}$$

must be fulfilled. After some algebra, the conditions C.17 can be manipulated into the following form for the modal equation

$$Q\left[\frac{\cos kCz_1\left(\frac{2i\cos kCz_1}{n_{o2}n_{x2}} - \frac{\sin kCz_1}{n_{x2}}\left(C+\frac{1}{C}\right)\right) + \sin kCz_1\left(2i\sin kCz_1 + \frac{\cos kCz_1}{n_{o2}}\left(C+\frac{1}{C}\right)\right)}{\cos kCz_1\left(-\frac{2i\cos kCz_1}{n_{o2}n_{x2}} + \frac{\sin kCz_1}{n_{x2}}\left(C+\frac{1}{C}\right)\right) + \sin kCz_1\left(2i\sin kCz_1 + \frac{\cos kCz_1}{n_{o2}}\left(C+\frac{1}{C}\right)\right)}\right]$$

$$+1=0 \qquad \text{C.18}$$

Further reasonable approximations for the cases of interest here are

$$kCz_1 << 1$$

$$|n_{o2}n_{x2}| >> kz_1\,|n_{o2}|\,,\; kz_1\,|n_{x2}| >> 1 \qquad \text{C.19}$$

Using these conditions it is a straightforward exercise to show that correct to order $(kz_1\,|n_{x2}|)^{-1}$ Eq (C.18) becomes

$$Q\left[1 + \frac{i}{kz_1 n_{x2}}\,(1 + C^{-2})\right] + 1 = 0 \qquad \text{C.20}$$

or equivalently to order $(kz_1\,|n_{x2}|)^{-1}$ by

$$Q\exp\left[\frac{i}{kz_1 n_{x2}}\,(1 + C^{-2})\right] + 1 = 0 \qquad \text{C.21}$$

Substituting C.9 for Q into C.21, the latter becomes

$$\exp\left[-2ikn_{x2}(z_2 - z_1) + \frac{i}{kz_1 n_{x2}}\,(1 + C^{-2}) + \ln R\right] = -1 \qquad \text{C.22}$$

Taking $R=e^{-\delta+i\beta}$, C.22 yields for the square of the cosine of the eigenangle

$$C^2 = \frac{1}{kz_1 n_{x2}\left[\,2\,kn_{x2}(z_2 - z_1) - (2p+1)\pi - \dfrac{1}{kz_1 n_{x2}} - \beta - i\delta\,\right]} \qquad \text{C.23}$$

where p = 0, 1, 2 . . .

If

$$\frac{|\mathrm{Im}\,(n_{x2})|}{|\mathrm{Re}\,(n_{x2})|} << 1 \text{ and } \delta << 1\,, \qquad \text{C.24}$$

Eq. C.23 yields a sharp resonance behavior for C^2 as well as for the attenuation,

$$\alpha = -8.68\,k\,\mathrm{Re}(S) \times 10^3 \ \text{dB/1000 km}\,, \qquad \text{C.25}$$

where S is the sine of the eigenangle. If in addition to the conditions C.19,

$$\beta << 1, \qquad \text{C.26}$$

the resonance condition is

$$z_2 - z_1 = \frac{2p+1}{4}\left(\frac{\lambda_0}{\mathrm{Re}\,(n_{x2})}\right)\,; \quad \lambda_0 = \text{free space wavelength} \qquad \text{C.27}$$

Since $\lambda_0/\mathrm{Re}(n_{x2})$ is the local wavelength in region 2, a primary condition for resonance in this instance is that region 2 serve as a quarter waveplate. The first condition of C.24 is always true for cases of interest here so that the second condition of C.24 becomes the crucial one. For the cases of interest here, namely

$$|n_{x3}| >> |n_{x2}|, |n_{x4}| \qquad \text{C.28}$$

the second condition of C.24 will be best satisfied when the layer, region 3, also has a thickness close to quarter integer multiples of the local wavelength in region 3. Also, the condition most detrimental to a sharp resonance is the condition that the layer, region 3, has a thickness close to half integer multiples of the local wavelength. To understand better the origin of these conditions, consider C.10 subject to the qualification that regions 2 and 4 have identical charge densities and collision frequencies. Then subject to the first condition of C.24 and conditions C.28 it follows for

$$-2ikn_{x3}(z_3 - z_2) = (-2p\pi - \epsilon)i - 2k\,|\mathrm{Im}(n_{x3})|(z_3 - z_2)\ ;\ \ p = 1, 2, 3 \ldots \qquad \text{C.29}$$

and for

$$\epsilon,\ 2k\,|\mathrm{Im}(n_{x3})|(z_3 - z_2) << 1 \qquad \text{C.30}$$

that C.10 becomes approximately

$$R \simeq \frac{2k|\mathrm{Im}(n_{x3})|(z_3 - z_2) + i\epsilon}{2k|\mathrm{Im}(n_{x3})|(z_3 - z_2) + i\epsilon + 4\,n_{x2}/n_{x3}} \qquad \text{C.31}$$

For conditions of primary interest here

$$2k|\mathrm{Im}(n_{x3})|(z_3 - z_2) << 4|n_{x2}/n_{x3}| \qquad \text{C.32}$$

If in addition

$$\epsilon << 4|n_{x2}/n_{x3}| \qquad \text{C.33}$$

it follows that $R<<1$ so that the δ term in C.23 will tend to smear the resonance.

If instead of C.29 the condition

$$-2ikn_{x3}(z_3 - z_2) = -((2p + 1)\pi + \epsilon)i - 2k|\mathrm{Im}(n_{x3})|(z_3 - z_2)\ ;\ \ p = 0,1,2 \ldots \qquad \text{C.34}$$

is imposed and conditions C.30 satisfied it follows that $R=1$ to first order in ϵ, $k|I_m(n_{x3})|(z_3-z_2)$ and n_{x2}/n_{x3} . Thus, subject to these conditions, the resonance peak should be accentuated when C.34 is satisfied. It is interesting to note that contrary to the preceding findings, the condition C.29 rather than C.34 was previously suggested as being the condition for strong resonance.[25] In section 4 results of calculations based on C.23 will be given which illustrate the foregoing behavior.

For the more general case of two reflecting layers separated by an inhomogeneous medium, we would expect C.25 to be replaced by

$$\int_{z_1}^{z_2} \mathrm{Re}\,(n_{x2})\,dz = (2p+1)\lambda_0/4 \;;\quad p = 0, 1, 2, 3, \text{etc.} \tag{C.35}$$

To examine the polarization of the resonant wave, it is first observed that C.20 gives approximately

$$Q = -1 + i\,(1 + C^{-2})/kz_1 n_{x2} \tag{C.36}$$

Inserting this in C.14 and remembering that $E_2 = 0$ gives

$$A = -\,ikz_1\, C^2\, n_{x2}\, B\,/\,S^2 \tag{C.37}$$

Using C.37 in Eqs. C.15 and C.16 and retaining just the dominant terms give

$$\mathcal{H}_1/\mathcal{H}_2 = -iC^2 \tag{C.38}$$

Since $|C^2|$ is on the order of unity for the resonant wave for reasonable values of the parameters, Eq. C.38 shows that the polarization close to resonance, unlike the normal situation at ELF, will contain comparable amounts of both vertical and horizontal polarization.

INITIAL DISTRIBUTION LIST

Department of Defense

Assistant Secretary of Defense
CMD, CONT, COMM & INTELL
Department of Defense
Washington, DC 20301
01CY ATTN M. Epstein
01CY ATTN J. Babcock

Director
Command Control Technical Center
Pentagon Rm BE 685
Washington, DC 20301
01CY ATTN C-650
01CY ATTN C-312

Director
Defense Advanced Research Project Agency
Architect Building
1400 Wilson Blvd.
Arlington, VA 22209
01CY ATTN Nuclear Monitoring Rsch
01CY ATTN Strategic Tech. Office

Defense Communication Engineer Center
1860 Wiehle Avenue
Reston, VA 22090
01CY ATTN Code R220 M. Horowitz
01CY ATTN Code R720 John Worthington
01CY Code R410 James W. McLean
01CY Code R103

Director
Defense Communications Agency
Washington, DC 20305
01CY ATTN Code 810 R. W. Rostron
01CY ATTN Code 480
01CY ATTN Code 101B MAJ Rood

Defense Communications Agency
WWMCCS System Engineering Org
Washington, DC 20305
01CY ATTN R. L. Crawford

Defense Documentation Center
Cameron Station
Alexandria, VA 22314
12CY ATTN TC

Director
Defense Intelligence Agency
Washington, DC 20301
01CY ATTN DIAST-5
01CY ATTN DIAAP Albert L. Wise
01CY ATTN DB-4C Edward OFarrell
01CY ATTN DT-1BZ CAPT R. W. Morton
01CY ATTN HQ-TR J. H. Stewart

Director
Defense Nuclear Agency
Washington, DC 20305
01CY ATTN DDST
01CY ATTN TISI Archives
03CY ATTN TITL Tech. Library
03CY ATTN RAAE
01CY ATTN STVL

Commander
Field Command
Defense Nuclear Agency
Kirtland AFB, NM 87115
01CY ATTN FCPR

Director
Interservice Nuclear Weapons School
Kirtland AFB, NM 87115
01CY ATTN Document Control

Director
Joint Strat TGT Planning Staff JCS
Offutt AFB
Omaha, NB 68113
01CY ATTN JPST CAPT D. G. Goetz

Chief
Livermore Division Fld Command DNA
Lawrence Livermore Laboratory
P.O. Box 808
Livermore, CA 94550
01CY ATTN FCPRL

Director
National Security Agency
FT. George G. Meade, MD 20755
01CY ATTN W65
01CY ATTN Oliver H. Bartlett W32
01CY ATTN Technical Library
01CY ATTN John Skillman R52

OJCS/J-3
The Pentagon
Washington, DC 20301
(Operations)
01CY ATTN WWMCCS Eval OFC Mr. Toma

OJCS/J-5
The Pentagon
Washington, DC 20301
(Plans & Policy)
01CY ATTN Nuclear Division

Under Secry of Defense for Research
and Engineering
Department of Defense
Washington, DC 20301
01CY ATTN S&SS (OS)

Department of the Army

Commander/Director
Atmospheric Sciences Laboratory
US Army Electronics Command
White Sands Missile Range, NM 88002
01CY ATTN DELAS-AE-M F. E. Niles

Commander
Harry Diamond Laboratories
2800 Powder Mill Rd.
Adelphi, MD 20783
01CY ATTN DELHD-NP Francis N. Wimenitz
01CY ATTN Mildred H. Weiner DRXDO-II

Commander
US Army Electronics Command
Fort Monmouth, NJ 07703
01CY ATTN DRSEL-RD
01CY ATTN J. E. Quigley

Commander
US Army Foreign Science & Tech. Center
220 7th Street, NE
Charlottesville, VA 22901
01CY ATTN R. Jones
01CY ATTN P. A. Crowley

Commander
US Army Nuclear Agency
7500 Backlick Road
Building 2073
Springfield, VA 22150
01CY ATTN MONA-WE J. Berberet

Chief
US Army Research Office
P.O. Box 12211
Triangle Park, NC 27709
01CY ATTN DRXRD-ZC

Department of the Navy

Chief of Naval Operations
Navy Department
Washington, DC 20350
01CY ATTN OP 941
01CY ATTN Code 604C3
01CY ATTN OP 943 LCDR Huff
01CY ATTN OP 981

Chief of Naval Research
Navy Department
Arlington, VA 22217
01CY ATTN Code 402
01CY ATTN Code 420
01CY ATTN Code 421
01CY ATTN Code 461
01CY ATTN Code 464

Commanding Officer
Naval Intelligence Support Center
4301 Suitland Rd. Bldg. 5
Washington, DC 20390
01CY ATTN Code 5404 J. Galet

Commander
Naval Ocean Systems Center
San Diego, CA 92152
01CY ATTN R. Eastman
03CY ATTN Code 532
01CY ATTN Code 532 William F. Moler

Director
Naval Research Laboratory
Washington, DC 20375
01CY ATTN Code 5410 John Davis
01CY ATTN Code 7701 Jack D. Brown
01CY ATTN Code 5461 Trans. Iono. Prop.
01CY ATTN Code 5465 Prop. Applications
01CY ATTN Code 5460 Electromag. Prop. Br.
02CY ATTN Code 2600 Tech. Library

Officer-in-Charge
Naval Surface Weapons Center
White Oak, Silver Spring, MD 20910
01CY ATTN Code WA501 Navy Nuc Prgms Off.
01CY ATTN Code WX21 Tech. Library

Commander
Naval Telecommunications Command
NAVTELCOM Headquarters
4401 Massachusetts Ave, NW
Washington, DC 20390
01CY ATTN Code 24C

Commanding Officer
Navy Underwater Sound Laboratory
Fort Trumbull
New London, CT 06320
01CY ATTN Peter Bannister
01CY ATTN D. A. Miller

Director
Strategic Systems Project Office
Navy Department
Washington, DC 20376
01CY ATTN NSP-2141

Department of the Air Force

Commander
ADC/DC
ENT AFB, CO 80912
01CY ATTN DC Mr. Long

Commander
ADCOM/XPD
ENT AFB, CO 80912
01CY ATTN XPQDQ
01CY ATTN XP

AF Geophysics Laboratory, AFSC
Hanscom AFB, MA 01731
01CY ATTN CRU S. Horowitz
01CY ATTN PHP Jules Aarons
01CY ATTN OPR James C. Ulwick
01CY OPR Alva T. Stair
02CY SUOL Research Library

AF Weapons Laboratory, AFSC
Kirtland AFB, NM 87117
02CY ATTN SUL
01CY ATTN SAS John M. Kam
01CY ATTN DYC CAPT L. Wittwer

AFTAC
Patrick AFB, FL 32925
01CY ATTN TN
01CY ATTN TD-3
01CY ATTN TD-5
01CY ATTN TF/MAJ Wiley

Air Force Avionics Laboratory, AFSC
Wright-Patterson AFB, OH 45433
01CY ATTN AAD

Commander
Foreign Technology Division, AFSC
Wright-Patterson AFB, OH 45433
01CY ATTN ETD B. L. Ballard

HQ USAF/RD
Washington, DC 20330
01CY ATTN RDQ
Headquarters
North American Air Defense Command
1500 East Boulder
Colorado Springs, CO 80912
01CY ATTN Chief Scientist

Commander
Rome Air Development Center, AFSC
Griffiss AFB, NY 13440
01CY ATTN EMTLD Doc. Library

Commander
Rome Air Development Center, AFSC
Hanscom AFB, MA 01731
01CY ATTN EEP John Rasmussen

SAMSO/MN
Norton AFB, CA 92409
(Minuteman)
01CY ATTN NMML LTC Kennedy

Commander in Chief
Strategic Air Command
Offutt AFB, NB 68113
01CY ATTN NRT
01CY ATTN XPFS MAJ Brian G. Stephan
01CY ATTN DOK Chief Scientist

US Energy Research and Dev. Admin.

Department of Energy
Albuquerque Operations Office
P.O. Box 5400
Albuquerque, NM 87115
01CY ATTN Doc Con for D. W. Sherwood

Department of Energy
Division of Headquarters Services
Library Branch G-043
Washington, DC 20545
01CY ATTN Doc Con for Allen Labowitz

Division of Military Application
Department of Energy
Washington, DC 20545
01CY ATTN Doc Con for Donald I. Gale

University of California
Lawrence Livermore Laboratory
P.O. Box 808
Livermore, CA 94550
01CY ATTN Glenn C. Werth L-216
01CY ATTN Tech. Info Dept L-3
01CY ATTN Frederick D. Seward L-46

Los Alamos Scientific Laboratory
P.O. Box 1663
Los Alamos, NM 87545
01CY ATTN Doc Con for T. F. Taschek
01CY ATTN Doc Con for D. R. Westervelt
01CY ATTN Doc Con for P. W. Keaton
01CY ATTN Doc Con for J. H. Coon

Sandia Laboratories
Livermore Laboratory
P.O. Box 969
Livermore, CA 94550
01CY ATTN Doc Con for B. E. Murphey
01CY ATTN Doc Con for T. B. Cook ORG 8000

Sandia Laboratories
P.O. Box 5800
Albuquerque, NM 87115
01CY ATTN Doc Con for Space Proj Div
01CY ATTN Doc Con for A. D. Thornbrough ORG 1245
01CY ATTN Doc Con for W. C. Myra
01CY ATTN Doc Con for 3141 Sandia Rpt Coll

Other Government

Department of Commerce
National Bureau of Standards
Washington, DC 20234
01CY ATTN Arthur Ernst
01CY ATTN Raymond T. Moore

Department of Commerce
Office of Telecommunications
Institute for TELCOM Science
Boulder, CO 80302
01CY ATTN William F. Utlaut
01CY ATTN L. A. Berry
01CY ATTN A. Glenn Jean
01CY ATTN D. D. Crombie
01CY ATTN J. R. Wait

Department of Transportation
Office of the Secretary
TAD-44.1, Room 10402-B
400 7th Street, SW
Washington, DC 20590
01CY ATTN R. L. Lewis
01CY ATTN R. H. Doherty

Department of Defense Contractors

Aeronomy Corporation
217 S. Neil Street
Champaign, IL 61820
01CY ATTN S. A. Bowhill

Aerospace Corporation
P.O. Box 92957
Los Angeles, CA 90009
01CY ATTN Irving M. Garfunkel

Analytical Systems Engineering Corp.
5 Old Concord Rd.
Burlington, MA 01803
01CY ATTN Radio Sciences

Boeing Company, The
P.O. Box 3707
Seattle, WA 98124
01CY ATTN Glenn A. Hall
01CY ATTN H. R. Willard
01CY ATTN J. F. Kenney

University of California
at San Diego
Marine Physical Lab of the
Scripps Institute of Oceanography
San Diego, CA 92132
01CY ATTN Henry G. Booker

Computer Sciences Corporation
P.O. Box 530
6565 Arlington Blvd
Falls Church, VA 22046
01CY ATTN D. Blumberg

University of Denver
Colorado Seminary
Denver Research Institute
P.O. Box 10127
Denver, CO 80210
01CY ATTN Donald Dubbert
01CY ATTN Herbert Rend

Develco
530 Logue Avenue
Mountain View, CA 94040
01CY ATTN L. H. Rorden

ESL, Inc.
495 Java Drive
Sunnyvale, CA 94086
01CY ATTN James Marshall

General Electric Company
Space Division
Valley Forge Space Center
Goddard Blvd King of Prussia
P.O. Box 8555
Philadelphia, PA 19101
01CY ATTN M. H. Bortner
Space Science Lab.

General Electric Company
TEMPO-Center for Advanced Students
816 State Street
P.O. Drawer QQ
Santa Barbara, CA 93102
01CY ATTN B. Gambill
02CY ATTN DASIAC
01CY ATTN Don Chandler
01CY ATTN Warren S. Knapp

Geophysical Institute
University of Alaska
Fairbanks, AK 99701
01CY ATTN T. N. Davis
01CY ATTN Neal Brown
01CY Technical Library

GTE Sylvania, Inc.
Electronics Systems GRP
Eastern Division
77 A Street
Needham, MA 02194
01CY ATTN Marshal Cross

IIT Research Institute
10 West 35th Street
Chicago, IL 60616
01CY ATTN Technical Library

University of Illinois
Department of Electrical Engineering
Urbana, IL 61803
02CY ATTN Aeronomy Laboratory

Johns Hopkins University
Applied Physics Laboratory
Johns Hopkins Road
Laurel, MD 20810
01CY ATTN Document Librarian
01CY ATTN J. Newland
01CY P. T. Komiske

Lockheed Missiles & Space Co, Inc.
3251 Hanover Street
Palo Alto, CA 94304
01CY ATTN E. E. Gaines
01CY ATTN W. L. Imhof D/52-12
01CY ATTN J. B. Reagan D/52-12
01CY ATTN R. G. Johnson D/52-12

Lowell Research Foundation, Univ. of
450 Aiken Street
Lowell, MA 01854
01CY ATTN Dr. Bibl

M.I.T. Lincoln Laboratory
P.O. Box 73
Lexington, MA 02173
01CY ATTN Dave White
01CY ATTN J. H. Pannell L-246
01CY ATTN R. Enticknapp
01CY ATTN D. M. Towle

Mission Research Coporation
735 State Street
Santa Barbara, CA 93101
01CY ATTN R. Hendrick
01CY ATTN F. Fajen
01CY ATTN M. Scheibe
01CY ATTN J. Gilbert
01CY ATTN C. L. Longmire

Mitre Corporation
P.O. Box 208
Bedford, MA 01730
01CY ATTN G. Harding

Pacific-Sierra Research Corp.
1456 Cloverfield Blvd.
Santa Monica, CA 90404
01CY ATTN E. C. Field, Jr.

Pennsylvania State University
Ionosphere Research Laboratory
318 Electrical Engineering East
University Park, PA 16802
02CY ATTN Ionospheric Rsch Lab.

R&D Associates
P.O. Box 9695
Marina Del Rey, CA 90291
01CY ATTN Forrest Gilmore
01CY ATTN William J. Karzas
01CY ATTN Phyllis Greifinger
01CY ATTN Carl Greifinger
01CY ATTN H. A. Ory
01CY ATTN Bryan Gabbard
01CY ATTN R. P. Turco

Rand Corporation
1700 Main Street
Santa Monica, CA 90406
02CY ATTN Technical Library
01CY ATTN Cullen Crain

SRI International
333 Ravenswood Avenue
Menlo Park, CA 94025
01CY ATTN E. T. Pierce
01CY ATTN Donald Neilson
01CY ATTN George Carpenter
01CY ATTN W. G. Chestnut
01CY ATTN J. R. Peterson
01CY ATTN Gary Price

Stanford University
Radio Science Laboratory
Stanford, CA 94305
01CY ATTN R. A. Helliwell
01CY ATTN R. Fraser-Smith
01CY ATTN J. Katsufrakis

TRW Defense & Space Sys. Group
One Space Park
Redondo Beach, CA 90278
01CY ATTN Saul Altschuler
01CY ATTN Dianna Dee